N° d'ordre : 41225 **Année 2013**

THÈSE

Présentée à

L'UNIVERSITE DE LILLE 1 SCIENCES & TECHNOLOGIES

pour obtenir le grade de

DOCTEUR DE L'UNIVERSITE

Spécialité : Micro et Nano Technologies, Acoustique et Télécommunications

Conception and realization of silicon solar cells based on nanostructures

par

Di Zhou

Soutenance le lundi 25 november 2013, devant la commission d'examen :

Président	**Tuami Lasri**
Rapporteurs	**Fabrice Gourbilleau**
	Georges Bremond
Examinateurs	**Ludger Wirtz**
	Etienne Quesnel
Directeur de thèse	**Didier Stiévenard**
Co-Encadrante	**Odile Robbe**

Acknowledgement

This work has been done in IEMN since 2010. I would like to express my thanks to the chief of IEMN Mr Lionel Buchaillot for allowing me to do my Ph.D in the laboratory. I also would like to thank Mr. Tuami Lasri for accepting to be the president of the jury in my defense, and Mr. Fabrice Gourbilleau and Mr. Georges Bremond for their great contribution to review this thesis. I wish to thank also Mr. Ludger Wirtz and Mr. Etienne Quesnel for participating to the jury and examining my work.

The deep and sincere appreciation to my supervisor Prof. Didier Stiévenard for continuous support of my Ph.D study and research, for his patience, kindness, expertise and excellent guidance. Without his supervision and constant help, it would not have been possible for me to finish this doctoral thesis.

I am grateful to my co-director Mrs Odile Robbe, who guide my research of zinc oxide and help me with preparation and chacaterization of the samples enthusiastically.

My sincere thanks also goes to Mr. Yan Pennec, who introduces me to theoretical work and gives me a lot of warm help and useful suggestions on the theoretical parts of my work.

I wish to thanks Mrs.Sylvia Turrell and Mr. Etienne Okada for their helping in the samples characterization.

Many thanks go to Mr. Yannick Lambert, Tao Xu and Jean-philippe Nys for their friendly help with my work in IEMN. During these three years, I have spend a lot of time in the cleaning room, so I would like to thanks all the IEMN clean room staff for their constant technical support.

I have also thank Mrs Florence Senez for help me deal with many things.

I wish to thank all my friends: Pierre, Ophelie, Ewa, Nadine, Hind, David, Raghvendra, Chong Jin, Xianglei Han, Jinshan Shi and Zhuang Xiong for their useful discussion, emotional support and entertainment.

Lastly, I would like to express my thanks to my parents for supporting me spiritually throughout my life and my dear Wei for all his encouragement and love.

Table of content

Chapter 1 Introduction

To satisfy the energy requirement, more and more fossil fuel resources, such as petroleum, coal and gas, are consumed. However, these energy sources will be used up one day and their consumption is hostile to the environment. In recent years, there has been a trend towards the increased commercialization of renewable sources. Renewable sources contains wind, hydropower, geothermal heat, biomass and solar energy. Wind power depends on the wind speed, so wind turbines should be installed in areas of higher wind resources, such as offshore and high altitude sites. Typically, turbines with rated output of 1.5-3 MW can be used for commercial use. Hydropower is derived from the kinetic energy of falling water from higher potential to lower potential. This power can be generated by large-scale hydroelectric dam. Geothermal energy is from thermal energy originating from the original formation of the planet and from radioactive decay of the minerals. This power is theoretically more than adequate to supply the energy needs, but only a very fraction may be exploited because of the high-cost of the drilling and exploration for deep resources. Biomass is a renewable energy source only if the extraction rate doesn't exceed the production rate. The energy information administration projected that by 2017, biomass will be more expensive than natural gas. About 16.7% of global final energy consumption comes from renewable resources, with 11 % of energy from biomass, and 3.3 % from hydropower and 3% from new renewable resources (wind, solar, geothermal), as shown in fig.1. However, according to a 2011 projection by the international energy agency, photovoltaic and solar-thermal plants may produce most of the world's electricity by 2060, and wind, hydropower and biomass will supply much of the remaining generation.

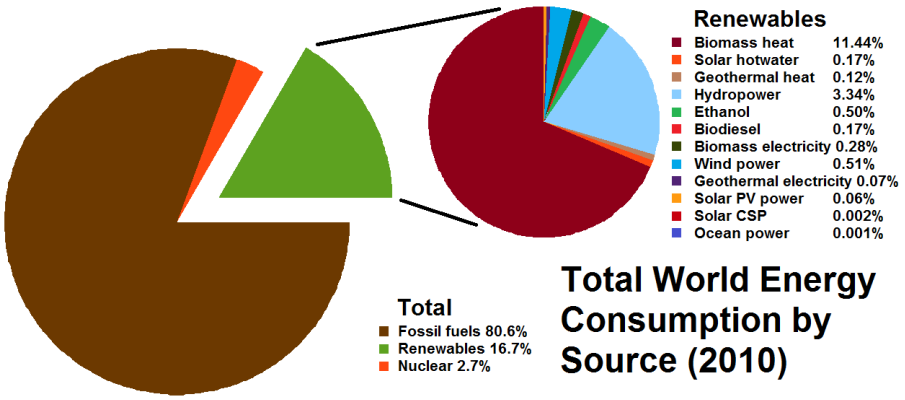

Figure 1 Total world energy consumption by source

Solar power source is radiation from the sun. The measured solar spectrum on the earth's surface depends on various factors, such as latitude and the angle of incidence, which impact the total air mass (AM) density of the atmosphere through which the sun light has passed. More specifically, $AM = \frac{1}{\cos\theta}$,where θ is the angle of incidence relative to radiation directly normal to the earth's surface. AM0, i.e. no atmosphere, represent the solar energy arriving at the top of atmosphere. To facilitate the comparison of photovoltaic technologies, two standard spectra at the earth surface have been defined, the global and direct AM1.5 spectra, i.e. AM1.5G (includes both direct and diffuse radiation) and AM1.5D (includes direct radiation only). Fig.2 gives ASTM (American Society For Testing And Materials) standard AM0, AM1.5G, AM1.5D solar spectra. [1]

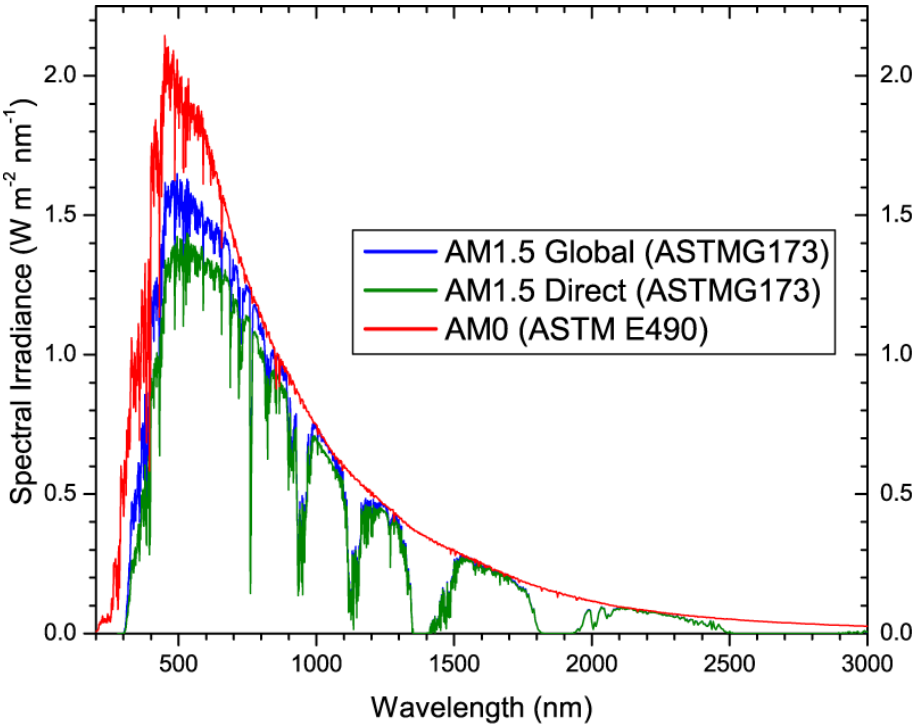

Figure 2 ASTM standard AM0, AM1.5G, AM1.5D solar spectra

1.1 Photovoltaics

1.1.1 Introduction

The science and technology of converting solar radiation energy directly into current is defined as Photovoltaics (PV). The first solar cell with a power conversion efficiency of ~6% was realized using silicon by researches from AT &T Bell Labs in 1954, 115 years

after when the concept was first defined by french physicist Edmond Becquerel[1]. Over the past years, the detailed understanding of the physics and chemistry of PV and moreover, the introduction of nanotechnology, enable the rapid developments in the field of PV.

To begin with we will provide a brief introduction on the basic behavior of solar cell. Solar cell is realized by forming a p-n junction, where the build-in electrical field separates photogenerated electron-hole pairs that diffuse to this region, so that the electrons are swept to the n-side and holes are swept to the p-side to complete a circuit.

The ideal p-n junction with no light emitting on it has a total current as follows:

$$J = J_p + J_n = \left[\frac{qD_p P_{n0}}{L_p} + \frac{qD_n n_{p0}}{L_n}\right]\left[\exp\left(\frac{qV}{kT}\right) - 1\right] = J_0\left[\exp\left(\frac{qV}{kT}\right) - 1\right]$$

where J_p and J_n are the minority carrier diffusion current densities on n and p side of the junction, respectively. D_p and D_n are the diffusion coefficients of holes (on n-side) and electrons (on p-side), respectively. L_p and L_n are minority carrier diffusion lengths. P_{n0} and n_{p0} are the thermal equilibrium density of holes and electrons in n-side and p-side, respectively. q is the charge of electron. V is the applied forward bias. T is the temperature and k is the Boltzman constant.

However, some electron-hole pairs get lost before collection due to the recombination, so the equation becomes:

$J = J_0\left[\exp\left(\frac{qV}{\eta kT}\right) - 1\right]$ where η is the ideality factor

When light is applied to the p-n junction, a current J_L will be generated, so the general expression for a semiconductor p-n diode solar cell is:

$$J = J_0\left[\exp\left(\frac{qV}{\eta kT}\right) - 1\right] - J_L$$

The J-V curve, as shown in Fig.3, contains critical informations relating to the efficiency of the solar cell.

- short-circuit current density J_{sc}, which is equal to the light generated current density, provides the maximum current density at zero voltage;

-open-circuit voltage V_{oc}, provides the maximum voltage at zero current.

$$V_{oc}=\eta\frac{kT}{q}\ln\left(\frac{I}{I_0}+1\right)\approx\eta\frac{kT}{q}\ln\left(\frac{I_L}{I_0}\right)$$

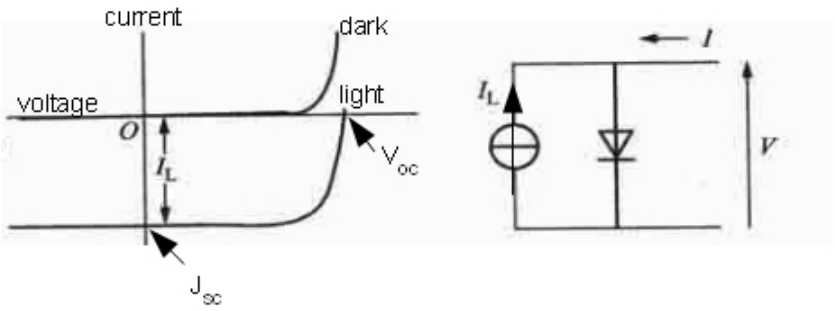

(a) (b)

Figure 3 (a) Typical representation of an I-V curve, showing short-circuit current (J_{sc},) and open-circuit voltage points (V_{oc}) (b) equivalent circuit

- fill factor (FF), can be defined as the ratio of maximum power of the solar cell $P_{max}=I_m V_m$, to the power $P=I_{sc}V_{oc}$. This parameter shows the quality of pn junction and can be calculated by the empirical equation for the ideal diode:

$$FF=\frac{I_m V_m}{I_{sc}V_{oc}}=\frac{V_{OC}-\ln(V_{OC}+0.72)}{V_{OC}+1}$$

- conversion efficiency η

$$\eta=\frac{I_m V_m}{P_0}=\frac{J_{sc}V_{oc}FF}{P_0}$$

in which P_0 is the applied power density to the device.

Additionally, quantum efficiency of the device as a function of wavelength is another important feature, which includes external quantum efficiency (EQE) and internal quantum efficiency (IQE). EQE is based on the I_L measured for the solar cell as a function of wavelength:

$$EQE=\frac{I_L}{qn_{ph}}=\frac{I_{SC}}{qn_{ph}}\qquad IQE=\frac{EQE}{A}=\frac{EQE}{1-R-T}$$

n_{ph} is the incident photons flux as a function of wavelength, per unit time, A is the absorbed light, R is the reflected light and T is the transmitted light.

Spectral response (SR) is typically used to characterize the performance of solar cell.

$SR = \frac{I_{SC}}{P_{¿}(\lambda)} = q\frac{\lambda}{hc}EQE$, $P_{in}(\lambda)$ is the power of incident light.

The quantum efficiency can provide valuable insight into the loss mechanisms of the solar cell, including front surface recombination and back recombination.[1-3]

1.1.2 Solar cell technologies

Si solar cells have been realized with an efficiency of approximately 27.6%, close to the theoretical limit for Si single junction, nevertheless, with high cost for mass production. For commercial application, increasing efficiency while decreasing cost have to be taken into consideration. Fig.4 depicted the efficiency of different solar cells as a function of time. If we compare the efficiency of single junction solar cells, we can see the efficiency relations as follows: GaAs solar cells >Si crystalline solar cells>Cu(In,Ga)Se_2 and other thin films solar cells >organic solar cells, quantum dot cells and other emerging cells. Although the efficiencies of organic cells are lower, they attract more and more attention, because of their low-cost and flexibility. It can be seen that multijunction cells achieve higher efficiencies than the best single junction cells, especially with concentrator. The maximum efficiency is 44%. So far, solar cell technologies have been classified into three generations. The first generation is based on crystalline Si bulk, with high efficiency but high cost. In order to decrease the cost, the second generation based on low-cost thin films have been developed. However, their efficiencies are lower than that of crystalline Si cells. Due to its lower efficiency, nanostructures are introduced to the second generation solar cells, as is called the third generation. The details will be discussed below.

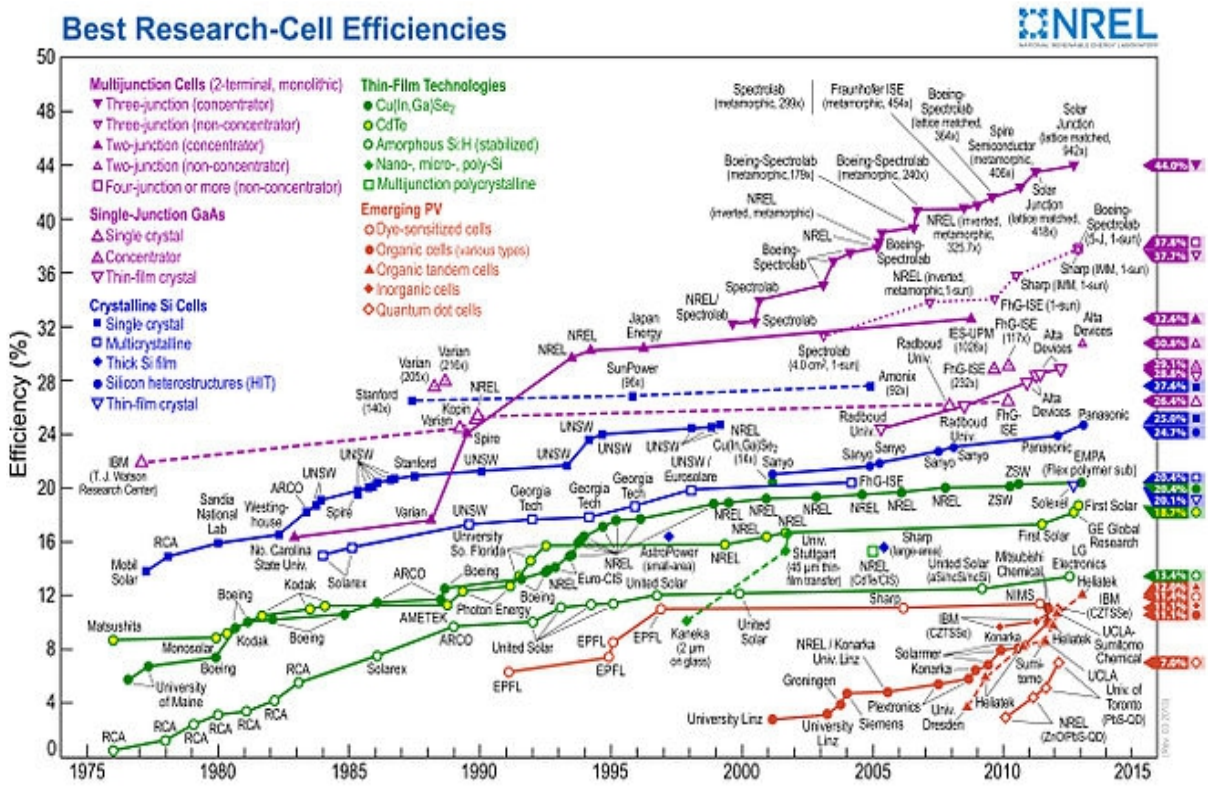

Figure 4 Reported timeline of solar cell efficiency (from National Renewable Energy Laboratory (USA))

First generation devices

The first-generation devices are mainly fabricated from bulk silicon. As we mentioned before, the best commercial solar cells based on single-crystal silicon are about 18% efficient, less than the theoretical efficiency because of the Shockley-Queisser limit, which places maximum solar conversion efficiency around 30% for a single p-n junction with a bandgap of 1.1 eV (typical for silicon) with consideration of the effect of blackbody radiation, recombination and spectrum loss. It was first calculated by William Shockley and Hans Queisser in 1961[4].

In pursuit of this high efficiency, the cost was sacrificed to produce thick and high-purity single crystalline Si.

To lower the price, polysilicon or multicrystalline silicon are suitable alternatives, in spite of their lower efficiencies owing to the presence of a high density of defects and grain boundaries. However, the efficiency can be improved by various methods such as purification (by purifying atmosphere, mold and coating materials) and enlargement of grain size.[5] The highest efficiency for multicrystalline silicon solar cell reported so far is

20.3% on small device area (1 cm^2), with a passivated rear surface in combination with a textured front surface. [6]

Second generation devices

The second-generation devices are fabricated on low-cost substrates, such as polymers, metal foils and glass. Thin films consisting of Crystalline silicon, amorphous silicon, CIG ($Cu(In,Ga)Se_2$), organic, dye-sensitized and CdTe, are deposited directly on these substrates rather than bulk, so will reduce the price by a factor of 2 to 5 times. However, these thin-film solar cells yield efficiencies less than ~12%.

1 crystalline Si thin films solar cell

Si thin films solar cells contain monocrystalline Si, polycrystalline Si, multicrystalline Si and nanocrystalline Si solar cell. Crystalline Si thin film solar cells with efficiency comparable to bulk Si solar cell have merely been achieved with polycrystalline silicon and monocrystalline Si on high-temperature-resistant substrates. CSG solar cell (crystalline silicon on glass) combining the advantages of standard silicon wafer-based technology with the advantages of thin films, has an efficiency of 8–9%.[7]

Owing to the low absorption coefficient of crystalline Si, typically, solar cell should be thick enough to absorb more light. For thin film solar cell, this problem has been addressed by light trapping schemes, for instance, texturing either substrate or surface to increase the path length of light through solar cell and depositing an anti reflection coating on the top of solar cell to reduce the reflection. The use of highly textured transparent conducting oxides such as Al-doped ZnO have been shown to increase J_{sc} by increasing the absorption and EQE in the near-IR portion of the solar spectrum[8].

Besides, the recombination at grain boundaries and crystal defects in the grains further lower the efficiency, which can be addressed by surface passivation. The passivation scheme relies on the doping type and resistivity of Si. Typically, Si_3N_4, SiO_2, Al_2O_3 and amorphous Si are used as effective passivation schemes in crystalline Si solar cells[9]. Additionally, rapid thermal annealing or plasma hydrogenation are widely used to passivate polycrystalline silicon[10].

Due to the high density of grain boundaries and low minority carrier lifetime, intrinsic layer is used in nanocrystalline Si solar cell to increase the solar cell efficiency. The p-i-n

junction with amorphous Si passivation layer shows an efficiency of 8.6%, up to 10.9% by adding a texture back reflector.[11]

2 amorphous Si(a-Si:H) thin-film solar cells

Hydrogenated amorphous Si(a-Si:H) thin-film solar cells have been widely spread, with the efficiency below 8%, because a-Si:H is based on low temperature process and it can absorb light very efficiently with an absorption depth of 1 μm, several hundred times thinner than that of the crystalline silicon. However, its carrier mobilities (μ) and lifetimes (τ) are significantly reduced compared to crystalline Si, with mobilities of approximately 1 to 20 cm^2/V-s (50-1300cm^2/V-s for typical c-Si) and τ less than 1 μs (1 μs to 1ms for typical c-Si). [12]

3 CIG(Cu(In,Ga)Se_2) solar cells

Chalcopyrite semiconductors such as $CuInSe_2$ (CIS) and $CuIn_{1-x}Ga_xSe_2$ (CIGS) are of particular interest for solar-cells applications, because its conversion efficiency exceeds 19.9% in active areas. CIGS thin films are primarily deposited by many methods at high temperatures, such as co-evaporation, sputtering and electrodeposition. The high temperature makes it difficult to deposit thin films on some low melting point substrates. And because of the toxic of selenization, vacuum and selenization treatment are required, which lead to high cost.[13] Many efforts have been done to avoid high temperature process in vacuum and selenization treatment, so that it is possible to deposit thin film on flexible substrates in low-cost way.

4 Organic and dye-sensitized solar cell

Organic solar cells have become an alternative to silicon solar cell because of their inexpensive solution-based processing and significant flexibility. Organic solar cell uses a polymer or dye as an electron donor and a second material as the electron acceptor.

Unlike traditional semiconductor solar cells where the photogenerated electron-hole pairs were separated by build-in electrical field of p-n junction, photogenerated electron-hole pairs in organic solar cell are known as a Frenkel exciton. In one component device, the excitons are dissociated by charge transfer in organic-metal interface, while in two component devices, the excitons will be separated if the differences in potential energy between two materials are larger than the exciton binding energy. [14]

Although organic solar cells cost less, the efficiency is relatively lower, due to the poor light absorption; most of the organic semiconductor have a relatively large bandgap (above

2 eV), so the light absorption are efficient for blue light but poor for red light. In addition, the exciton energy of these materials is in the range of 0.1 eV to 1 eV, which is too large to be easily separated, so the photocurrent generation is limited. Besides, holes mobility in polymer are very poor.

Dye-sensitized solar cell (DSSC) is an important branch of organic solar cell. It consists of three-components: a dye or inorganic sensitizer are adsorbed onto the surface of mesoporous n-type materials such as TiO_2 and the rest of the pores are filled with p-type hole-transporting materials (HTMs), including I_3^-/I^- electrolyte solution and polymer electrolyte[14-16]. The first DSSC was demonstrated by Grätzel and coworkers.[18] This solar cell separates the charge generation which is done at the semiconductor-dye interface, and the charge transport which is done by the semiconductor and the electrolyte. Equally important, the porous material can adsorb more dye, which in turn enhances the light absorption. So the efficiency is relatively higher compared with normal organic solar cell. Schematic representation of a DSSC is shown in Fig 5. Its working principle is: (1) the incident photon is absorbed by the dye molecule and an electron of dye is excited; (2) the excited electron is injected into the conduction band of TiO_2 particles, leaving the dye molecule to an oxidized states; (3) after passing through the porous particles to the TCO layer on the glass substrate (negative electrode) and then going through an external load to the positive electrode, the injected electron is finally transferred to the triiodide (I_3^-) in electrolyte and iodide (I^-) is obtained; (4) iodide(I^-) reduce the oxidized dye to complete the circuit.[17-18]

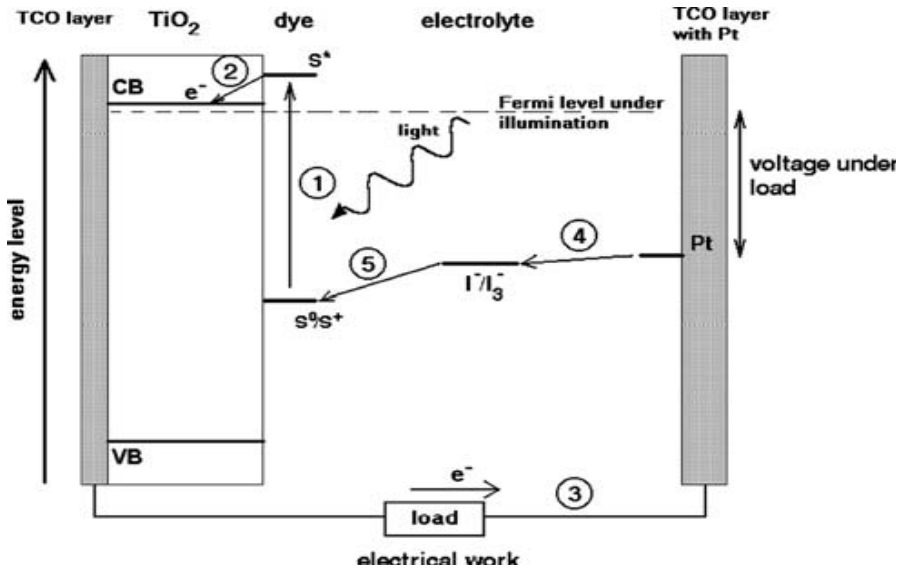

Figure 5 Working principle of DSSC

These cells are still in their early infancy, compared with inorganic thin-film cells. The commercialization of DSSC is slowly under way, due to the difficulties of packaging solar cells, poor heat resistance and ageing issues. The first problem can be solved by introducing solid-state electrolytes such as 2,2',7,7'-tetrakis-(n,N-di-p-methoxyphenyl-amine)-9,9'-spirobifluorene (or spiro-MeOTAD), PCPDTBT (poly(2,6-(4,4-bis-(2-ethylhexyl)-4H-cyclopenta[2,1-b;3,4-b']dithiophene)-alt-4,7(2,1,3-benzothiadiazole)) into DSSCs, and yet these solid-state devices achieve efficiencies on the order of 4%, which is quite low. In spite of the low efficiency and many issues, organic solar cells are still very suitable substitutes in solar cell application due to the attractive low production costs and their flexibility.

5 Cadmium telluride (CdTe) solar cell

Cadmium telluride (CdTe) with a bandgap of 1.45 eV, close to the optimal bandgap for photovoltaic energy conversion, has long been recognized as a strong candidate for thin film solar cell applications. CdTe solar cells are typically heterojunctions with cadmium sulfide (CdS) fabricated by a variety of low-cost deposition technologies, such as close spaced sublimation (CSS) and sputtering. Small area efficiencies of these solar cells have approached the value of 16.0% and in order to commercialize this technology, considerable efforts are made to decrease the price, increase the efficiency and protect environment from pollution associated with Cd in the manufacturing process and at the end of cell life, which is the key technological challenges for CdTe solar cell.[19]

Third generation devices

Second generation devices significantly decrease the price of solar cell, but decrease the efficiency. Third-generation device is based on second generation devices, adding nanostructures, which provide significant larger area surface to increase the light harvesting. So the new generation devices will achieve higher efficiency by combining the advantage of the second generation devices with the advantage of nanostructures.

The mechanisms that attempt to increase the efficiency of single-bandgap solar cells are: (1) broader the absorption and conversion spectra of the solar cell, primarily in the low-energy regions where the photons are not absorbed by a single-bandgap semiconductor; (2) improving the photogeneration rate by using high-energy photons in the solar spectrum better, typically, those photons are thermalized by interaction with

lattice phonon or are absorbed in the surface of solar cell; (3) creating more than one electron or photon per each absorbed photon to improve the photocurrent. [1]

The third-generation solar cells contain tandem solar cells, intermediate band solar cells, hot electron solar cells, multiple-exciton generation based solar cells, upconversion and downconversion based solar cells.

1 Tandem solar cell

The tandem cell, consisting of two or three semiconductor *p*-*n* junctions of different bandgaps, have a broad light absorption spectrum and yield higher efficiency compared to single-bandgap devices. To achieve the highest efficiency, the key parameters during fabrication are appropriate bandgaps, thicknesses, junction depths, and doping, which should be optimized, so that the incident solar spectrum is split between the cells most effectively.

There are two configurations, 'mechanically stacked' cell, in which each cell in the stack is treated as a separate device with two terminals; another configuration is an 'in-series' cell with each cell in the stack connected in series, such that the overall cell has just two terminals on the front and back of the whole cell. Although these two configurations have the same efficiency, the mechanically stacked solar cell is more flexible in practical, because each cell can be made individually, and then be connected with each other in the external circuit.

The higher efficiency tandem devices with over 40% efficiency are made from single-crystal III-V materials, experimental multijunction cell, using metamorphic materials, four or more junctions, and other design approaches have the potential to increase cell efficiencies over 45%, or even to 50%[20]. Those high quality material are grown by very expensive epitaxial processes, so they are merely used in the space market where cost is less of a technology concern than supplying sufficient power [21].

To reduce the price, non-toxic or abundant elements or compounds such as a-Si or Si nanostructure are used as substitutes in tandem devices. Because of the high defect density located in a-Si and at the surface of Si nanostructures, the solar cell efficiencies are lower compared with epitaxial III-V materials solar cell. One popular way to improve the efficiency is to introducing a thin intermediate reflector (IR) which enhances the *J*sc of the top cell without increasing the thickness of absorber layer, as showed in Fig 6. This kind of solar cell yield the efficiency over 12%, with J_{sc} up to almost 12 mA/cm^2.[22]

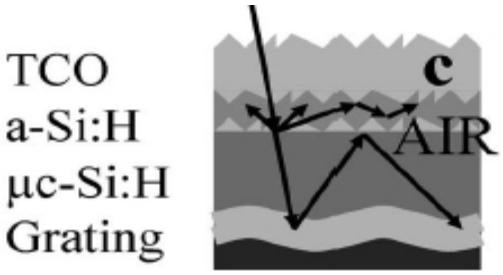

Figure 6 Design of n-i-p micromorph with IR

Additionally, the tandem solar cell can be made based on different second generation solar cell. J.Kim *et al.*[23] demonstrated tandem solar cell efficiencies of more than 6%, with the low band-gap polymer-fullerene composite as the charge-separating layer in the front cell and the high band-gap polymer composite as that in the back cell. S.Wenger *et al*.[24] reported on the integration of dye-sensitized solar cell and $Cu(In,Ga)Se_2$ solar cell to cut optical losses and material costs, achieving 12.2% conversion efficiency. The corrosion issue originating from redox mediator (I^- / I_3^- couple) of the dye-sensitized cell can not be neglected.

Besides, nanostructures such as quantum wells (QWs) or quantum dots (QDs), are introduced in tandem solar cells. An effectively larger bandgap is formed if QWs or QDs are closely spaced between layers of dielectric matrix. For QDs of 2 nm (QWs of 1 nm), an effective bandgap is 1.7 eV which is quite ideal for a tandem cell element on top of Si cell[21].

2 Intermediate-band (IB) solar cell

The intermediate-band (IB) solar cell consists of an IB material between n- and p-type semiconductors, as shown in fig.7(a). IB solar cells can deliver a high photovoltage by absorbing two sub-bandgap photons to produce one high energy electron[25]. As mentioned before, close spacing QDs will form an effective bandgap, so they can be used as an IB material. Fig.7(b) shows the quantum efficiency of GaAs/GaAs single-junction solar cells with and without an array of InGaAs self-organized Qds. The introduction of a narrow-gap material (QD array) increases the photocurrent in sub-bandgap region[26].

Dilute semiconductor alloys including InGaAsN and ZnTe:O can also be used as IB materials[27], where IB position is tunable by varying alloy composition. Compared with reference cell, the bulk solar cells with IB material ZnTe:O have a larger short circuit

current density J_{SC} and smaller open circuit voltage V_{OC}, with an overall improvement of 50% in the power conversion efficiency.

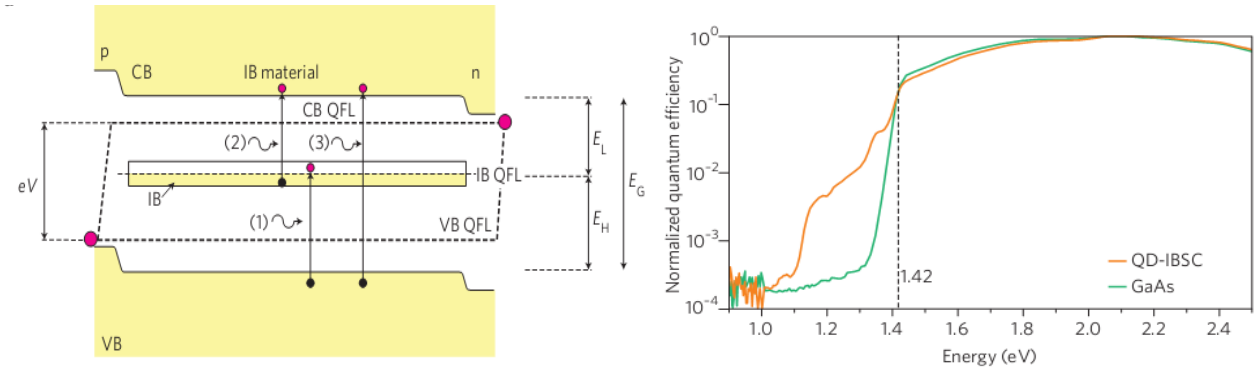

(a) (b)

Figure 7 (a) Band diagram of an IB solar cell (1) and (2) represent sub-bandgap photon absorption; (3) represents above-bandgap photon absorption. (b) Quantum efficiency of an QD-based IB solar cell (QD-IBSC) and a reference (GaAs) solar cell.

3 Multiple-exciton generation based solar cells

Multiple-exciton generation based solar cells will increase the efficiency by increasing the number of electron-hole pair per given photon to increase the photocurrent density. Carrier multiplication in semiconductor nanocrystals are enhanced by impact ionization process, as shown in Fig.8(a), where a high energy exciton was created in a nanocrystal by absorbing a photon of energy >2*Eg*, and then it relaxes to the band edge, along with the energy emission of at least 1*Eg,* which transfers to a valence band electron and excites it above the energy gap. Thus, this process converts more light with high photon energy into current.[28]

R. D. Schaller *et al.*[28] demonstrate for the first time that impact ionization in PbSe NCs take place on an ultrafast time scale with high efficiency, so these NCs have potential to significantly increase solar cell power conversion efficiency.

However, J.J.H.Pijpers *et al.*[29]demonstrated carrier multiplication is more efficient in bulk materials than in quantum dots, due to the reduced density of states in quantum dots. Carrier multiplication in quantum dots may be beneficial because extra carriers can be exploited at higher voltages ($E_{gap,QD}$ is always larger than $E_{gap,bulk}$), but the quantum confinement doesn't lead to higher carrier multiplication efficiencies.

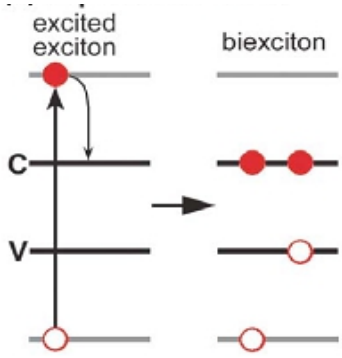

Figure 8 Schematics of impact ionization process

4 Upconversion and downconversion

In order to increase the absorption of solar energy, there are two ways to adapt the solar spectrum before it is absorbed by the solar cell. The first option is to transfer two lower-energy photons to one higher-energy photon which can be absorbed by solar cell. This process is known as upconversion (UC) and is particularly useful for solar cells with a large band-gap. The second option is to split one higher energy photon to two photons with a smaller energy which can be absorbed by the solar cell. This is known as downconversion (DC) and is especially beneficial for solar cells with a smaller band-gap. [1,19.31]

Lanthanide ions are very suitable to use for both DC and UC, thank to a rich energy level structure. There are many examples of efficient upconversion and downconversion using lanthanides, either with one type of lanthanide ion or a pair of lanthanide ions.

J.F.Suvyer demonstrated that upconversion lattices $NaYF_4$ codoped with Er^{3+},Yb^{3+}/Er^{3+} or Yb^{3+}/Tm^{3+} lead to as much as 50% of the excitation photons contributing to the upconversion emission[30].

Downconversion is focused on the conversion of a single UV photon into two visible photons. J.Meijer *et al.* studied the efficiency of downconversion for the (Nd^{3+},Yb^{3+}) couple in YF_3, downconversion is observed from the $^4D_{3/2}$ level of Nd^{3+} with efficiencies up to 40%[31].

5 Hot-carrier solar cell

A hot-carrier solar cell tends to slow the rate of photoexcited carrier cooling, which is caused by phonon interaction in the lattice, to allow time for carriers to be collected while they are still at elevated energies (‘hot’). This allows higher voltages to be achieved by the

cell. In addition to an absorber material that slows the rate of carrier relaxation, a hot carrier cell must allow extraction of carriers from the device through contacts that accept only a very narrow range of energies (selective energy contacts)[21].

Initial experimental progress has been made on selective energy contacts using double-barrier resonant tunneling structures, with a single layer of Si quantum dots providing the resonant level. The problem of slowing carrier cooling is very difficult. It has been observed at very high illumination intensities via a phonon bottleneck effect in which carrier energy decay mechanisms are restricted. Compounds with large mass difference between their anions and cations have a gap in their allowed phonon modes that can slow down these decay mechanisms and enhance the bottleneck effect. Examples are GaN and InN, with some experimental evidence for slowed cooling in the latter. Theoretical work on replicating this effect by modifying the phonic band structures of QD nanostructure superlattices will soon be attempted experimentally. Nevertheless, the hot carrier cell, while promising, is still a long way from demonstration.

In addition, semiconductor NCs can also be used for down shifting. The most used NCs are CdSe NCs, which lead to a strong enhancement of photocurrent in the high-energy portion of solar spectrum.[32]

1.2 Nanowires

1.2.1 Introduction

The above discussion on the third generation solar cells highlights the strong potential role of nanostructures on contributing to achieve low-cost, high-efficiency solar cells. The nanostructures are classified by dimensionality, i.e. nanostructured bulk materials and composites (3D), quantum wells (2D), nanowires and nanotubes (1D), and nanoparticles and quantum dots (0D).

Among the nanowires, silicon nanowires (SiNWs) are introduced in this work, because Si is widely considered as an important material for solar cell, although the indirect bandgap of Si is not the ideal for solar cell. In addition, its optical thickness is ~125 μm, whereas the optical thickness of direct bandgap material such as GaAs is ~0,9 μm. The key reason why Si is favored for PV industry today is that it is the second most abundant element in the earth, inexpensive and non-toxic compared to the other materials.

Particularly, the tremendous Si technologies have been developed in the last few decades. In this thesis, we will concentrate on SiNWs.[33]

1.2.2 Fabrication of silicon nanowires

To begin with, we should briefly introduce the fabrication of SiNWs, which is essential to the properties of silicon nanowires.

In principle, there are two basic approaches for preparing nanowires, i.e. the bottom-up and top-down approaches. The bottom-up approach is an assembly process which joins Si atoms to form nanowires, including vapor-liquid-solid (VLS) growth[34], oxide-assisted growth (OAG), supercritical-fluid-based and solution-based growth, and related methods.

The preparation of SiNWs via the gold-catalyzed VLS growth process involves: (1) depositing gold on a heated Si wafer to form gold droplets or evaporating gold layer on a Si wafer passivated by H[35]; (2) Si precipitation to form SiNWs from the droplet. Gold is the most popular metallic catalyst used in VLS growth process, but the presence of gold frequently induces deep-level electronic states in the Si bandgap and decreases the carrier lifetime and diffusion length, which is not beneficial for solar cells. Therefore, other metals, such as copper (Cu), platinum (Pt) and aluminum (Al), which are less detrimental to the carrier lifetime, are preferred.

The top-down approach prepares SiNWs via dimensional reduction of bulk Si by lithography and etching[36]. Electron beam lithography, reaction ion etching (RIE), natural lithography (chemically synthesized nanospheres as masks for patterning different shapes of particles and pillars), and the newly developed metal-catalyzed electroless etching (MCEE) are widely used to fabricate nanowires with dimensions ranging from tens to hundreds of nanometers. Weisse *et al.* fabricated silicon nanowires by the well-established Ag-assisted electroless wet etching technique, where they pattern Ag films by using silica spheres via Langmuir-Blodgett assembly[37-38]. In this process, nanowires keep the uniform electrical characteristics from the mother wafers, whereas the electrical properties of nanowires produced by the bottom-up approach depends on the dopant distribution during the fabrication process[39]. Fig.9 shows the boron distribution of nanowires made by top-down method and bottom-up method. The axial and radial B distribution in nanowires made by top-down are spatially homogeneous, while B distributes inhomogeneous in VSL-nanowires. The properties of nanowires will be discussed in the next section.

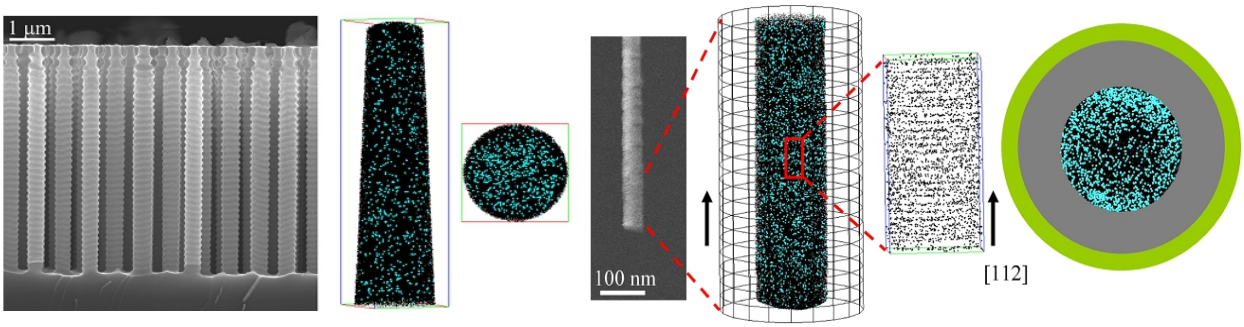

(a) (b)

Figure 9 Boron distribution of nanowires measured by laser-assist atom probe tomography.
(a) Nanowires are made by top-down method.(b) Nanowires are made by bottom-up method

1.2.3 Properties of silicon nanowires

In pursuit of solar cell with high efficiency, two important considerations have to be taken into account: high absorption and high carrier collection probability. SiNWs receive more attention as efficient light absorber for photovoltaic application owing to its high broadband optical absorption. As shown in fig.10, compared to thin films, the nanowire structures have the advantage of small reflection in a wide spectrum range even without antireflection coating[40]. The absorption of nanowires varies with the changing of array dimensions, including diameter, the period and the length. With the increase of diameter, the onset energy for absorption will be tuned from ultra-violet radiations to the visible light spectrum, as confirmed by experimental photocurrent measurement.[41] Using longer wires will improve the absorption in the low-frequency region where the absorption is limited by the small extinction coefficient of Si.[42] It was calculated that nanowires with a tapered tip will enhance the anti reflection properties.

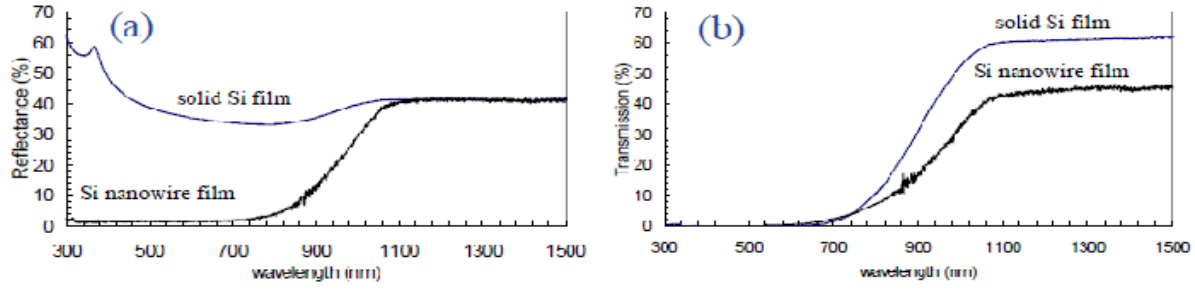

Figure 10 (a) Total reflectance and (b) transmission spectra of silicon nanowire and solid Si film

In order to obtain high efficiency, apart from high absorption, high carrier-collection probability is also important. Carrier-collection probability depends on the minority carrier diffusion length. As we mentioned before, SiNWs prepared by two methods have different electrical transport properties. Top-down nanowires keep the transport properties from the mother wafers, so the high carrier-collection can be obtained by choosing suitable mother wafer and making properly surface passivation. Whereas the transport properties of bottom-up nanowires depends on the growth process. Doped Au-catalyzed VLS-grown SiNWs has a lower mobility of 16 cm^2Vs^{-1}[43] and low minority carrier diffusion length (up to 4 μm) as a result of Au incorporation into the wires. So carrier-collection probability can be improved by replacing Au with non-Au catalysts. Using Cu VLS catalyst, SiNWs have relatively higher minority carrier diffusion length of ~10 μm, while their diffusion length are all considerably smaller than the diffusion length in high-purity bulk Si.[44]

1.2.4 Photovoltaic devices based on silicon nanowires

Because of the excellent optical properties and transport properties, SiNWs are regarded as the most attractive candidate for photovoltaic application. Many solar cells have been fabricated, such as: single SiNW solar cell, SiNWs based heterojunction solar cells and homojunction solar cells.

Single SiNW solar cell

As shown in fig.11, single SiNW solar cell with Schottky metal/semiconductor junction, has an overall efficiency of 0,46%.[45] Another single SiNW solar cell based on p/i/n coaxial junction shows the overall efficiency of ~3%.[46] These researches will provide an insight into nanowires charge transport and collection properties, which will contribute to optimize the efficiency of the NW arrays solar cells.

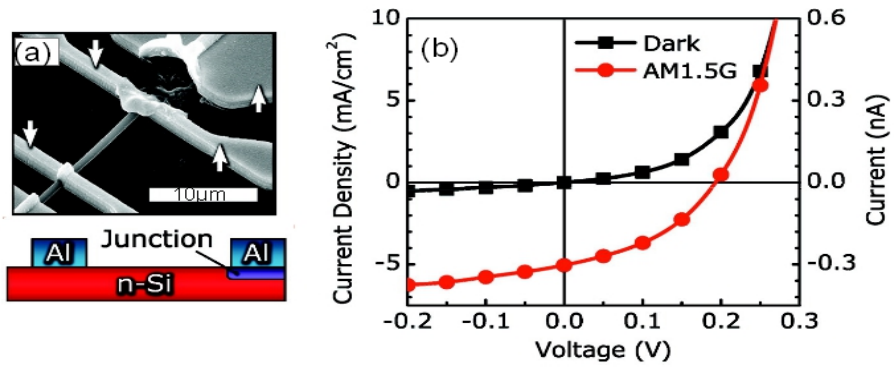

Figure 11 (a) SEM image of a single SiNW solar cell, the rectifying junction was formed by sourcing current between the adjacent upper contacts (upward-facing arrows) until the enclosed wire segment was destroyed. The *IV* data were then measured between the two inner contacts (downward-facing arrows).(b) J-V curve and I-V curve of this solar cell in the dark and under AM 1.5G illumination

SiNWs arrays based heterojunction solar cells

Recently, SiNWs/organic-semiconductor hybrid solar cell has attracted a lot of attention, because it exploits the advantage of SiNW for higher light absorption and organic semiconductor for low-cost. This hybrid solar cell fabrication process requires lower temperature (less than 200°C), so it's inexpensive compared to conventional Si p-n junction. Typical organic materials for the hybrid device are conjugated polymers, including poly (p-phenylenevinylene) (PPV) and its derivatives (CN-PPV, MEH-PPV,MEH-CN-PPV), MDMO-PPV, polythiophene (PT) and its derivatives (P3HT and PTEBS), and the polyanilines (PAn). They are mainly p-type semiconductors. N-type polymers are also available, but less effort has been made to synthesize and characterize them.[1]

Hybrid solar cell on the glass substrate were made using n-type SiNW arrays and poly(3-hexylthiophene):-phenyl-C61-butyric acid methyl ester (P3HT:PCBM). Fig.12 shows the transfer process: chemical etched n-type SiNWs were pressed into the polymer film, and then the donor wafer was removed by a lateral force. Metal contact was subsequently deposited on the exposed SiNWs tips to complete a solar cell. Compared to organic solar cell without SiNWs (with efficiency of 1.21%), hybrid solar cell shows higher efficiency of 1.91%.[47]

Owing to the large chains which prevent polymer from penetrating the small gaps in the SiNWs, the efficiency of the solar cell is limited. Short chain polymers, such as 2,2',7,7'-Tetrakis-(N,N-di-4-methoxyphenylamino)-9,9'-spirobifluorene (Spiro-OMeTAD) can easily

penetrate into the small gaps between NWs. This device has a power conversion efficiency of 10,3%.[48]

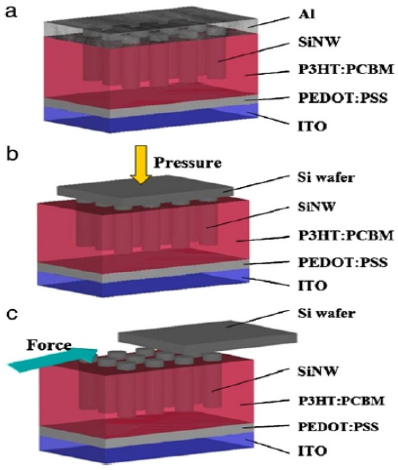

Figure 12 Schematic of the hybrid solar cell using SiNWs and P3HT:PCBM blend: (a) depositing polymer blend on ITO; (b) pressing SiNWs into the blend; and (c) silicon wafer was seperated from the polymer blend.

In addition to polymer semiconductor, carbon nanotubes (CNT) and graphene are appropriate electrode materials in solar cells. Hybrid solar cells composed of a CNT/SiNWs heterojunction cell and a SiNW array-based photoelectrochemical (PEC) cell show a conversion efficiency of 1.29%. Conductive CNT film formed heterojunctions with SiNWs and also acted as the transparent counter electrode in PEC cell, as shown in fig.13.[49]

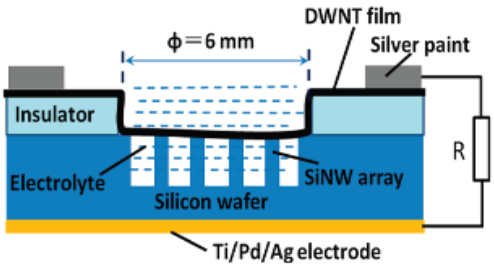

Figure 13 Hybrid heterojunction/PEC solar cell structure

Graphene, with ultrahigh mobility, outstanding flexibility, stability and high transmittance within the visible - infrared region, has attracted tremendous attention in photoelectronic devices. Theoretical studies have been performed to simulate the conversion efficiency of graphene/semiconductor heterojunction solar cell. It was shown that a maximum efficiency of ~9.2% can be achieved by tuning graphene work function, changing layer numbers and

adding an anti reflection film (SiNWs arrays). Subsequently, the experimental studies show that graphene/SiNWs solar cell give an efficiency of up to 7.7%.[50]

SiNWs arrays homojunction solar cell

Axial p-n junction

Axial p-n junction SiNW arrays solar cells possess greater light absorption and essentially work similarly to conventional planar p-n junction cells, but their p-n junction areas are smaller.[31] Sivakov e*t al.* [51] have reported the fabrication of axial p-n junction SiNWs arrays solar cell using an electroless wet chemical etching process of a microcrystalline (mc)-p^+-n-n^+ Si layer on glass, as shown in fig.14. This solar cell have an overall power efficiency of 4.4% under AM1.5G illumination.

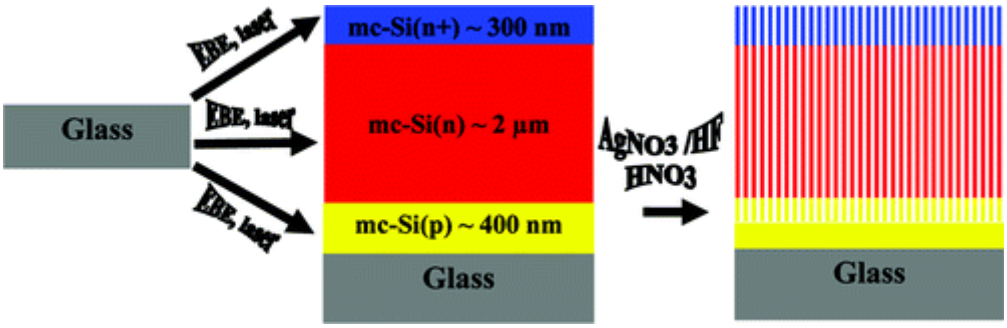

Figure 14 Schematics of the axial p-n juntion SiNW arrays solar cell fabrication process, the mc-Si p-n junction layers were deposited by electron beam evaporation (EBE) on a glass substrate (middle) and the SiNWs were obtained by wet chemical etching (right).

Weisse *et al.* reported a new method to fabricate axial junction SiNWs electronic devices on arbitrary substrates by vertical transfer printing methods(V-TPM), as shown in fig.15. Axial SiNWs arrays were formed by chemical etching of p-n junction wafer, and the crack which was introduced by inserting a wafer soaking step between two consecutive etching steps, enables the device to be transferred. This method facilitates the fabrication of large area SiNWs arrays on arbitrary substrates, including plastic sheets, metal foils and glass slides.[37] Solar cells on inexpensive substrates have big potential, although their efficiency is still under improvement.

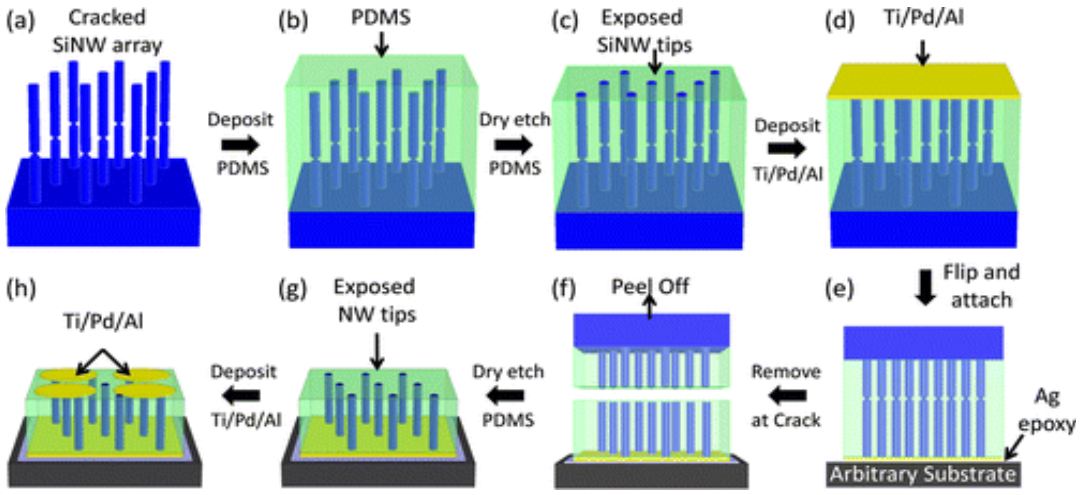

Figure 15. Schematic of SiNW arrays electronic device fabrication process with V-TPM: (a) forming horizontally crack (b) covering SiNWs with PDMS. (c) etching PDMS to expose SiNW tips. (d) depositing metal contact on the exposed SiNW. (e) attaching the metal contact to an arbitrary substrate. (f) peeling off SiNW arrays from wafer. (g) exposing the other side of SiNW tips. (h) depositing another metal contact to complete the device.

Radial p-n junction

In conventional planar p-n junction solar cell, as shown in fig.16(a), an incident photon creates an electron-hole pair which is separated by a built-in electric field. To generate power, the carriers (electrons and holes) must be able to traverse the thickness of the cells. i.e. they must have the carrier diffusion length $Ln > 1/\alpha$, where $1/\alpha$ is the optical thickness of the material (optical thickness is the thickness of material required to absorb 90% of the incident photons with energy above the band-gap energy). And in order to have more absorption, the cell thickness should be bigger than $1/\alpha$, which will decrease the device efficiency because of the carrier recombination.[52] So for a conventional planar solar cell, there are two key constraints: (1) the material must be sufficiently thick in order to absorb more photons; (2) the material must have a high minority carrier diffusion length to effectively collect the photogenerated charge carriers.[52]

A semiconductor device consisting of arrays of radial p-n junction nanowires will provide a solution to this contradictory. Fig.16 (b) depicts the radial p-n junction nanowires solar cell and its corresponding energy band diagram. The exterior shell of the nanowire was assumed to be n-type and the interior core was assumed to be p-type. A nanowire with a p-n junction in the radial direction would enable a decoupling of the requirement for light

absorption and carrier extraction into orthogonal spatial directions. Each nanowire would be sufficiently long in the direction of incident light in order to have a higher light absorption, but sufficiently thin in another dimension to facilitate radial collection of carriers.

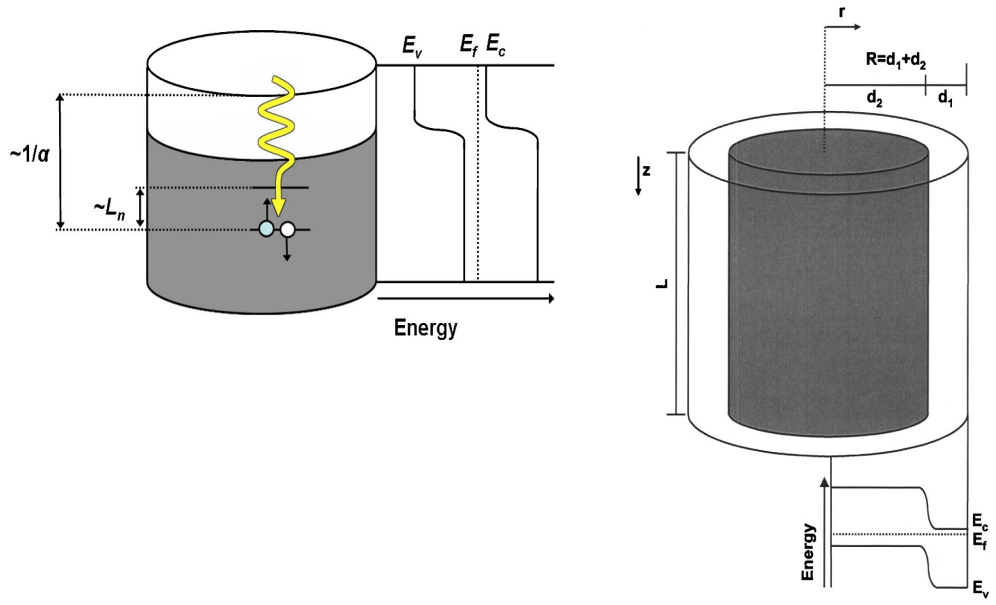

(a) (b)

Figure 16 Schematics of (a) planar pn junction solar cell and (b) nanowires radial p-n junction

The optimal wire dimensions are obtained when the wire has a radius approximately equal to carrier diffusion length, and their doping level must be high enough to be sure that a rod with small radius is not fully depleted. The length approximately equals to the optical thickness. Such a wire geometry device allows excellent optical absorption and high carrier-collection efficiency even using low-quality Si, leading to lower material cost in Si PV cells.

Garnetee *et al.*[53]described the fabrication of radial p-n junction solar cell using a low-energy, scalable process. They made n-type SiNW with aqueous electroless etching and deposited p-type amorphous Si (α-Si) by LPCVD, and subsequent crystallization with rapid thermal annealing. This solar cell has a lower efficiency, up to 0,5%. The low efficiency is due to the interfacial recombination and high resistance. Later, they dramatically reduced surface roughness (one way they proposed to reduce recombination) and improved the efficiency by a factor of 10. They also studied the light trapping effect in SiNW by changing the Si film thickness and SiNW length and found that there is a competition between improved absorption and increased surface recombination. For very thin absorbing layers,

the light trapping effect dominates over recombination. But for the thicker layer, the recombination effect is more important.[54]

Because of the recombination effect in SiNWs, it is necessary to passivate it before forming p-n junction. Researchers in Stanford passivated their hybrid Si microwire radial junction solar cell by adding intrinsic polysilicon films. They increased the efficiency from 7% to 9%, i.e. a relative enhancement of 30%. Furthermore, they passivated the top surface of pin junction by depositing thin α-SiN:H films and further increased the efficiency to 11%, i.e. an increase of 20%.[55]

1.3 Nanoparticles and quantum dots

Nanoparticles, quantum dots have been implemented in various solar cell application to advance solar conversion techniques. Quantum dots are nanocrystals with diameters which are smaller than Bohr radius. Their excitons are confined in a three spatial dimensions, which leads to quantum confinement. Fig.17 shows the splitting of energy level quantum dots. When the quantum confinement effects are completely dominant, the energy levels split up. By varying the radius of QDs, the quantum confinement energy of exciton can be controlled, leading to changes of the optical properties.

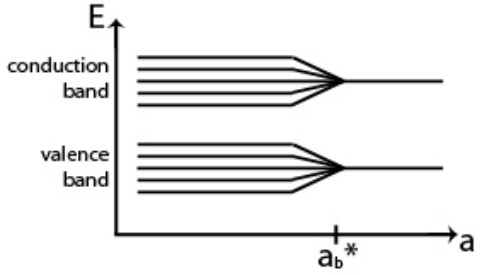

Figure 17 Splitting of energy levels for small quantum dots. The horizontal axis is the radius of the quantum dots and ab* is the Exciton Bohr radius.

There are generally two broad classes of QD used in solar cells: inorganic colloidal quantum dots in an organic matrix and epitaxial or vapor-phase grown crystalline QDs. The first class can be used for multi-exciton generation in DSSC and electrolyte-based solar cells. The second class includes III-V materials and IV materials QDs.

Crystalline group IV quantum dots are grown using simple CVD or sputtering deposition. III-V quantum dots have been grown using epitaxy.[56] Typical dots, such as cadmium

selenide (CdSe), cadmium sulfide (CdS), indium arsenide (InAs) and indium phosphide (InP) can be synthesized from a three-component system composed of precursors, organic surfactants and solvents. A common method for colloidal QD formation is to rapidly inject the precursors containing the group II, IV, or VI species into a hot and vigorously stirred solvent. As a consequence, a great number of nucleation centers are formed, and the coordinating ligands in the hot solvent prevent particle growth. In order to narrow the size distribution, surface selective precipitations are used, because of the slow addition of precursors and subsequent centrifugation of the colloidal solution of particles. [57]

Because of the quantum confinement, QDs can be used in the third generation solar cell to increase the ultimate efficiency, such as intermediate band solar cell, hot-carrier solar cells, down-conversion and up-conversion, as discussed before.

Metallic nanoparticles that support surface plasmons can be used to increase the light absorption. There are two main basic mechanisms which have been proposed to explain the enhancement of light absorption: light scattering and near field concentration of light. The nanoparticles placed inside the absorbing layers will generate surface plasmons which produce evanescent waves by a strong coupling between an incident electromagnetic (EM) wave and the electrons of the conduction band of a metal. This coupling occurs when the frequency of an incident wave is equal to the frequency of the plasmon resonance. So the EMs around metallic particles increase, which make it possible to improve absorption in the surrounding medium. The resonance frequency varies according to the sizes of the nanoparticles, the material of the nanoparticles and the optical constants of the surrounding medium.[58-59]

Tan *et al.* implemented the self-assembled Ag NPs based plasmonic back reflector in thin film silicon solar cell.[60] Because of the strong light scattering of Ag NPs, the plasmonic back reflector can provide efficient light trapping, leading to a short circuit current as high as 15.1 mA/cm^2, without any deterioration of V_{oc} or FF.

Quantum dots are often not connected electrically, although they have strong and tunable optical absorption. One-dimensional nanowires can carry electrical currents and deliver optical energy to external circuits. It is expected that the combination of QD and NW will provide another option to modulate the performance of solar cells. It is known that the QD-NW complex has the ability to extract optical energy from QDs via the Förster energy transfer.[61] Fig.18 gives the schema of QD-NW complex and energy diagram.

Incident photons will generate excitons in QDs. If QDs and NWs are very close to each other, excitons in the QDs can excite NWs by coulombic transfer.

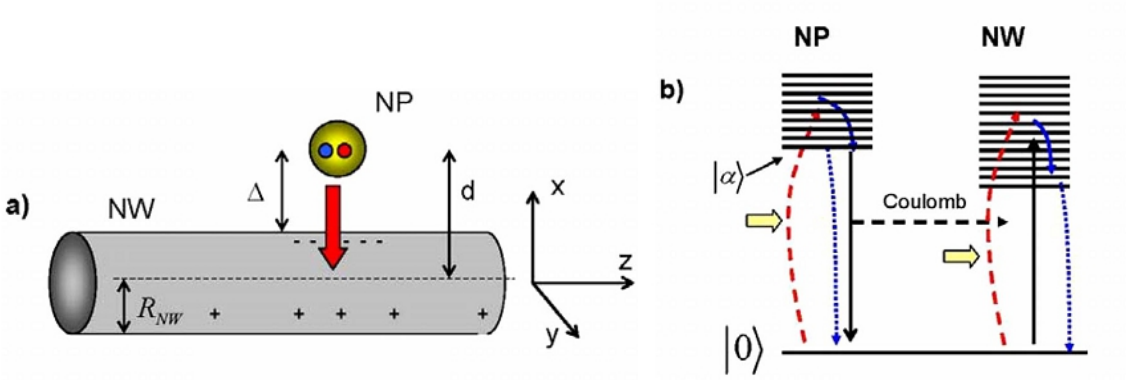

(a) (b)

Figure18 (a)Schematic of NP-NW complex. (b) Energy diagram of physical process

Hernández-Martínez *et al.*[61] studied the process of exciton transfer in SiNW-CdTe QD complex. Fig.19 shows the schematics of the complex and calculated enhacement of carrier generation in this complex as a function of QD-NW distance. This energy-transfer efficiency is proportional to $1/d^5$ (d is the distance between NWs and QDs). So it is expected that solar cells based on QD-NW complex will have high efficiency associated with increased absorption. However, so far, there is no experimental result which evidences a great enhanced solar cell efficiency associated with this effect.

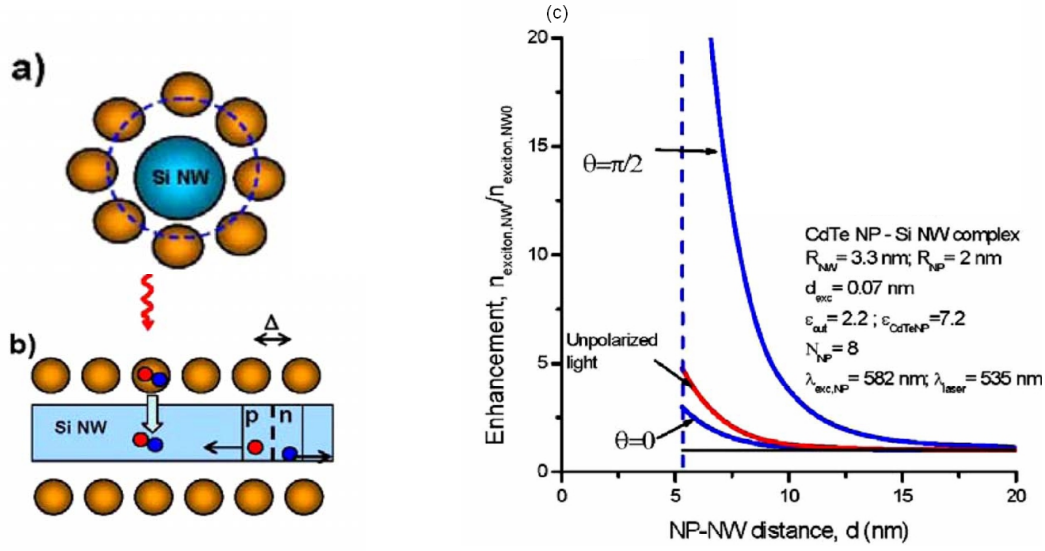

Figure 19 (a) and (b) Schematics of the complex. QDs form a shell around NW. And p-n junction inside the NWs will seperate photogenerated excitons. (c) Calculated ratio $n_{exciton,NW}/n_{exciton,NW0}$ for unpolarized light and polarized light for a SiNW-CdTe QD complex. Here, $n_{exciton,NW}$ and $n_{exciton,NW0}$ are the number of optically generated excitons inside a NW with and without QDs shell.

1.4 Scope of work

For planar p-n junction solar cell, the material must be thick enough to have enough absorption, whereas increasing the thickness increases the carrier recombination. In order to decouple the requirement of light absorption and carrier collection, nanopillars (or nanocones) radial p-n junctions are introduced. Nanopillars (or nanocones) have great light absorption and radial geometry offers minimal recombination if the diameter of nanopillars (or nanocones) is smaller than the minority carrier diffusion length.

This work focuses on the realization and characterization of low-cost Si nanostructures (nanopillars and nanocones) solar cells with sol-gel derived Al-doped ZnO (AZO) transparent electrodes. There are two things have to be taken into consideration: cost and efficiency. In order to decrease the fabrication price, silica balls and Langmuir-Blodgett techniques are used as the substitutes of photoresist and electrical beam lithography, respectively. Additionally, AZO thin film transparent electrodes are synthesized by low-cost sol-gel methods. In pursuit of high efficiency, on one hand, we have optimized the absorption of nanopillars and nanocones by varying their periods, diameters, lengths and sidewalls. On the other hand, we have optimized the electrical properties of AZO thin films by changing the synthesis parameters, such as doping concentration, baking temperature, annealing temperature and hydrogen treatment. At the end, solar cells have been realized based on optimized Si nanostructures and optimized AZO thin films. Associated with surface defects, surface passivation methods have been performed to reduce the defect concentration in n^+-i-p junction and to improve the efficiency of solar cells.

The organization of the manuscript is the following:

Chapter 2 introduces the experimental techniques used in this work, including the nanostructure fabrication systems, sol-gel techniques, solar cell integration process and relevant characterization equipments.

Chapter 3 investigates the influence of periods, diameters, lengths and sidewalls on the optical properties of nanopillars (or nanocones) both theoretically and experimentally. In order to understand the light absorption within nanopillars (or nanocones), we use finite difference time domain (FDTD) method to calculate their optical properties and we deduce general trends for the optimization of the solar cell efficiencies by varying the morphology of Si nanostructures (diameters, period, length of nanopillars or nanocones). By comparing their absorption spectra, Si nanostructures are optimized. At the end, we make a

comparison between experimental and calculated reflectance of nanostructural surface of Si.

Chapter 4 deals with the influence of doping concentration, baking temperature, annealing temperature and hydrogen treatment on the optical and electrical properties of AZO thin films. The optimized AZO films should have high transparency and low resistivity.

In chapter 5, the integration of solar cells devices is realized on planar and nanocones n^+-i-p junction and AZO films are used as top transparent electrodes. The effect of different passivation methods on the electrical properties of the solar cells is also investigated. Finally, the effect of AZO films on the optical and electrical properties of solar cells is evidenced.

Chapter 6 gives the conclusions and the prospects of the thesis.

[1]Tsakalakos. Nanotechnology for Photovoltaics. CRC press, 2010. (book)

[2] S. R. Wenham, M. A. Green *et al.* Applied Photovoltaics. Earthscan, 2007.(book)

[3] J. Nelson. The Physics of Solar Cells. Imperial College Press, 2003. (book)

[4] W. Shockley, H. J. Queisser. Detailed balance limit of efficiency of p-n junction solar cell. Journal of Applied Physics. 3, 32 (1961).

[5] S. Nara, Y. Sakaguchi. Newly developed multicrystalline silicon wafer with diffusion length over 250 μm. 3rd World Conference On Photovoltaic Energy Conversion, 2, 1483 (2003).

[6] O. Schultz, S. W. Glunz, G. P. Willeke. Multicrystalline silicon solar cells exceeding 20% efficiency. Progress In Photovoltaics: Research And Applications. 12, 553 (2004).

[7] M. A. Green, P. A. Basore *et al*. Crystalline silicon on glass (CSG) thin film solar cell modules. Solar Energy. 77, 857 (2004).

[8]J. Müllera, B. Recha *et al*. TCO and light trapping in silicon thin film solar cells. Solar Energy. 77, 917 (2004).

[9] G. Dingemans and W. M. M. Kessels. Status and prospects of Al_2O_3-based surface passivation schemes for silicon solar cells. Journal of Vacuum Science & Technology A. 30, 040802 (2012).

[10] B. Gorka. Hydrogen passivation of polycrystalline Si thin film solar cells. 2010. (thesis)

[11] R. E. I. Schropp, J. K. Rath, H. Li. Growth mechanism of nanocrystalline silicon at the phase transition and its application in thin film solar cells. Journal of Crystal Growth. 311,760 (2009).

[12] B. Rech, H. Wagner. Potential of amorphous silicon for solar cells. Applied Physics A. 69,155 (1999).

[13] S. R. Dhage, H. Kim *et al*. Cu(In,Ga)Se_2 thin film preparation from a Cu(In,Ga) metallic alloy and Se nanoparticles by an intense pulsed light technique. Journal of Electronic Materialsl, 40:2, 2011.

[14] W. C. Sinke and M. M. Wienk. Solid-state organic solar cells. Nature. 395, 544 (1998).

[15] U. Bach *et al.* Solid-state dye-sensitized mesoporous TiO_2 solar cells with high photon-to-electron conversion efficiencies. Nature. 395, 583 (1998).

[16] S. H. Lim, C. Lim *et al*. Toward interaction of sensitizer and functional moieties in hole-transporting materials for efficient semiconductor-sensitized solar cells. Nano Letters. 11, 4789 (2011).

[17] K. Yu, J. Chen. Enhancing solar cell efficiencies through 1-D nanostructures. Nanoscale Research Letters. 4, 1 (2009).

[18] M. K. Nazeeruddin, E. Baranoff *et al*. Dye-sensitized solar cells: a brief overview. Solar Energy. 85,1172 (2011).

[19] C. S. Ferekides, D. Marinskiy *et al*. High effciency CSS CdTe solar cells. Thin Solid Films. 361, 520 (2000).

[20] R. R. King, D. C. Law *et al*. 40% efficient metamorphic GaInP/GaInAs/Ge multijunction solar cells. Applied Physics Letters. 90,183516 (2007).

[21] G. Conibeer. Third-generation photovoltaics. Materials Today. 10,11(2007).

[22] T. Söderström, F. Haug *et al*. Asymmetric intermediate reflector for tandem micromorph thin film silicon solar cells. Applied Physics Letters. 94, 063501 (2009).

[23] J. Y. Kim, K. Lee *et al.* Efficient tandem polymer solar cells fabricated by all-solution processing. Science. 317, 222 (2007) .

[24] S. Wenger, S. Seyrling *et al*. Fabrication and performance of a monolithic dye-sensitized TiO_2/Cu(In,Ga)Se_2 thin film tandem solar cell. Applied Physics Letters. 94, 173508 (2009).

[25] A. Luque, A. Martí *et al*. Understanding intermediate-band solar cells. Nature Photonics. 6, 146 (2012).

[26] S. A. Blokhin, A. V. Sakharov *et al*. AlGaAs/GaAs photovoltaic cells with an array of InGaAs QDs. Semiconductors. 43, 4 (2009).

[27] W. Wang, A. Lin *et al*. Intermediate-band photovoltaic solar cell based on ZnTe:O. Applied Physics Letters. 95, 011103 (2009).

[28] R. D. Schaller and V. I. Klimov. High efficiency carrier multiplication in PbSe nanocrystals: implications for solar energy conversion. Physical Review Letters. 92, 18 (2004).

[29] J. J. H. Pijpers, R. Ulbricht *et al*. Assessment of carrier-multiplication efficiency in bulk PbSe and PbS. Nature Physics. 5, 811 (2009).

[30] J. F. Suyver, A. Aebischer *et al*. Novel materials doped with trivalent lanthanides and transition metal ions showing near-infrared to visible photon upconversion. Optical Materials. 27, 1111 (2005).

[31] J. Meijer, L. Aarts *et al*. Downconversion for solar cells in YF3:Nd3+, Yb3+. Physical Review B. 81, 035107 (2010).

[32] Y. Lambert, D. Zhou *et al*. Progressive multi-layer drop-casting of CdSe nanoparticles for photocurrent down shifing monitoring. Applied Physics Letters. 103, 051102 (2013).
[33] A. I. Hochbaum and P. Yang. Semiconductor nanowires for energy conversion. Chemical Reviews.110, 527 (2010).
[34] T. Xu, J. P. Nys *et al*. Growth of Si nanowires on micropillars for the study of their dopant distribution by atom probe tomography. Journal of Vacuum Science & Technology B. 26, 1960 (2008).
[35] W. H. Chen, R. Lardé *et al*. Study of the effect of gas pressure and catalyst droplets number density on Silicon nanowires growth, tapering, and gold coverage. Journal Of Applied Physics. 107, 084902 (2010).
[36] W. Chen,V. G. Dubrovskii *et al*. Boron distribution in the core of Si nanowire grown by chemical vapor deposition. Journal of Applied Physics. 111, 094909 (2012).
[37] J. M. Weisse, C. H. Lee *et al.* Fabrication of flexible and vertical Silicon nanowire electronics. Nano Letters. 12, 3339 (2012).
[38] J. M. Weisse, D. R. Kim *et al.* Vertical transfer of uniform Silicon nanowire arrays via crack formation. Nano Letters. 11, 1300 (2011).
[39] K. Peng and S. Lee. Silicon nanowires for photovoltaic solar energy conversion. Advanced Materials. 23, 198 (2011).
[40] L. Tsakalakos, J. Balch *et al*. Strong broadband optical absorption in silicon nanowire films. Journal of Nanophotonics. 1, 013552 (2007).
[41] T. Xu, Y. Lambert *et al*. Optical absorption of silicon nanowires. Journal of Applied Physics. 112, 033506 (2012).
[42] L. Hu and G. Chen. Analysis of optical absorption in Silicon nanowire arrays for photovoltaic applications. Nano Letters. 7, 11 (2007).
[43] D. H. K. Murthy, T. Xu *et al*. Efficient photogeneration of charge carriers in silicon nanowires with a radial doping gradient. Nanotechnology. 22, 315710 (2011).
[44] M. C. Putnam, D. B. Turner-Evans *et al*. 10 μm minority-carrier diffusion lengths in Si wires synthesized by Cu-catalyzed vapor-liquid-solid growth. Applied Physics Letters. 95, 163116 (2009).
[45] M. D. Kelzenberg, D. B. Turner-Evans *et al*. Photovoltaic measurements in single-nanowire Silicon solar cells. Nano Letters. 8, 710 (2008).

[46] B. Tian, X. Zheng *et al*. Coaxial silicon nanowires as solar cells and nanoelectronic power sources. Nature. 449, 885 (2007).

[47] J. Huang, C. Hsiao *et al*. Well-aligned single-crystalline Silicon nanowire hybrid solar cells on glass. Solar Energy Materials & Solar Cells. 93, 621 (2009).

[48] L. He, C. Jiang *et al*. Highly efficient Si-nanorods/organic hybrid core-sheath heterojunction solar cells. Applied Physics Letters. 99, 021104 (2011).

[49] Q. Shu *et al.* Hybrid heterojunction and photoelectrochemistry solar cell based on Silicon nanowires and double-walled Carbon nanotubes. Nano Letters. 9, 4338 (2009).

[50] T. Song, S. T. Lee *et al*. Silicon nanowires for photovoltaic applications: the progress and challenge. Nano Energy. 1, 654 (2012).

[51] V. Sivakov, G. Andrä *et al*. Silicon nanowire-based solar cells on glass: synthesis, optical properties, and cell parameters. Nano Letters. 9, 1549 (2009).

[52] B. M. Kayes and H. A. Atwatera. Comparison of the device physics principles of planar and radial p-n junction nanorod solar cells. Journal of Applied Physics. 97, 114302 (2005).

[53] E. C. Garnett and P. Yang. Silicon nanowire radial p-n junction solar cells. Journal of the American Chemical Society. 130, 9224 (2008).

[54] E. Garnetee and P. Yang. Light trapping in Silicon nanowires solar cells. Nano Letters. 10,1082 (2010).

[55] D. R. Kim, C. H. Lee *et al*. Hybrid Si microwire and planar solar cells: passivation and characterization. Nano Letters. 11, 2704 (2011).

[56] L. Tsakalakos. Nanostructures for photovoltaics. Materials Science and Engineering R. 62, 175 (2008).

[57] D. L. Ferreira, F. O. Silva *et al*. Size selective precipitation of CdSe colloidal quantum dots. AIP Conference Proceedings. 1199, 309 (2010).

[58] H. A. Atwater and A. Polman. Plasmonics for improved photovoltaic devices. Nature Materials. 9, 205 (2010).

[59] K. R. Catchpole and A. Polman. Plasmonic solar cells. Optics Express. 16, 21793 (2008).

[60] H. Tan, R. Santbergen *et al*. Plasmonic light trapping in thin-film silicon solar cells with improved self-assembled silver nanoparticles. Nano Letters. 12, 4070 (2012).

[61] P. L. Hernández-Martínez and A. O. Govorov. Exciton energy transfer between nanoparticles and nanowires. Physical Review B. 78, 035314 (2008).

Chapter 2 Experimental techniques

This chapter presents the experimental techniques which have been used to realize Si nanopillars (or nanocones) solar cells in a low-cost and flexible way. Fig.1 is a schematic view of these solar cells. Nanopillars (nanocones) are obtained by etching Si wafer using silica balls as a mask, and then p-n junction (or p-i-n junction) is formed by depositing polysilicon on nanopillars (or nanocones). In order to transport electrons from p-n junction to the metal conduct, sol-gel derived transparent conductive oxide AZO (Al-doped ZnO) thin films are coated on the top of p-n (or p-i-n) junction. Adding AZO thin films will also decrease the reflection of solar cell because of its adaptive refractive index. Al electrode is deposited at the rear side of p-n (or p-i-n) junction, and Ti/Au electrodes with a U-shape are evaporated at the surface of AZO thin films subsequently.

So in general, the fabrication of a solar cell involves 3 steps:

(I) fabrication and characterization of Si nanopillars (or nanocones)

(ii) fabrication and characterization of AZO thin films

(iii) realization and characterization of final device

The purpose of this approach can be outlined as follows: a low-cost fabrication process, an optimization of the optical and electrical properties of Si nanopillars (or nanocones) and the addition of AZO films to increase the energy conversion efficiency of solar cells.

The details of each part will be discussed later.

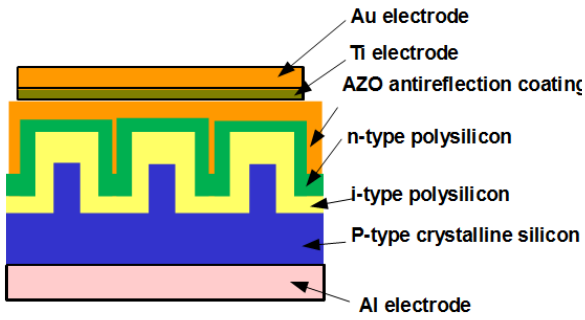

Figure 1 Si nanopillars p-n junction solar cell structure

2.1 Fabrication and characterization of Si nanopillars (or nanocones)

To begin with, we present the low-cost fabrication process of Si nanopillars (or nanocones), as illustrated in fig.2(a): first, silica balls used as masks are deposited on the planar p-type silicon substrate by Langmuir-Blodgett techniques (LB), as shown in fig.2(b);

secondly, reactive ion etching (RIE) is performed to reduce the silica ball, as shown in fig.2(c); thirdly, deep reactive ion etching (DRIE) and RIE are used to obtain cylindrical Si nanopillars (or nanocones), shown in fig.2(d); the last but not the least, silica balls are removed by hydrofluoric acid (HF), as shown in fig.2(e). The main advantage of this process is to use silica balls deposited by LB techniques as etching mask, rather than expensive photoresist and electron beam lithography (EBL) to achieve a low cost approach.

We can optimize the nanopillars (or nanocones) by changing their periods, lengths and diameters. The period of nanopillars (or nanocones) are determined by the sizes of silica balls. After shrinkage of silica balls, their size will decide the diameters of nanopillars (or nanocones), and by controlling the etching time of nanopillars (or nanocones), the length of them can be controlled.

Scan electron microscopy (SEM) is used to scan the morphology of the nanopillars (or nanocones) and UV-vis-infrared spectroscopy is performed to characterize their optical properties. By simulating the influence of period, length and diameter of the nanopillars (or nanocones) on the total absorption, we optimize the fabrication process in order to achieve the nanopillars (or nanocones) with high absorption.

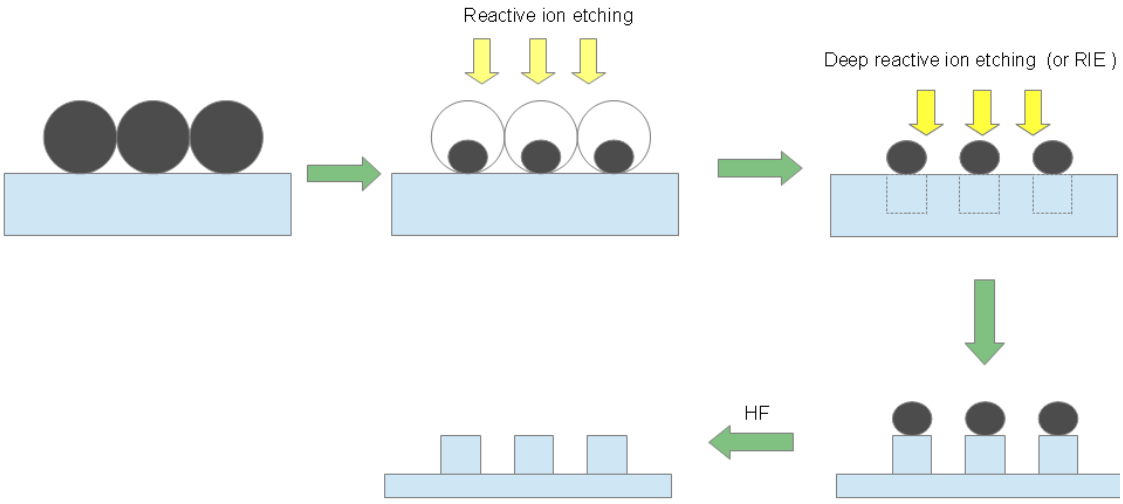

(a)

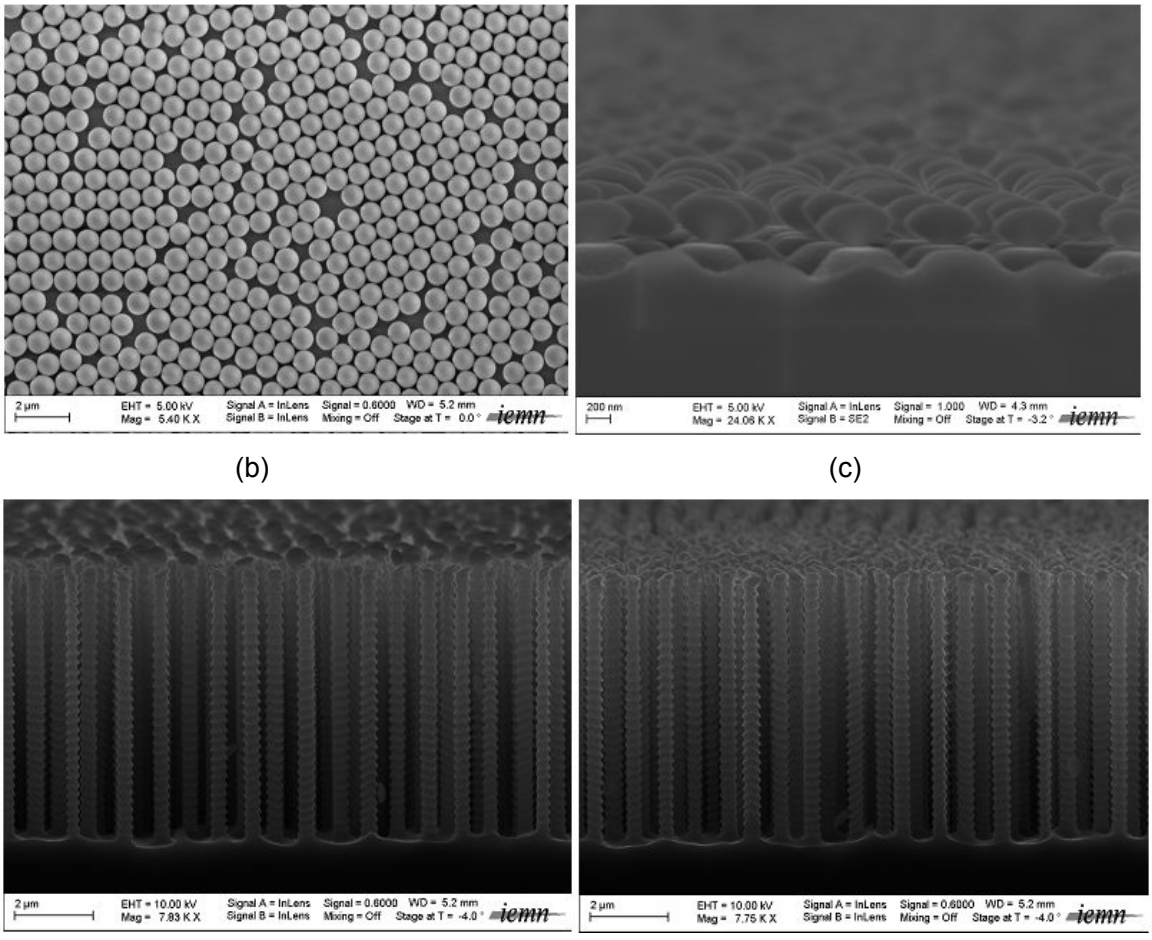

(b) (c)

(d) (e)

Figure 2 Schematic drawing of Si nanostructure fabrication process

2.1.1 Langmuir-Blodgett deposition

To fabricate nanopillars (or nanocones), masks with suitable sizes should be deposited on the substrate. In this work, we choose silica balls as mask and the Langmuir-Blodgett technique is used to deposit modified silica monolayer on the Si substrate, due to their lower-cost compared with photoresist and photolithography.

To determine the size of silica balls, the diameter of nanopillar (or nanocones) (d_0), the thickness of polysilicon (d) and the thickness of AZO films have to be taken into consideration. Indeed, as shown in fig.3, if the space between two nanopillars is equal or smaller than 2d, there will be no place to deposit AZO thin films which will transport electrons from p-n junction to the metal conduct. So in this work, two types of silica balls with the diameter of 880 nm and 380 nm bought from Gmbh Microparticles company, are used. To satisfy the needs of LB techniques and obtain amphiphilic silica balls, surface modification is required. The experimental process is :

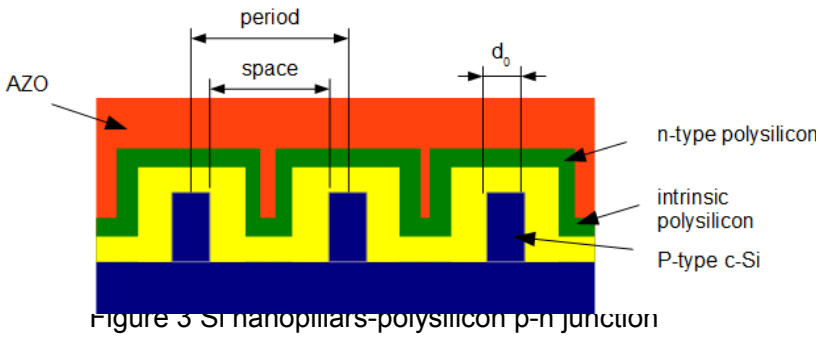

Figure 3 Si nanopillars-polysilicon p-n junction

(1) 1 mL of silica ball solution (5% in water) is centrifugalized at 5000 tr/min for 4 minutes. After that, the supernatant is removed and replaced by 1.5 mL of ethanol. This new solution is put in the ultrasonic bath to be well dispersed and then is centrifugalized again to remove the supernatant and replaced by ethanol.

(2) 10 µL of Aminopropyl-dimethyl-ethoxy silane is put into the solution to react with particles for 24 hours at room temperature.

(3) centrifugal and ultrasonic processes, as step (1), are repeated three times. The modified silica balls are diluted into the mixture of 250 µL ethanol and 250 µL chloroform.

Thanks to the amphiphilic nature of modified silica balls, when silica balls spread at the air/water interface, the hydrophilic group is immersed in the water and hydrophobic part is pointing towards air. The monolayer can be compressed by the barrier moving system,

meanwhile, the surface pressure is measured by electrobalance.

The most important indicator of the monolayer quality is given by the surface pressure as a function of the area per molecule, so called a surface press – area isotherm, as illustrated in fig.4. During the formation of the first monolayer, the monolayer phase transfers from gaseous state (relatively easy to compress) to the liquid state (relatively condensed). Upon further compression, the monolayer reaches the solid state (higher density). If the monolayer is further compressed, it will form the second layer, which will cause a sharp increase in the surface pressure.[1]

Silica balls can be transferred into the substrate by successively dipping the substrate down and up through the monolayer under a constant surface pressure (pressure of dip-coating as shown in fig.4.

In this technique, any contamination will lower surface tension, so the cleaning steps are performed before deposition process:chloroform, isopropanol and deionized water are used successively to wash the LB trough.

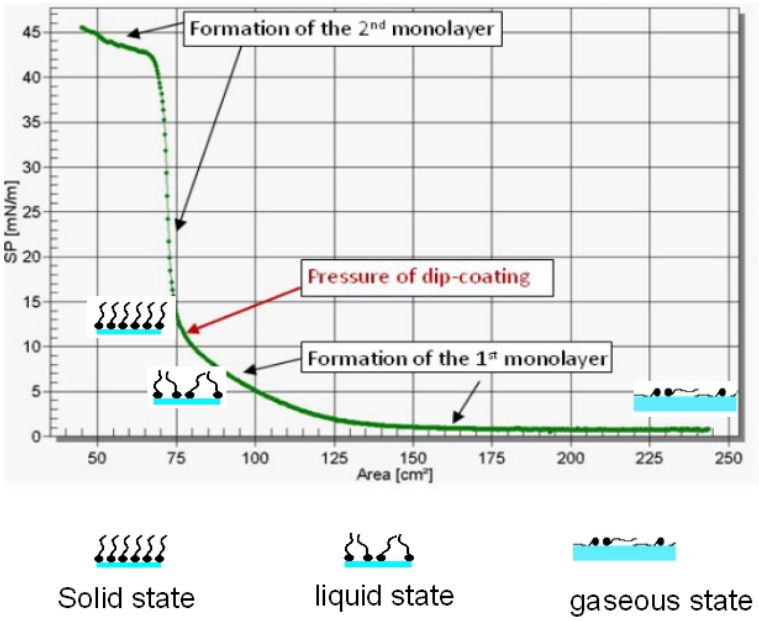

Figure 4 Surface pressure-area isotherm of silica ball

2.1.2 Dry etching (plasma etching)

In order to obtain nanopillars (or nanocones) with required diameters, silica balls are reduced by RIE plasma etchings system. Fig.5 shows the photography of RIE system.

Figure 5 Photography of RIE etching system in IEMN

The plasma in a RIE system is obtained by applying an electric field to the molecular gas in the chamber. The ions diffuse to the surface of the sample and are absorbed to produce volatile compounds which are desorbed and diffuse into the chamber, so the material is etched.

The etching process contains chemical etching and physical etching

-chemical etching: so called isotropic etching, whose etching mechanism is a reaction between ions and samples

-physical etching: so called anisotropic etching, due to the ions with higher energy, which bombard the samples and break it. This etching process will always happen along with the chemical etching.

In this work, we use CHF_3 and O_2 to etch silica balls, the parameters of the plasma are given in table 1. Fig.6 shows the morphology of reduced silica balls with different parameters. The variation of power and pressure will result in the configuration change of silica balls. The reduced balls with parameter d (in table 1) is an ellipsoid and others are spheres.

	CHF_3(sccm)	O_2(sccm)	Power (W)	Pressure (mTorr)
a	40	8	50	300
b	40	8	70	350
c	40	8	100	550
d	40	8	100	250

Table 1 RIE parameter for etching silica balls

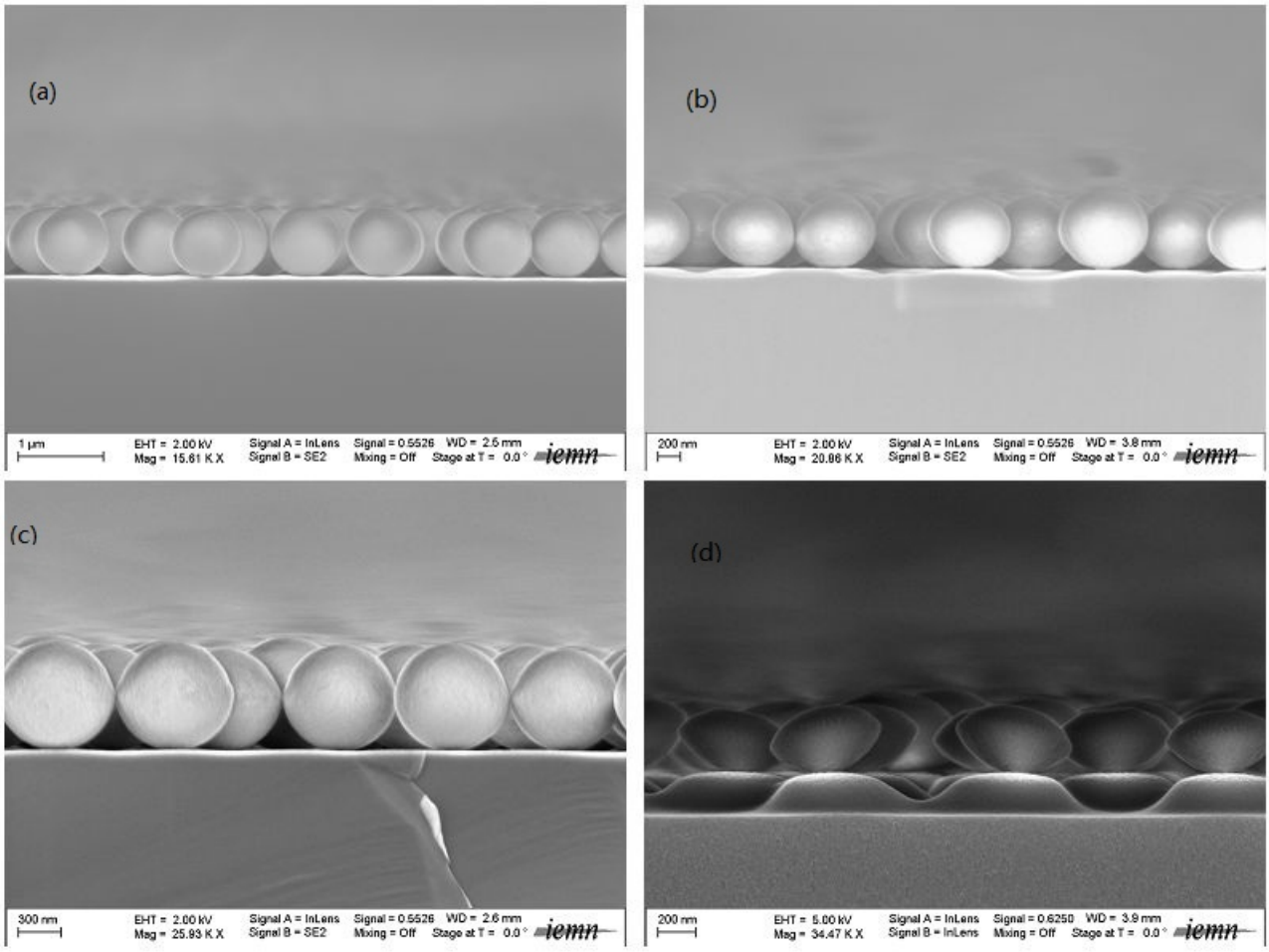

Figure 6 SEM images of reduced silica balls with different etching parameter, images(a), (b), (c) and (d)correspond to parameters a,b,c,d in table 1, respectively.

Fig.7(a) compares the anisotropy factor (horizontal length divided by vertical length) of reduced silica balls as a function of etching time. The parameters are labelled following table 1. A general trend can be observed, i.e. the anisotropy factor increases with time. There are two different regimes in the figure: one with fast increasing rate and another with slow increasing rate. In the first regime, the samples are etched using parameters with high power (100 W, 70 W) and low pressure (250 mTorr). In the second regime, the

samples are etched using parameters with low power (50 W, 70 W) and high pressure (300 mTorr, 350mTorr and 550 mTorr). If the pressure increases, we can assume that the attack of the plasma ions are everywhere (top, lateral) and the anisotropic factor is weak. With low pressure, the attack is mainly on top and thus, anisotropy increases.

Fig.7(b) shows the etching rate of different recipes with different pressure and power. It can be seen that vertical etching rate is always greater than horizontal rate and both of them increase with the increase of power. However, when the pressure is too high (500 mTorr) and gas fluxes are not changed, in order to obtain this high pressure in the chamber, it is necessary to have the valve (where gases are pumped out) closed, which means produced gas (a mixture of plasma ions and removed silicon oxide) can not be removed from the chamber quickly. This will decrease the etching rate. The anisotropic etching parameter with pressure of 250 mTorr and power of 100 W shows fastest etching rates than other anisotropic etching parameters. So we use this anisotropic etching parameter d to reduce the silica balls quickly.

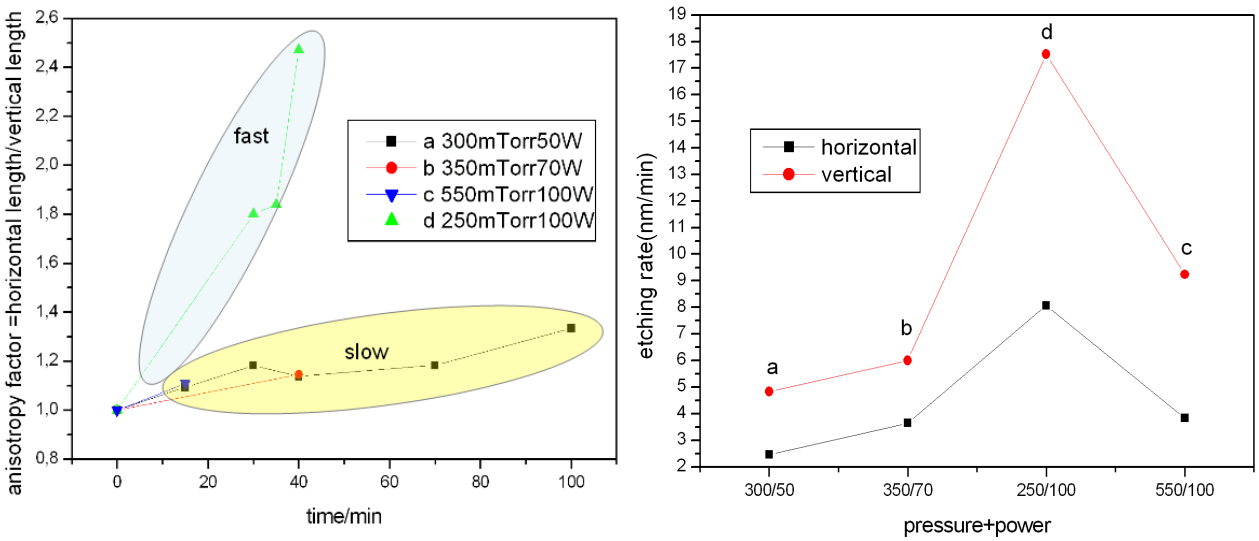

(a) (b)

Figure 7 (a) Anisotropy factor as the function of etching time, horizontal length and vertical length are labelled (b) etching rate of different recipes with different power and pressure

Silica balls have been reduced to a required size, and DRIE etching and RIE etching are subsequently used to fabricate nanopillars and nanocones, respectively. The main techniques of DRIE used in this work is Bosch process, which is also called time-multiplex etching process, alternating between etching step and passivation step and then repeating them until the required length is reached. Passivation step is done with a mixture of SF_6

and O_2, This step will deposit polymer on the surface, protecting the sidewall from etching. But etching step will completely remove polymer on the bottom and partially remove the polymer on the sidewall.[2] This process produces structure with highly anisotropy at a higher etch rate, but the drawback is the scallop profiles sidewall, as illustrated in fig.8(a). The etching parameters are shown in table 2.

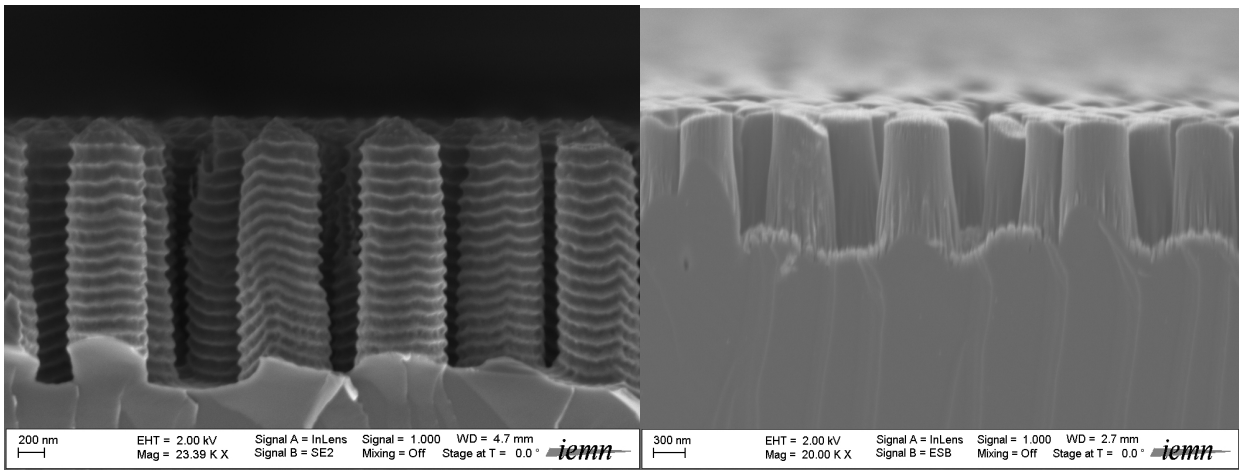

(a) (b)

Figure 8 SEM image of Si naopillars made by (a) DRIE etching and (b) ICP etching.

Etching time(s)	SF_3(sccm)	O_2(sccm)	EtchingPower(W)
2	450	45	2100
Passivation time(s)	CHF_3(sccm)	Passivation Power(W)	
2.6	200	2000	

Table 2 DRIE parameter for fabricating Si nanopillars

ICP-RIE systems is RIE system with ICP generator applying a high density of ions which enhances the etching rate, along with RF generator to supply an electrical field near the sample to increase the degree of anisotropy. In this work, Cl_2 is used to fabricate Si nanopillars, as shown in fig.8 (b).The etching parameters are shown in table 3.

Cl_2(sccm)	pressure(mTorr)	Power(W)
30	10	40

Table 3 ICP parameter for fabricating Si nanopillars

RIE system is used to fabricate nanocones in this work, the etching parameters are shown in table 4. Fig.9 is an illustration of the morphology of nanocones obtained by RIE

etching.

CHF_3(sccm)	O_2(sccm)	Power(W)	Pressure(mTorr)
40	8	100	250

Table 4 RIE parameter for fabricating Si nanocones

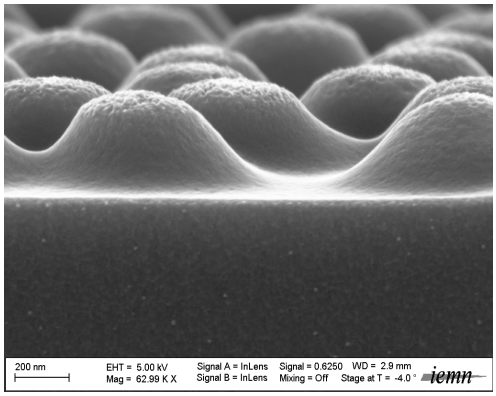

Figure 9 SEM image of Si nanocones made by RIE etching

After etching, we remove the remaining silica balls by immersing them into HF solution (50%HF) for 30 s.

2.1.3 Scan electron microsocopy

In this work, SEM Zeiss ultra 55 is used to obtain morphology image of a sample by scanning it with a focused electrons beam. Field emission gun (FEG) is used to produce electron beam. The signals are produced by the interaction between electrons beam and the atoms in the sample. The detector will detect the signal emitted from the sample to produce an image.

There are two different kinds of detector associated with different signals.

-secondary electrons (SE) detector: In-lens SE detector (so called immersion-lens) is immersed in the electrical field, which will collect SE signals with high spatial resolution information.

-back-scattered electrons (BSE) detector: BSE are electrons reflected from the sample by elastic scattering. The intensity of the signal will be proportional to the atomic number of the sample, so the BSE image shows the information about the distribution of elements of the sample.

2.1.4 UV/Vis/NIR spectroscopy

Cary 5000 ultraviolet-visible-infrared spectroscopy equipped with integrating spheres was used in this work to measure the total reflectance of nanopillars (or nanocones). Thanks to the integrating spheres, as shown in fig.10, which is a hollow sphere with its interior covered with a diffuse white reflective coating, such as magnesium oxide (MgO) or barium sulfate ($BaSO_4$), the total light reflected from the sample in all directions can be measured precisely (I). The reflectance (R), usually expressed as a percentage, is the ratio (I/I_0), where I_0 is the intensity of light reflected from reference. Fig.11 gives an example of the reflectance spectrum measured by UV/VIS/NIR spectroscopy with integrating sphere.

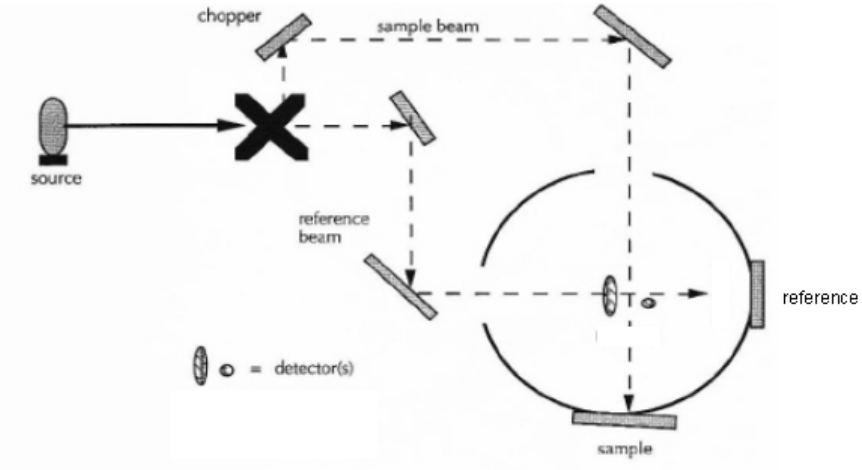

Figure 10 Schematic of spectroscopy with integrating sphere

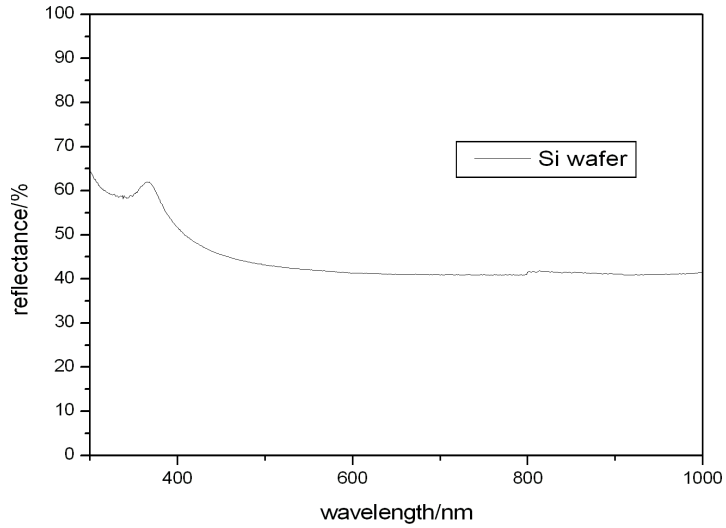

Figure 11 Reflectance spectrum of Si wafer measured by spectroscopy with integrating sphere

Because the transmission of the specimen in the range of 300 nm to 1000 nm is very small, so it can be neglected. The absorption in this region is equal to 1-R. For photovoltaic application, the larger the absorption of Si nanopillars (or nanocones), the better. So Si nanopillars (or nanocones) can be optimized by selecting the larger absorption or smaller reflectance.

2.2 Fabrication and characterization of AZO thin films

To transport electrons from nanopillars (nanocones) p-n junction to front metal electrodes, we use transparent conductive oxide AZO thin films, which can reduce the reflection of solar cell, thanks to the adaptive refractive index of AZO films. Sol-gel technique is used to produce AZO thin films here, because this technique allows to prepare large-area coating in ambient condition in a low cost way, and the optical and electrical properties of sol-gel derived AZO films are tunable by varying the fabrication parameters. Moreover, sol-gel deposition leads to conformal AZO layer on nanostructured surfaceas, a key advantage compared to sputtering deposition. As the substitute for ITO (indium tin oxide), AZO films are supposed to exhibit transparency (above 80% in the visible range) and the resistivity comparable to ITO (typically in the order of 10^{-3} Ωcm).

UV-VIS-NIR spectroscopy is applied to characterize the optical properties of AZO films, and hall effect measurement is used for measuring the electrical properties of AZO thin films. By changing the fabrication parameters and comparing the transmittance spectra and resistivity of AZO thin films, the fabrication parameters are optimized.

2.2.1 Sol-gel techniques

Sol-gel technique is widely used to fabricate materials (typically metal oxides) from sol (colloidal solution) to gel containing either particles or network polymers. Typical precursors are easily hydrolyzable metal compounds (metal inorganic salts or matal alkoxides). After hydrolysis and polycondensation reaction, precursors form a colloidal suspension, which will solidify a new phase (gel).

Fig.12 shows the main steps of sol–gel process:

(1) Synthesis of precursors: zinc salt, solvent, additives and dopant are put into a beaker. The mixture is stirred at 60 °C for 60 mins by magnetic stirrer.

(2) Preparation of sol: the precursors are left to age in a sealed bottle at room temperature for 48 hours.

(3) Preparation of xerogel film: the sol is deposited onto the substrate by spin-coating with the speed of 3000 r/min for 30 s. Subsequently, the substrate with thin film is baked on a hot plate for 10 mins. Repeating these steps until the require thickness (250 nm, 10 layers for the sol with Zn^{2+}concentration of 0.8 mol/L, 20 layers for the sol with Zn^{2+} concentration of 0.17 mol/L) is obtained. In this work, there are two substrates, quartz and silicon covered with 500 nm silicon oxide films, used in optical and electrical measurements, respectively.

(4) Fabrication of AZO dense film: the sample is annealed at a higher temperature in ambient atmosphere for 1h. Fig.13 shows the furnace temperature as a function of time in this work. The heating rate keeps constant (1 °C/min) in different experiments, since this slow rate prevents crack formation. For the sake of lower resistivity, hydrogen treatment is performed afterward.

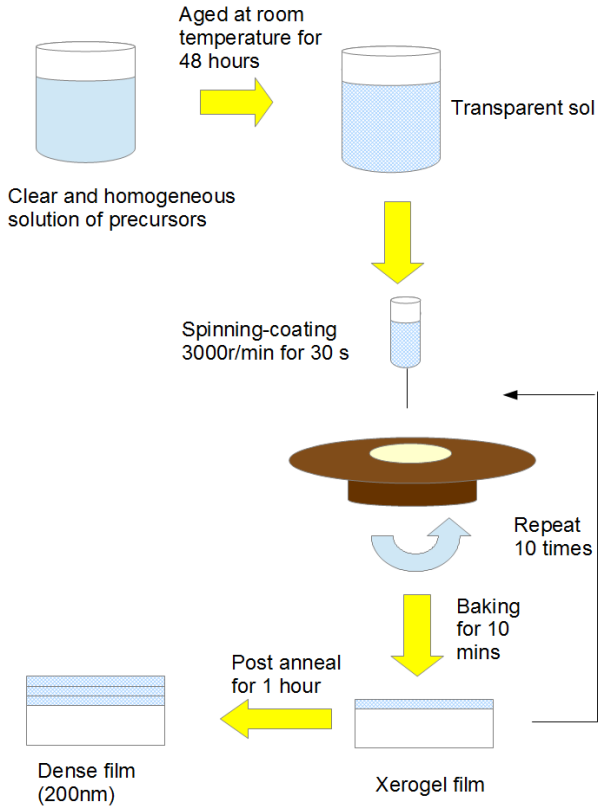

Figure 12 Schematic diagram of sol-gel process

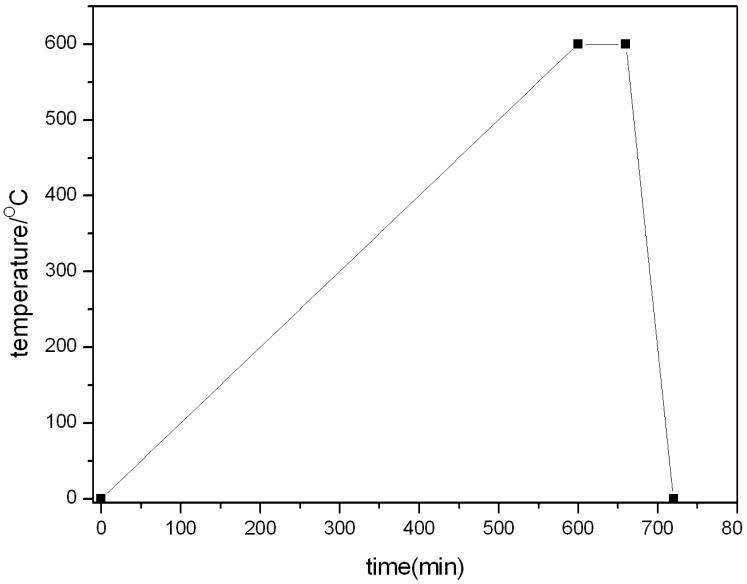

Figure 13 Temperature as a function of times during heat treatment

The process involves several parameters: (1) the nature and concentration of the precursor, solvent, additives and dopant, (2) the baking and post-heat treatment of the materials, (3) hydrogen treatment. These parameters govern the optical and electrical properties of AZO thin films.

In this work, precursor is zinc acetate dihydrate ($Zn(CH_3COO)_2.2H_2O$), because its acetate groups can be decomposed and produce combustion volatile by-products. The concentration of zinc salt (0.8 mol/L and 0.17 mol/L) have an effect on the optical properties of AZO film, as shown in fig.14(a). Lower concentration (0.17 mol/L) results in a higher transmittance of thin film in the ultraviolet region while it results in a lower transmittance in the visible region which is a more important region in photovoltaic application. So here the concentration of 0.8 mol/L is used.

Before choosing solvent, we compare the transmittance of AZO films using different solvent, as represented in fig.14(b). It can be observed that sample using 2-methoxyethanol as a solvent have higher transmittance. So we use 2-methoxyethanol in this work.

Additive, acting as a chelating ligand, is applied to form a stable sol by bridging two zinc atoms to avoid the rapid precipitation of Zinc hydroxide. Here, monoethanolamine (MEA) is used.[3]

This work is focused on the influence of doping concentration, baking temperature, post-treatment and hydrogen treatment on the optical, electrical properties of AZO films.

By optimizing these parameters, we expect to obtain AZO films with high transparency and low resistivity.

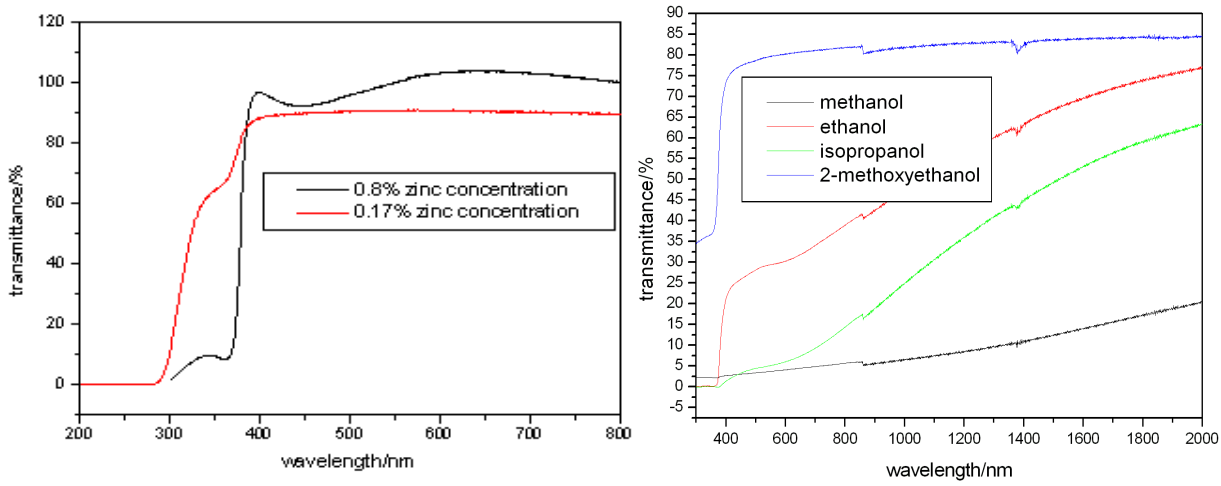

Figure14 (a) Transmittance spectra of AZO film with different Zn concentration (b) Transmittance spectra of AZO film using different solvent

2.2.2 UV/Vis/NIR spectroscopy

UV-VIS-NIR spectroscopy is used to measure the transmittance of the AZO films deposited on quartz. In this system, the light is split into two beams, one beam is used as the reference (I_0) and another beam will pass through the sample (I), the ratio (I/I_0) is called transmittance (T), which is usually expressed as a percentage (%T). Fig.15 shows the transmittance spectrum of quartz. It can be seen that quartz is transparent in the range from 300 nm to 1000 nm.

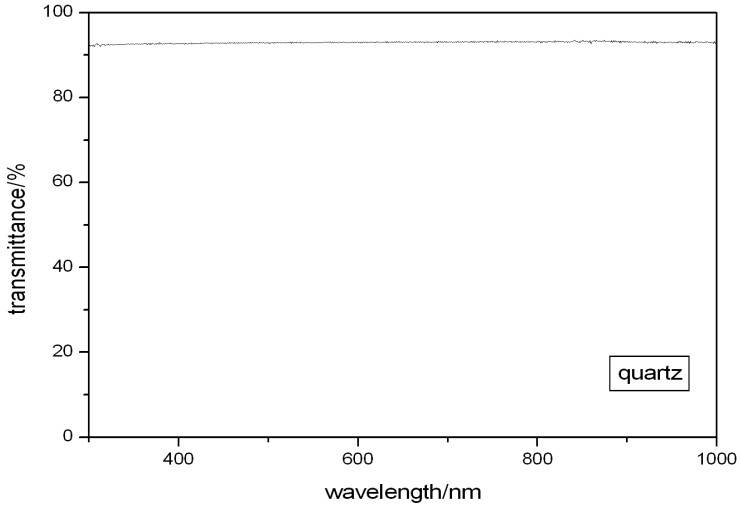

Figure 15 Transmittance spectrum of quartz

2.2.3 Hall effect system

In this work, electrical properties of AZO thin films are measured by Hall effect system. When a perpendicular magnetic field is applied to an electric current, due to the lorentz force, the electrons move to the left side or holes move to the opposite side and create an electrical field, which give the moving carriers a force against lorentz force. In steady-state, this electrical field will be strong enough to balance out lorentz force, so the carriers will move without deviation. It is the so called hall effect.

In order to diminish error, suitable geometry is required during this measurement. Sample geometry (van der pauw geometry) for hall effect system is shown in fig.16.

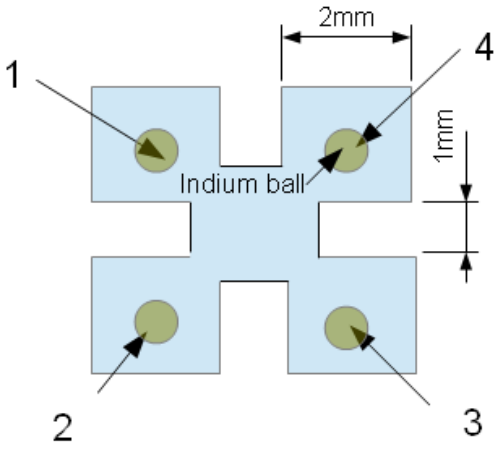

Figure 16 Van der pauw geometry

Sample preparation: first, AZO films are deposited on SiO_2 /Si substrate; second, depositing photoresist (S1818) with the thickness of 1.5 μm on AZO films; third, transferring patterns from mask to the sample by optical lithography and developing the sample with MF-319 developer in order to reveal the clover pattern; next, obtaining the geometry by dry etching or wet etching (ammonium chloride solution (10 wt.%)); last, removing the photoresist. Four indium balls are melt down on the four squares of the samples to form four ohmic contacts, labeled 1,2,3 and 4 respectively, as shown in fig.16.

Resistivity measurement

The current (I_{12}) is sourced through 1 and 2 and the voltage drop (V_{43}) is measured between 3 and 4. Additionally, the current (I_{23}) is applied between 2 and 3 and the voltage drop (V_{14}) is measured between 1 and 4.

Two characteristic resistances R_A and R_B are calculated by the following expressions:

$$R_A = \frac{V_{43}}{I_{12}} \qquad R_B = \frac{V_{14}}{I_{23}}$$

R_A and R_B are related to the sheet resistance R_S through the van der pauw equation:

$$\exp\left(-\pi \frac{R_A}{R_S}\right) + \exp\left(-\pi \frac{R_B}{R_S}\right) = 1 \quad .$$

The bulk resistivity ρ can be calculated using $\rho = R_S d$, where d is the thickness of the thin film.

Hall effect measurement

Applying a constant magnetic field B perpendicular to the sample and a current (I_{13}) between 1 and 3, the voltage drop (V_{24P}) is measured between 2 and 4, which is equal to the hall voltage V_H. So the sheet carrier concentration can be calculated by: $p_s = \frac{BI_{13}}{qV_H}$ ($n_s = \frac{-BI_{13}}{qV_H}$), the bulk concentration is $p = \frac{p_s}{d}$ ($n = \frac{n_s}{d}$) and then the hall mobility $\mu = \frac{1}{(q * n_s * R_s)}$ can be obtained from sheet carrier concentration (p_s or n_s) and sheet resistance (R_S).[4]

2.3 Realization and characterization of solar cell

After optimization of the reflectance of Si nanopillars (or nanocones) and electrical properties of AZO thin films, solar cells are realized. Si nanopillars (or nanocones) are used to make radial p-n junction, which, as discussed before, can decouple the requirement for light absorption and carrier collection. Transparent AZO thin films are coated on p-n junction to transport electrons from p-n junction to metal contacts, and these thin films can reduce the reflectance of p-n junction due to the dielectric adaptation effect. In order to yield high efficiency, optimized nanopillars (or nanocones) with lower reflectance and higher absorption and optimized AZO thin films are used. The fabrication processes are shown in fig 17 (a):

(i) depositing n+-type polysilicon or intrinsic polysilicon on Si nanostructure (see fig.17 (b)) to form p-n junction or p-i-n junction, as shown in fig.17 (c).

(ii) depositing optimized AZO films as transparent electrode and antireflection layer, as shown in fig.17(d).

(iii) depositing metal contact on the front and rear side.

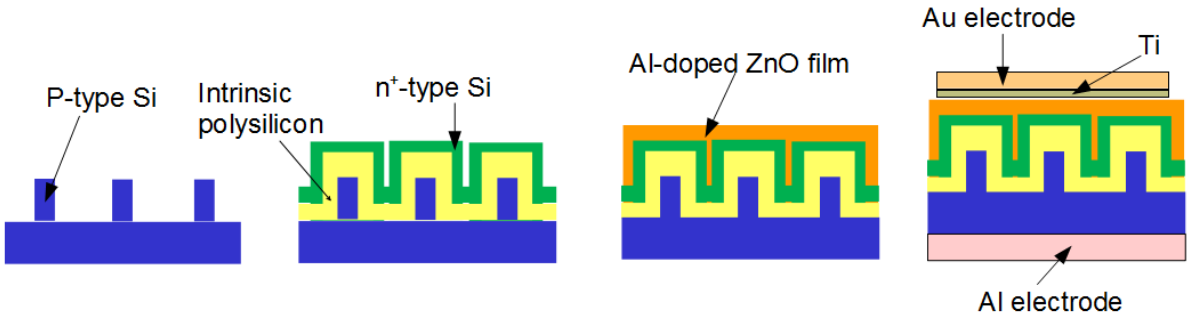

(a)

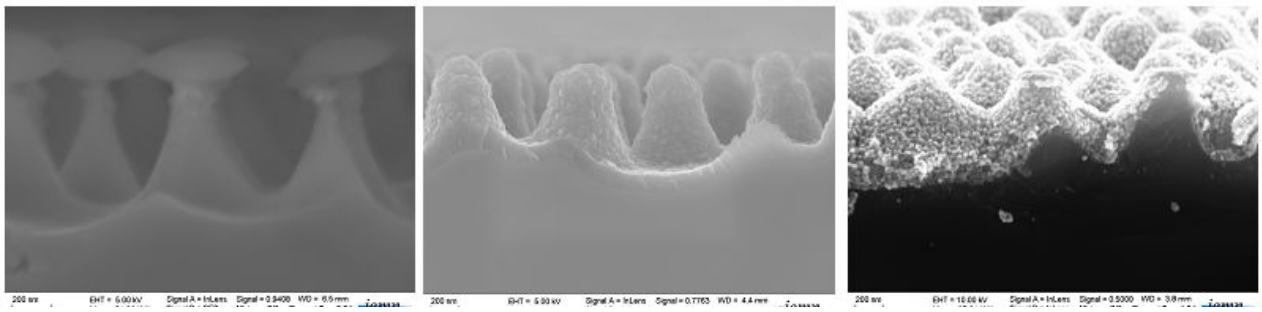

(b) (c) (d)

Figure 17. Schematic diagram of the fabrication process of solar cells

In this part, the reflectance of solar cells are measured by UV-VIS-NIR spectroscopy. The photoconductivity measurements are performed by photocurrent spectroscopy, and the efficiency of solar cells are measured by solar simulator.

2.3.1 Realization process

Polysilicon:

N+-doped polysilicon is deposited on p-type Si wafer or Si nanopillars (nanocones) to form n+-p junction. A majority of depletion region of n+-p junction is in p-type monocrystalline Si with less defects instead of polysilicon with defects associated with grain boundary. So, normally, the recombination of photocarriers is minimized. In order to increase the efficiency of solar cells, we add intrinsic polysilicon to form n^+-i-p junction. This n^+-i-p junction has a wider depletion region, so it can seperate more photogenerated

electron-hole pairs. Nevertheless, in order to reduce significantly the carrier recombination at the interface between polysilicon and monocrystalline Si, wet oxidation passivation method is used. Additionally, hydrogen passivation is performed to reduce the defects in polysilicon. These passivation methods will be presented in chapter 5.

LP-CVD (low pressure chemical vapor deposition), is used to deposit polysilicon. During the process, the wafer is exposed to one or more volatile precusors reacting with each other or decomposing on the wafer to obtain required materials.

In this work, SiH_4 is used to deposit intrinsic polysilicon layer, and SiH_4 and PH_3 are used to deposit phosphorus polysilicon layer. The parameters are shown in table 5.

	SiH_4(sccm)	PH_3(sccm)	pressure(mTorr)	temperature(°C)	resistivity(Ωcm)
instrinsic polysilicon	80		200	585	>10
n+-doped polysilicon	70	5	100	700	0.02

Table 5 CVD parameters for polysilicon deposition

Metal contact:

To complete the fabrication of solar cell, 100 nm titanium (Ti) and 500 nm gold (Au) are deposited in turn on the front side of the samples with a U shape (as shown in fig.18), and 200 nm aluminium is evaporated on the rear side of the samples.

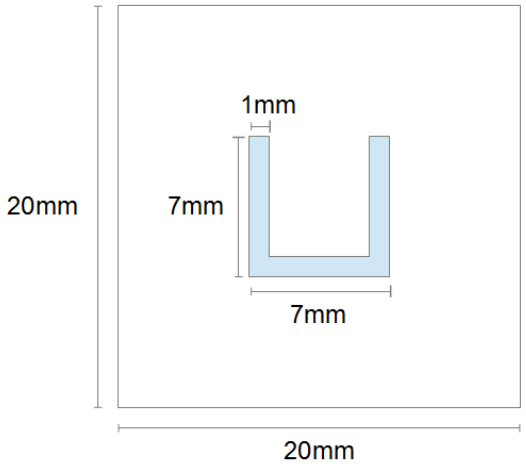

Figure 18 U shape mask for front metal contact

2.3.2 Photocurrent spectroscopy

To measure the photocurrent as a function of wavelength and photocurrent as a function of voltage, photocurrent spectroscopy is used, as shown in fig.19.

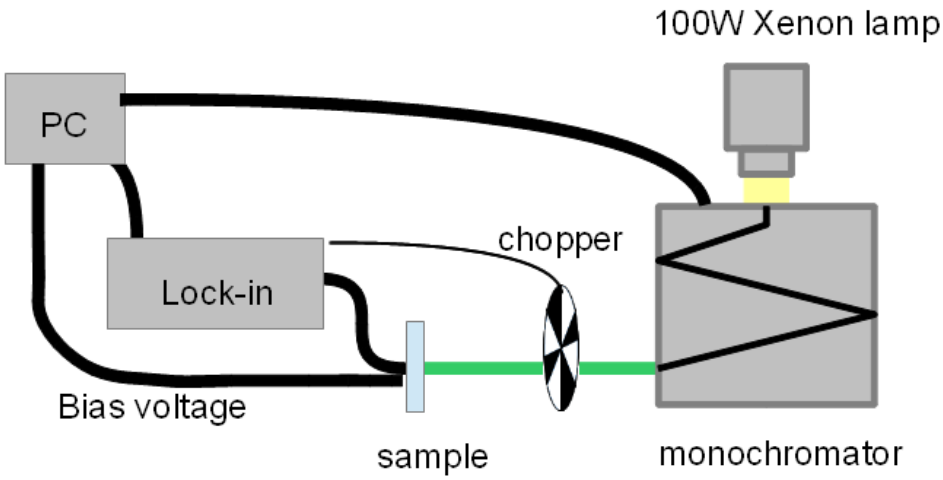

(a)

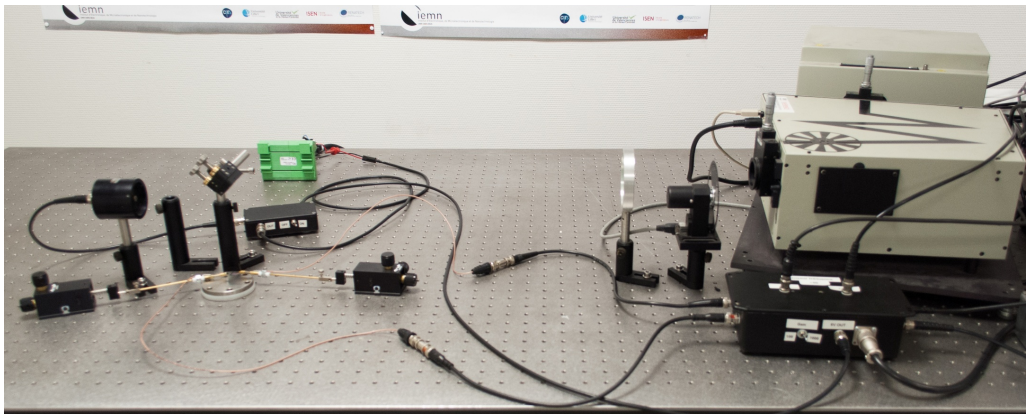

(b)

Figure 19 (a) Schematic and (b) photograph of the photocurrent spectroscopy

Light source used in this work is a monochromator with a 100 W Xenon lamp (range from 350 nm to 2500 nm). The light is chopped at the frequency of 32 Hz to decrease the influence of noise on the photocurrent. This photocurrent is detected by a synchronous model 7225 lock-in amplifier[5], with synchronized frequency of 32 Hz. To calibrate the photon flux emitted from the lamp, we use a thermopile detector, which measure the irradiance of the lamp. Hence, all the results are normalized. Fig.20 shows a typical photocurrent of the thermopile detector versus the energy of irradiation.

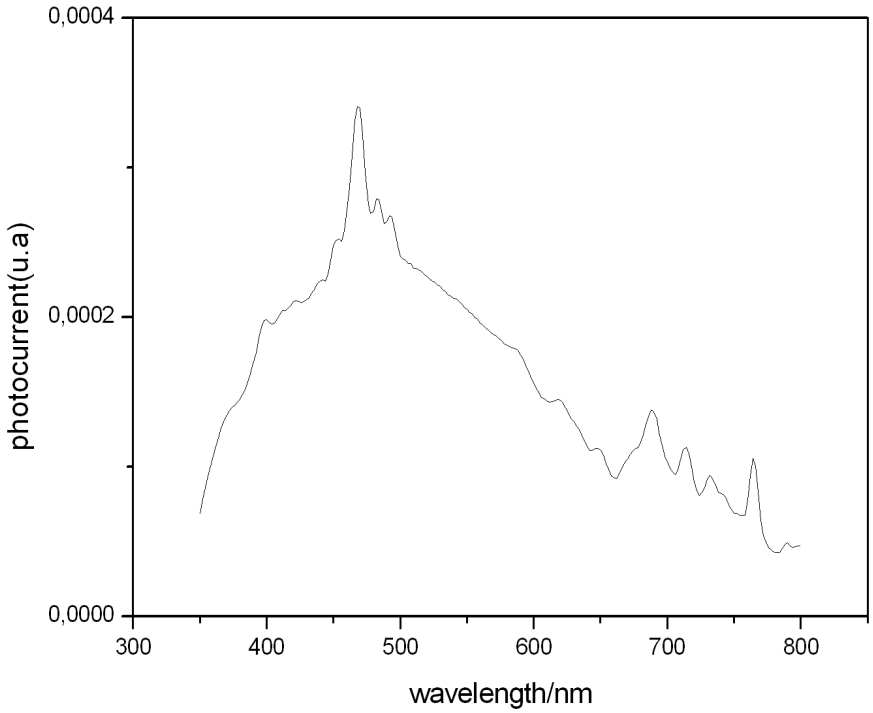

Figure 20 Photocurrent spectrum of the thermopile detector

2.3.3 Solar simulator

To know the efficiency of solar cell, Oriel Class AAA solar simulator is used. The system includes two parts:

(I) An illuminator housing (as shown in fig.21) with a built-in Xenon arc lamp, air mass 1.5 Global filter (AM 1.5G) and an integrated shutter; AM1.5 is typically used to characterize the performance of solar cell under standard condition. AM is air mass coefficient, expressed as a ratio of optical path (L) through the atmosphere at solar zenith angle of z to the path (L_0) at the zenith $AM = \frac{L}{L_0} \approx \frac{1}{\cos(z)}$ Number 1,5 represent the spectrum at mid-latitudes,where z=48,2º.[6] The AM1.5 Global spectrum is designed for flat plate modules and has an integrated power of 1000 W/m^2.

Figure 21 Photograph of solar simulator

(ii) I-V test station: Model 4200-SCS Semiconductor Characterization System is used to characterize the electrical properties using 4-wire probing, obtaining I-V curve and some critical parameters such as short circuit current (I_{sc}), current density (J_{sc}), open circuit voltage (V_{oc}), fill factor (ff), maximum output power (P_{max}), cell efficiency (η), and other standard photovoltaic cell parameters, as shown in fig.22.

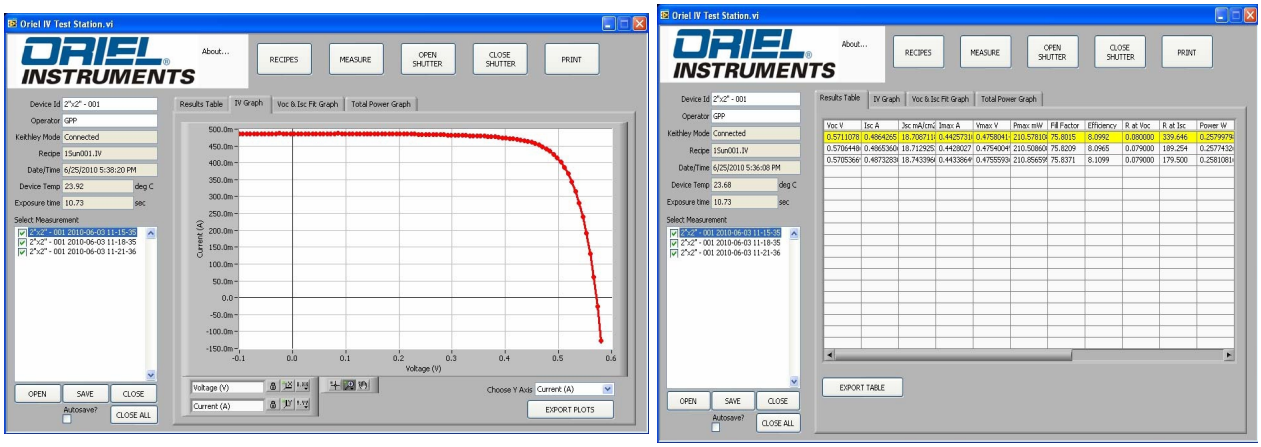

Figure 22 Graphs of measurements results using the Oriel® IV test station software

The I-V test station use the reference cell which consists of a solar cell and an electronic display, for calibrating the solar simulator power level, as shown in fig.23.

Figure 23 Photograph of reference cell and electronic display

Conclusion

We have described all the technical processes used to elaborate our samples, from simple nanostructured surface to solar cell devices. In the following chapters, we present detailed optimizations of Si nanopillars (and nanocones) by varying geometry parameters (diameter, period and length), and AZO films by changing operating parameters (doping concentration, baking temperatures, post-annealing temperatures and hydrogen treatment). Finally, we integrate solar cells and investigate the influence of passivation on the properties of solar cells in details.

[1] Langmuir and langmuir-blodgett films.KSV instruments. (Application note)

[2] B. Wu, A. Kumar *et al*. High aspect ratio silicon etch: a review. Journal of Applied Physics. 108, 051101(2010).

[3] L. Znaidi. Sol–gel-deposited ZnO thin films: A review. Material Science And Engineering B. 174,18 (2010).

[4] Test Methods for Measuring Resistivity and Hall Coefficient and Determining Hall Mobility in Single-Crystal Semiconductors. Active Standard ASTM F76.10.04 (2011).

[5] T. Xu, Y. Lambert *et al*. Optical absorption of silicon nanowires. Journal of Applied Physics. 112, 033506 (2012).

[6] L. Tsakalakos. Nanotechnology for Photovoltaics. CRC press, 2010. (book)

Chapter 3 Optical properties of Si nanopillars and nanocones

Due to the small absorption coefficient of Si, typical crystalline Si solar cells reach several hundreds microns of thickness to obtain high efficiency, which results in an increase of the cost. In order to obtain solar cells with low-cost and high efficiency, new conceptions are applied to thin film solar cells. Light trapping methods, such as surface texturing and surface nanostructuring, have been reported to increase the optical absorption and address this issue. Surface texturing randomizes the direction of light within the device and increases optical absorption by a factor of $4n^2$ (n is the refractive index of materials)[1]. Surface nanostructuring, such as nanowires (nanopillars) and nanocones, can trap light through a combination of multiple-reflection and increase concentration of light energy within the materials. Additionally, in radial p-n junction, each nanopillars (nanocones) allows for more carrier collection when they have a diameter of the order of the carrier diffusion length.[2-4] Such geometries promise high efficiencies at lower-cost than typical single crystalline Si solar cells, so they are promising building blocks which are incorporated into photovoltaic cell. However, the optical absorption depends on the structure parameters, such as filling factor, length, diameters and sidewalls.[3-7] So the optimization and theroretical understanding of optical absorption within SiNPs and SiNCs are critical in improving the efficiency of solar cells.

Optical properties of Si NWs or NCs arrays have been reported before. J.S.Li et al.[4] studied NPs arrays by varying diameters, periods and length. They showed that more efficient light absorption compared to the Si wafer with the same thickness was found when the period is between 250 nm and 1200 nm and the ratio of diameter (D) to period (P) is bigger than 0.5. The maximum efficiency is obtained when the ratio is D=0.8. It was also found that longer wires lead to higher efficiency with an optimized length of 20 μm[3]. However, long wires will increase the cost and also it will be difficult to deposit ZnO antireflection layer and make metal contact. It appears necessary to use an ideal wire length at least shorter than 5 μm.

In this work, we fabricated SiNPs and SiNCs arrays using dry etching. By changing the dry etching parameters, SiNPs and SiNCs with different diameters, length or sidewalls were obtained. SiNPs and SiNCs were tested by comparing their experimental reflectance spectra. The lower the reflectances are, the better SiNPs and SiNCs are. Owing to the

limitation of the system of characterization, it's impossible to obtain directly an experimental absorption spectrum. In order to understand the light absorption within SiNPs and SiNCs, we used home-made 3D finite difference time domain (3D-FDTD) method to calculate their optical properties. This method leads to the knowledge of the reflection, the transmission and the total absorption spectra of the nanostructured surface. Finally, we make a comparison between experimental and simulated results.

3.1 Influence of the structural parameters on the experimental optical properties

In this part, SiNPs with different diameters, D/P (where D is the diameter of SiNPs and P is the period), length and sidewalls are fabricated by top-down method. By comparing these reflectance spectra, the influence of these structure parameters on measured reflectance spectra are discussed.

Diameter

First, we discussed the influence of diameters on the optical properties. Fig 1 shows the SEM image of SiNPs with different diameters made by ICP etching, and their parameters are given in Table 1. These NPs have the same period of 380 nm and same length of 750 nm. The diameters were controlled by varying the shrinking time of silica balls, as shown in Chapter 2. Fig.2 presents the reflectance spectra of SiNPs of two diameters: 270 nm (D/P= 0.7) and 320 nm (D/P= 0.8) and Si wafer with same thickness in the wavelength range of 300 -1000 nm, which corresponds to the major spectral irradiance of sunlight. It is clear that nanopillars impart a significant reduction of reflectance compared to the solid film. It can be seen in fig.2 that diameters have an effect on the reflectance. The reflectance is ranged from 20%- 28% in the 300-1000 nm energy range when the diameter is 320 nm. When the diameter decreased to 270 nm, the reflectance is ranged from 15%-25%. So with the decrease of diameter, the reflectance decreased. When the SiNPs have the period of 380 nm and length of 750 nm, the best fabricated NPs have a diameter of 270 nm.

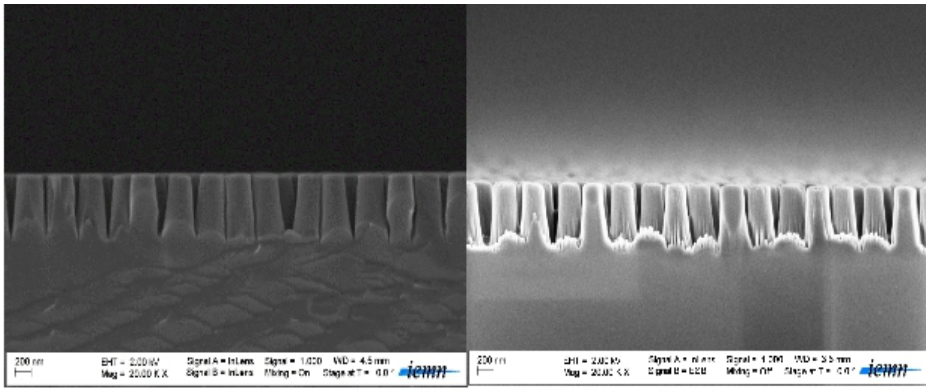

(a) (b)

Figure 1 SEM images of SiNPs with length of 750 nm, period of 380 nm and diameter of (a) 320 nm and (b) 270 nm

Samples	Diameters/nm	Period/nm	D/P	Length/nm
a	320	380	0.8	750
b	270	380	0.7	750

Table 1 Parameters of SiNPs corresponding to images a and b in fig.1.

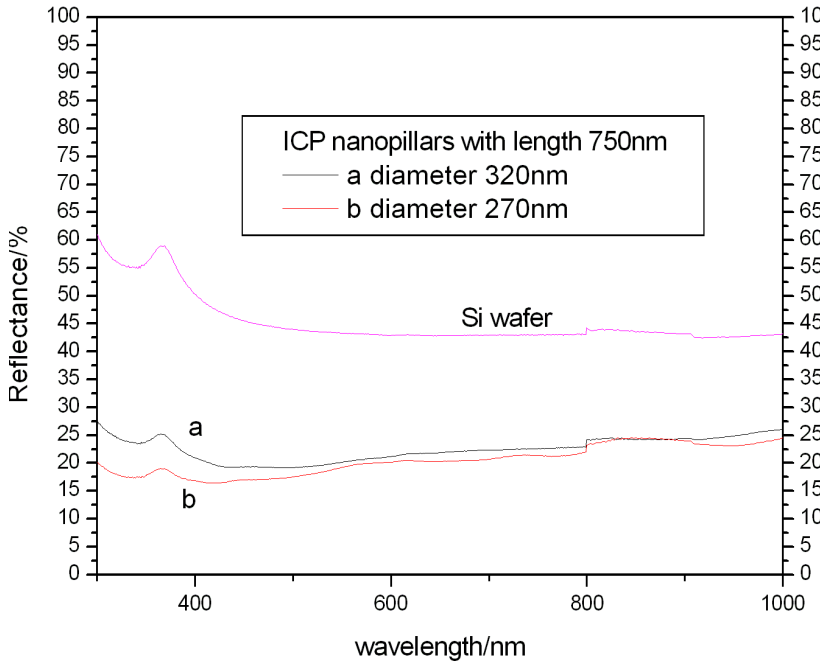

Figure 2 Total reflectance spectra from integrated sphere measurement for Si wafer and SiNPs with length of 750 nm, period of 380 nm and diameter of (a) 320 nm and (b) 270 nm.

D/P

Fig.3 shows the SEM image of SiNPs with different D/P made by ICP etching. This ratio can be changed by varying either the diameters or the periods. Table 2 gives the parameters of these SiNPs. They have the same length of 1300 nm and with D/P varying from 0.6 to 0.7. NPs with the diameters of 240 nm (with period of 380 nm) and 520 nm (with period of 880 nm) have the same ratio of 0.6. NPs with the diameters of 630 nm (with period of 880 nm) and NPs with the diameters of 320 nm (with period of 380 nm) have the ratio of 0.7 and 0.8, respectively.

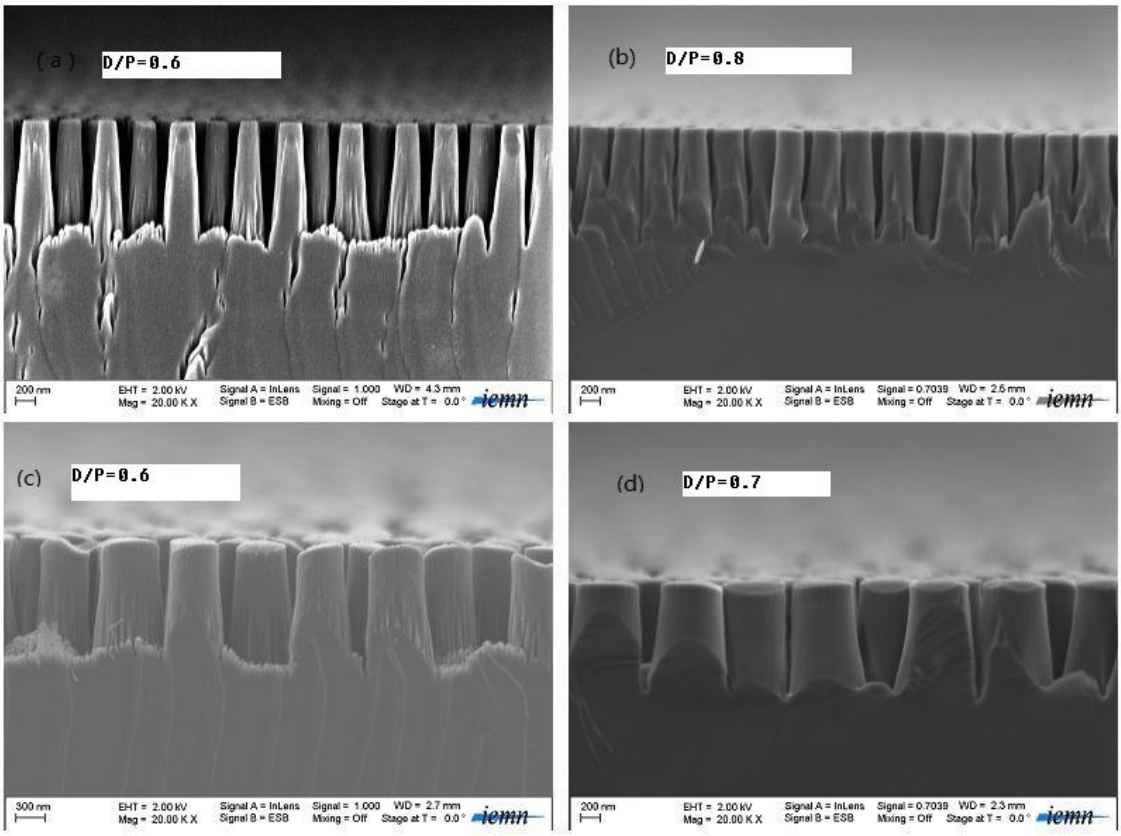

Figure 3 SEM images of SiNPs with length of 1300 nm, period of 380 nm and diameter of (a) 240 nm and (b) 320 nm, respectively. And SiNPs with length of 1300 nm, period of 880 nm and diameter of (c) 520 nm and (d) 630 nm, respectively.

Samples	Diameters/nm	Period/nm	D/P	Length/nm
a	240	380	0.6	1300
b	320	380	0.8	1300
c	520	880	0.6	1300
d	630	880	0.7	1300

Table 2 Parameters of SiNPs corresponding to images a, b,c and d in fig.3.

Fig.4 presents the corresponding reflectance spectra of these SiNPs in the wavelength range of 300 -1000 nm. In the range from 700 nm to 1000 nm, the reflectance spectra of SiNPs with different D/P are similar. However, in the range from 300 nm to 700 nm, SiNPs with the D/P=0.6 show clearly the smallest reflectance. When the ratio increases, the reflectance increases with a best fabricated NPs of D/P=0.6. Comparing the reflectance spectra of NPs with a same D/P=0.6, i.e. diameter of 240 nm with period of 380 nm and diameter of 520 nm with period of 880 nm, we can observe that the NPs with smaller diameters and smaller period present a lower reflectance.

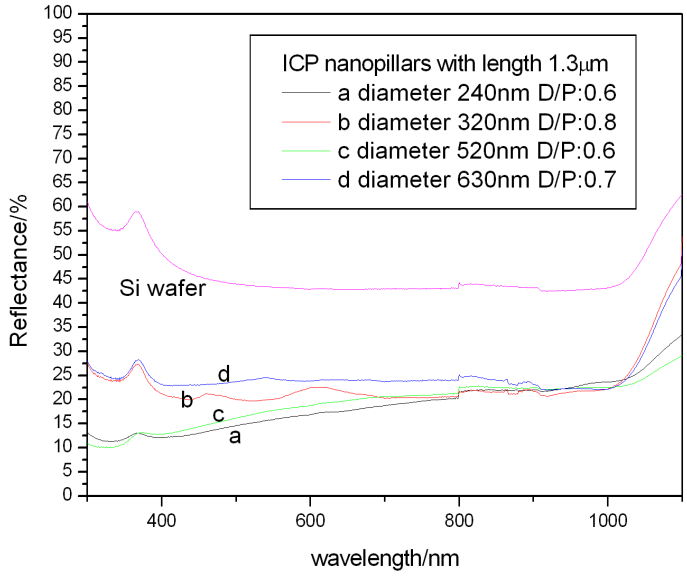

Figure 4 Total reflectance spectra for SiNPs film with different D/P, (a), (b), (c) and (d) are corresponding to the SiNPs in fig.3

Length

To study the influence of length on the antireflection characteristics of SiNPs, the total reflectance of SiNPs with different lengths have been measured. The length was controlled by varying the deep etching time. As shown in fig.5, the length of SiNPs obtained by ICP

etching increases linearly with etching time. The etching rate is equal to 55 nm/min.

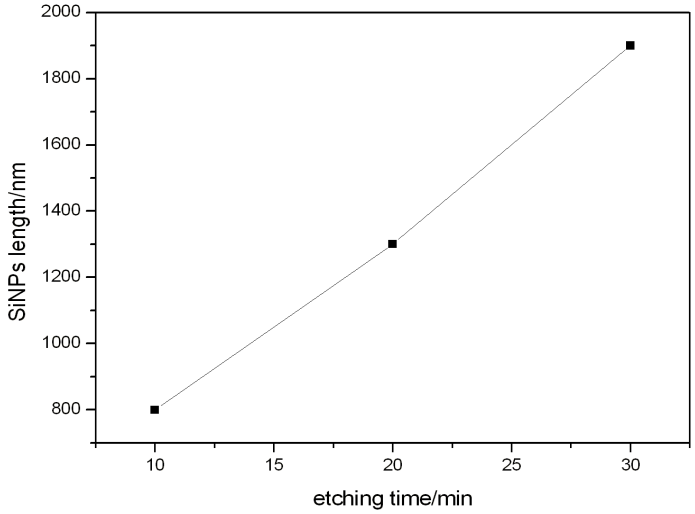

Figure 5 Length of SiNPs as a function of deep etching time

Fig.6 shows the SEM images of SiNPs with optimized diameter of 270 nm, period of 380 nm and lengths of 800 nm, 1300 nm and 1900 nm. Their parameter are shown in table 3. It can be seen that with the increase of etching time, the sidewalls are more tapered. This point has been already reported in other samples from literature[8] and this is due to the silica mask. The selectivity of Si to silica is about 26, so the mask erosion will increase the lateral etching. Moreover, during the etching process, the etched products are deposited, which decrease the etching rate from the top to the bottom of SiNPs, so tapered sidewalls can occur.[8] Fig.7(a) presents the correspondent reflectance spectra of SiNPs with different length in the wavelength range of 300 -1000 nm. Compared to the reflectance of Si wafer, the average reflectance of SiNPs with length of 800 nm decreases to 20%. For higher length, the reflectance decreases again. As shown in fig.7(b), the reflectance decreases linearly with the length. This behavior is linked to the fact that when the length increases, the amount of silicon increases as well.

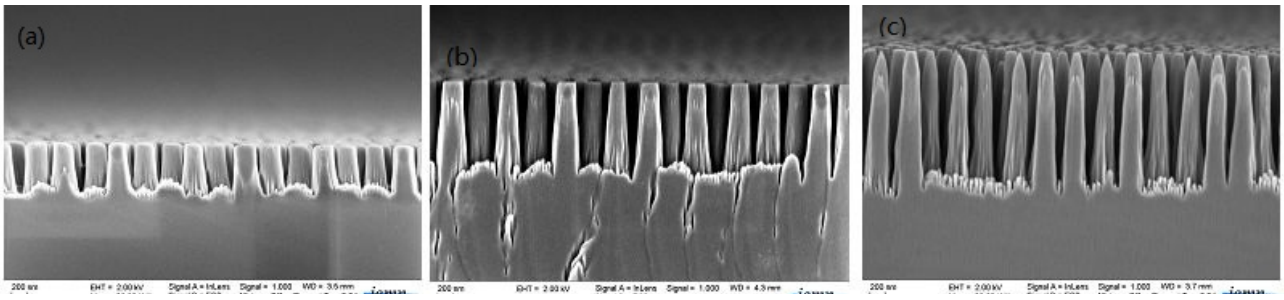

Figure 6 SEM images of SiNPs with diameter of 270 nm, period of 380 nm and length of (a) 800 nm, (b) 1300 nm and (c)1900 nm, respectively.

Samples	Diameters/nm	Period/nm	D/P	Length/nm
a	270	380	0.7	800
b	270	380	0.7	1300
c	270	380	0.7	1900

Table 3 Parameters of SiNPs corresponding to images a, b and c in fig.6.

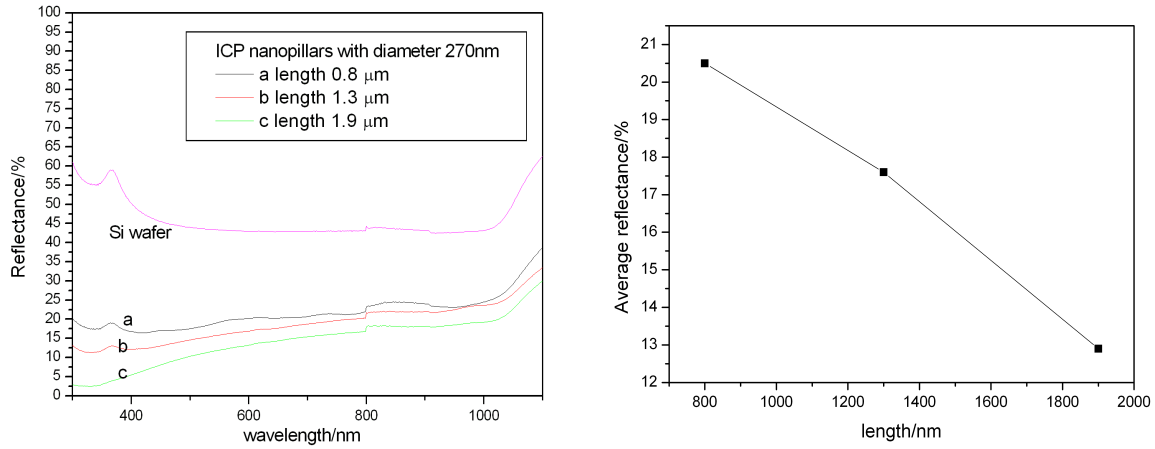

(a) (b)

Figure 7 (a)Total reflectance spectra for SiNPs with diameter of 270 nm, period of 380 nm and length of 800 nm, 1300 nm and 1900 nm, respectively. (b) Average reflectance as a function of length.

Sidewalls

As discussed in chapter 2, SiNPs etched by different methods have different sidewalls. In order to know the influence of sidewalls on the reflectance of SiNPs, we have fabricated two kinds of SiNPs with the same length of 1000 nm, same diameters of 600 nm and same period of 880 nm, by ICP etching and DRIE etching, respectively, as shown in fig.8. Table 4 shows the parameters of these SiNPs.

Fig.9 presents the corresponding reflectance spectra of SiNPs with different sidewalls in the wavelength range of 300 -1000 nm. Their average reflectances are comparable. This is because the size of this scallop profiles sidewalls is smaller than the measured wavelength, which is shown in fig.8(b). So the small sidewalls have no effect on the reflectance spectra.

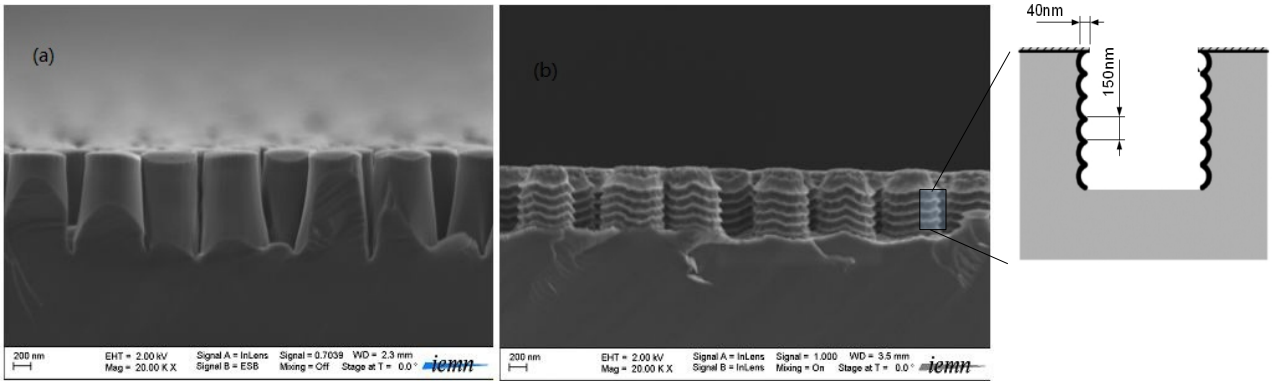

(a) (b)

Figure 8 SEM images of SiNPs with (a) smooth sidewalls and (b) scallop profiles sidewall, respectively.

Samples	Diameters/nm	Period/nm	D/P	Length/nm
a	600	880	0.68	1000
b	600	880	0.68	1000

Table 4 Parameters of SiNPs corresponding to images a and b in fig.8.

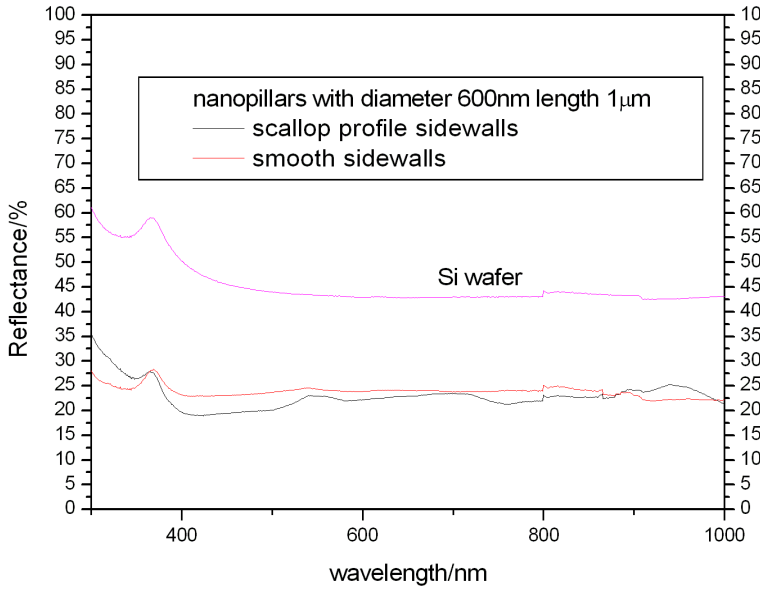

Figure 9 Total reflectance spectra for SiNPs with smooth sidewalls and scallop profiles sidewalls

Nanocones

As discussed before, SiNPs have excellent antireflection properties, and the reflectance are tunable by varying the diameter and length. Besides, NCs can also reduce the reflection by graded transition of effective refractive index from air to Si. [2]

Fig.10 shows the SEM image of SiNCs with different parameters, which were fabricated by changing the RIE etching time and etching gas. The corespondent parameters are given in table 5. Fig.11 shows the reflectance spectra of SiNCs. With the decrease of diameters, the reflectance decreases, while with the increase of length, the reflectance decreases. So for a given period of 880 nm, the best fabricated SiNCs is the one with top diameter of 400 nm,bottom diameter of 806 nm and the length of 470 nm.

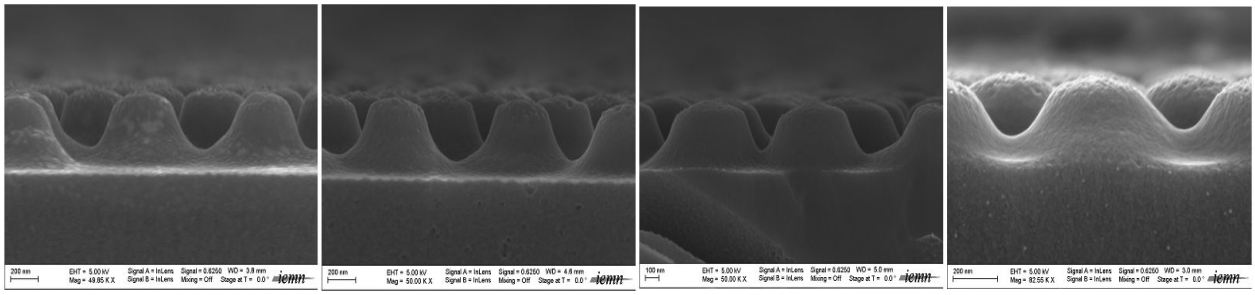

(a) (b) (c) (d)

Figure 10 SEM images of SiNCs with (a) length of 470 nm, bottom diameter of 806 nm, top diameter of 400 nm (b) length of 480 nm, bottom diameter of 880 nm, top diameter of 414 nm (c) length of 420 nm, bottom diameter of 837 nm, top diameter of 436 nm and (d) length of 340 nm, bottom diameter of 804 nm, top diameter of 375 nm, respectively.

Samples	Top diameters/nm	Period/nm	Bottom diameters/nm	D/P	Length/nm
a	400	880	806	0.6	470
b	414	880	880	0.8	480
c	436	880	837	0.6	420
d	375	880	804	0.7	340

Table 5 Parameters of SiNPs corresponding to images a, b,c and d in fig.10.

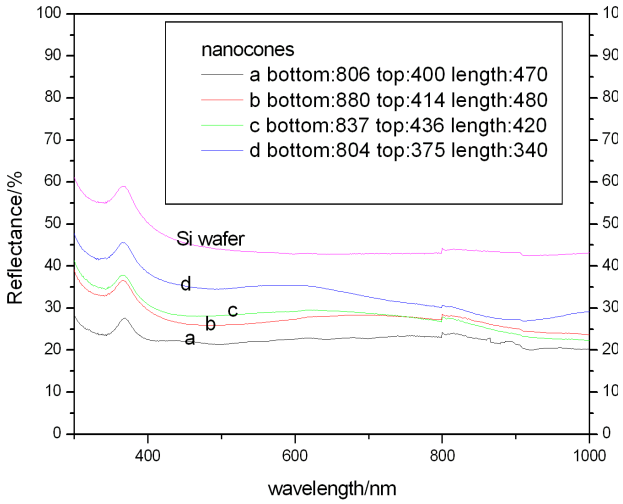

Figure 11 Total reflectance spectra for SiNCs

3.2 Influence of the structural parameters on the simulated optical properties

The experimental studies have been done in the previous section by comparing the reflectance spectra. Due to the limitation of fabrication technology and measurement system, it's impossible to study the absorption of SiNPs with too many different sizes. In order to better understand the behavior of SiNPs and SiNCs, we investigated the simulated optical properties of Si nanostrutures by the finite difference time domain (FDTD) method. In this method, the calculations are performed on periodic array of vertical NPs on Si substrate. The structure of the unit cell is shown in fig.12. The incident source is placed in the air medium and propagate along the z-direction. At each left and right sides of unit cell, perfectly matched layers (PML) were used to avoid the reflection wave which penetrate inside them. Periodic boundary conditions (PBC) are applied on both top and down sides of the unit cell to build the perodic structure. As shown in fig.12(b), these SiNPs repeated periodically, so the structure is infinite in the (x, y) plane. To study the absorption of SiNPs, a reflection detector is placed in the air medium and a transmission one is placed close to the interface between Si wafer and NPs in the Si medium.

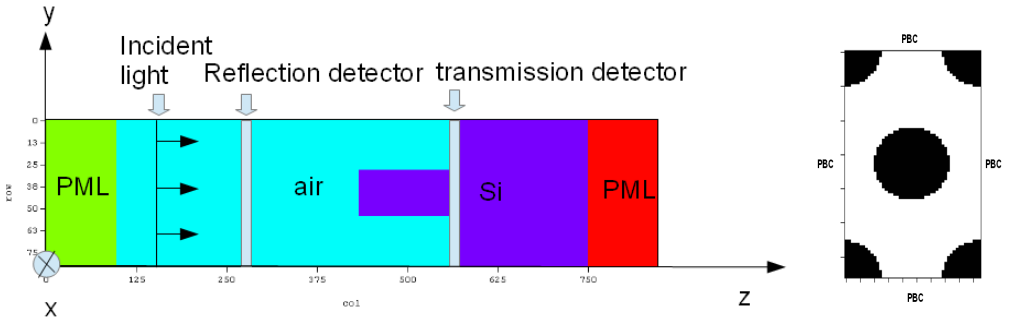

(a) (b)

Figure 12 Schematic representation of (a) Si NPs periodic array structure and (b) cross section of SiNPs array.

Principle of FDTD method

The FDTD method is performed considering the calculation in a 3D box both in tima and space, the cartesian coordinates of the electromagnetic wave:

$\vec{E} = \begin{Bmatrix} E_x \\ E_y \\ E_z \end{Bmatrix}$ for electrical field and $\vec{H} = \begin{Bmatrix} H_x \\ H_y \\ H_y \end{Bmatrix}$ for magnetic field

The optical properties of the unit cell are described through the Maxwell's equations:

$$\vec{\nabla}\times\vec{E}=\frac{-\partial\vec{B}}{\partial t} \quad (1)$$

$$\vec{\nabla}\times\vec{B}=\mu_0\varepsilon_0\varepsilon_r\frac{\partial\vec{E}}{\partial t} \quad (2)$$

taking an example of the first equations in the i direction gives:

$$\mu_0\frac{\partial H_x}{\partial t}=\frac{\partial E_y}{\partial z}-\frac{\partial E_z}{\partial y} \quad (3)$$

where $\varepsilon=\varepsilon_0\varepsilon_r$ and $\vec{B}=\mu_0\vec{H}$

It is impossible to obtain analytical resolution of those equations for the system studied. So we use a numerical method, the FDTD, which use finite central difference approximation in both time and space rather than partial differential equation.

In this method, a continuous function f(h) was used to represent one component of the electric or magnetic field, as shown in fig.13. Taylor series of this function are:

$$f\left(h_0+\frac{\Delta}{2}\right)=f\left(h_0\right)+\frac{\Delta}{2}f'(h)|_{h=h_0}+\frac{1}{2!}\left(\frac{\Delta}{2}\right)^2f''(h)|_{h=h_0}+\ldots \quad (4)$$

$$f\left(h_0-\frac{\Delta}{2}\right)=f\left(h_0\right)-\frac{\Delta}{2}f'(h)|_{h=h_0}+\frac{1}{2!}\left(\frac{\Delta}{2}\right)^2f''(h)|_{h=h_0}+\ldots \quad (5)$$

the first derivative of f(h) in h_0 is

(6)-(7) : $$\left.\frac{\partial f}{\partial h}\right|_{h=h_0}=\frac{f\left(h_0+\frac{\Delta}{2}\right)-f\left(h_0-\frac{\Delta}{2}\right)}{\Delta}+o\left(\Delta^2\right) \quad (6)$$ where $o(\Delta^2)$ is the error term

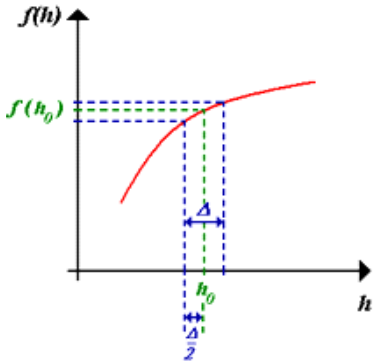

Figure 13 Principle of first derivative of f(h) in h_0

The FDTD method is based on two discretizations: a temporal one and a spatial one. The 3D space is discretized by a mesh with spatial increment Δx=Δy= Δz (in fig.14) and time is discretized by temporal increment Δt.

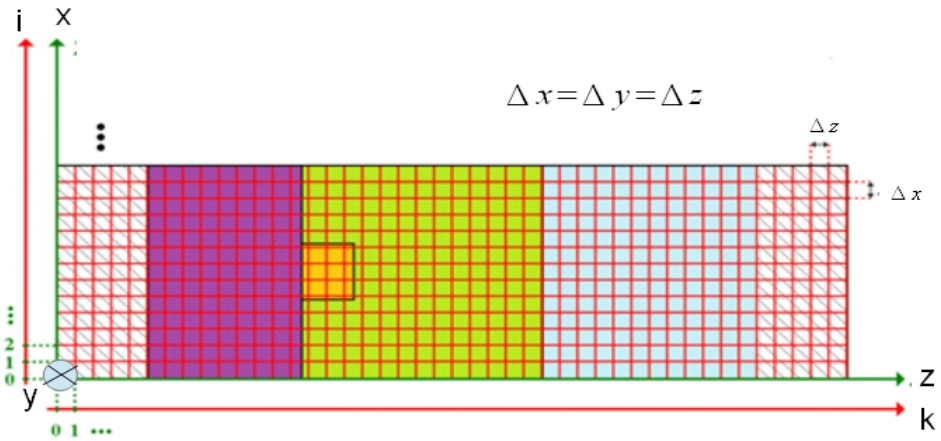

Figure 14 Spatial discretization of unit cell for FDTD application

The discretization of $\vec{E}$ and $\vec{H}$ is made on moved grids. K. Yee first proposed spatial staggering of the vector components of the E-field and H-field about rectangular unit cells of a cartesian grid. Each E field component is surrounded by four H field components, and each H field component is surrounded by four E field components, as shown in fig.15.

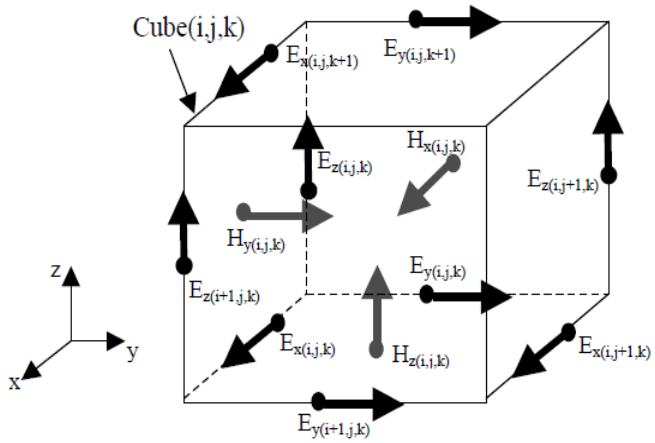

Figure 15 Representation of the position of the electromagnetic field components for Yee cell, located within the staggered cartesian grid.

The discretization in time is performed in a leap frog manner where the E-field and H-field updates are staggered, as shown in fig.16. The E-field (resp. H-field) updates are deduced midway during each time-step between successive H-field (resp. E-field) updates.

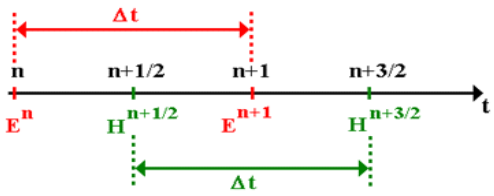

Figure 16 Representation of temporal discretization

After discretization, the partial differential equation (3) is changed :

$$H_x^{(n+\frac{3}{2})}(i,j,k)=H_x^{(n+\frac{1}{2})}(i,j,k)+\frac{\Delta t}{\mu}\left\{\frac{1}{\Delta z}[E_y^{n+1}(i,j,k)-E_y^{n+1}(i,j,k-1)]-\frac{1}{\Delta y}[E_z^{n+1}(i,j,k)-E_z^{n+1}(i,j-1,k)]\right\} \quad (7)$$

where $H_x^{(n+\frac{3}{2})}(i,j,k)$ represents the value of the magnetic field components along the x-axis, at the coordinates point $(x=i\Delta x, y=j\Delta y, z=k\Delta z)$ and at time $t=(n+\frac{3}{2})\Delta t$.

Equation (9) shows that at time $t=(n+\frac{3}{2})\Delta t$, the component H_y of the magnetic field is calculated from:

- component H_Z at the same coordinates point, but at time $t=(n+\frac{1}{2})\Delta t$

- the four nearest electrical field components at time $t=(n+1)\Delta t$

In total, there are six equations similar to equation (7), given as follows:

$$H_x^{(n+\frac{3}{2})}(i,j,k)=H_x^{(n+\frac{1}{2})}(i,j,k)+\frac{\Delta t}{\mu}\left\{\frac{1}{\Delta z}[E_y^{n+1}(i,j,k)-E_y^{n+1}(i,j,k-1)]-\frac{1}{\Delta y}[E_z^{n+1}(i,j,k)-E_z^{n+1}(i,j-1,k)]\right\}$$

$$H_y^{(n+\frac{3}{2})}(i,j,k)=H_y^{(n+\frac{1}{2})}(i,j,k)+\frac{\Delta t}{\mu}\left\{\frac{1}{\Delta x}[E_z^{n+1}(i,j,k)-E_z^{n+1}(i-1,j,k)]-\frac{1}{\Delta z}[E_x^{n+1}(i,j,k)-E_x^{n+1}(i,j,k-1)]\right\}$$

$$H_z^{(n+\frac{3}{2})}(i,j,k)=H_z^{(n+\frac{1}{2})}(i,j,k)+\frac{\Delta t}{\mu}\left\{\frac{1}{\Delta y}[E_x^{n+1}(i,j,k)-E_x^{n+1}(i,j-1,k)]-\frac{1}{\Delta x}[E_y^{n+1}(i,j,k)-E_y^{n+1}(i-1,j,k)]\right\}$$

$$E_x^{(n+1)}(i,j,k)=E_x^n(i,j,k)-\frac{\Delta t}{\varepsilon}\{\frac{1}{\Delta z}[H_y^{n+\frac{1}{2}}(i,j,k)-H_y^{n+\frac{1}{2}}(i,j,k-1)]-\frac{1}{\Delta y}[H_z^{n+\frac{1}{2}}(i,j,k)-H_z^{n+\frac{1}{2}}(i,j-1,k)]\}$$

$$E_y^{(n+1)}(i,j,k)=E_y^n(i,j,k)-\frac{\Delta t}{\varepsilon}\{\frac{1}{\Delta x}[H_z^{n+\frac{1}{2}}(i,j,k)-H_z^{n+\frac{1}{2}}(i-1,j,k)]-\frac{1}{\Delta z}[H_x^{n+\frac{1}{2}}(i,j,k)-H_x^{n+\frac{1}{2}}(i,j,k-1)]\}$$

$$E_z^{(n+1)}(i,j,k)=E_z^n(i,j,k)-\frac{\Delta t}{\varepsilon}\{\frac{1}{\Delta y}[H_x^{n+\frac{1}{2}}(i,j,k)-H_x^{n+\frac{1}{2}}(i,j-1,k)]-\frac{1}{\Delta x}[H_y^{n+\frac{1}{2}}(i,j,k)-H_y^{n+\frac{1}{2}}(i-1,j,k)]\}$$

The process is repeated many times as required until the last time-step is reached.

Dielectrical function of Si

In the FDTD method, the permittivity of dispersive materials cannot be directly subsituted into the FDTD scheme. Instead, the frequency-dependent complex permittivity

can be described by Lorentz mode of the form

$$\varepsilon(E)=\varepsilon_{\infty}+\sum_{p=1}^{4}\varepsilon_{p}(E) \qquad \varepsilon_{p}(E)=\frac{f_i\omega_{oi}^2}{\omega_{oi}^2-\omega^2+i\gamma_i\omega}$$

where $\varepsilon(E)$ is the dielectric permittivity, $\varepsilon(\infty)$ is high frequency dielectric constant, ω is the light energy (eV), f_i is the *i*th oscillator strength, ω_{0i} and γ_i are the transition energy and the dampling constant of the *i*th oscillator, respectively. We fit the permittivity by using Spectroscopic ellipsometry, which is a technique based on the measurement of a relative phase change of reflected and polarized light in order to characterize the thin film optical functions. A model has been made to evaluate the thickness and the optical properties of the materials by adjusting specific parameters in DeltaPsi2 software. This software fit the obtained permittivity automatically. The fitting parameters are shown in table 6.

i	f_j	γ_j	ω_{0j}	ε_∞
1	1.5511	0.2368	3.3997	2.6638
2	2.9212	0.6397	3.6895	
3	4.5495	0.6877	4.2073	

Table 6 Values of the parameters of the Lorentz oscillator model for bulk crystalline silicon

Fig.17 shows the experimental reflectivity measured by UV-visble spectroscopy (green dotted line) and simulated reflectivity using the measured fitting date (red dotted line) and the data from reference[9]. The Lorentz model data taken from literature were accurated only in the visible spectrum (black line in fig.17), while a peak was observed in the ultraviolet range. The simulated reflectivity using the fitting data is in excellent agreement with standard Si reference, weakly smaller than the experimental reflectivity measured by UV-vis spectroscopy. The difference originated from the mismatch between UV-visble spectroscopy and ellipsometry.

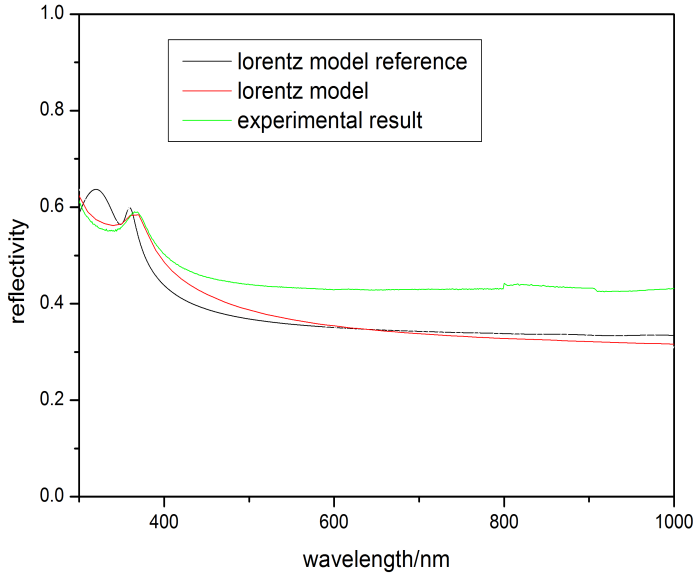

Figure 17 Experimental reflectivity measured by UV-visble spectroscopy (green dotted line) and simulated reflectivity using the measured fitting date (red dotted line) and the data from reference

Simulated results

Diameters

From the experimental results, it has been shown that the optical reflectance of SiNPs varies with their diameters. With the increase of diameter, the reflectance increases. We found that the best fabricated NPs with low reflectance, have the diameter of 270 nm.

In simulation, we put the reflection detector in air and transmission detector at the surface of Si bulk. The difference between the incident signal 'I' and the summation of the reflectance 'R' and the transmission 'T' at the surface corresponds to the part of energy 'A' absorbed through the NPs (NCs): A=I-(R+T). Fig.18(a) shows the simulated absorptivity spectra of NPs with various diameters ranging from 50 nm to 380 nm with a same length of 1000 nm and a period of 380 nm. Fig.18 (b) shows the threshold wavelength as a function of the diameters. The threshold wavelength is the wavelength corresponding to the half maximum intensity of absorption. With the increase of diameters, the threshold wavelength redshift occurs. It can be seen that when the diameter is smaller than 270 nm, the threshold wavelength is linearly proportional to the diameter. In previous work, the tendency are similar, when the threshold wavelength is studied as a function of diameter. [5]

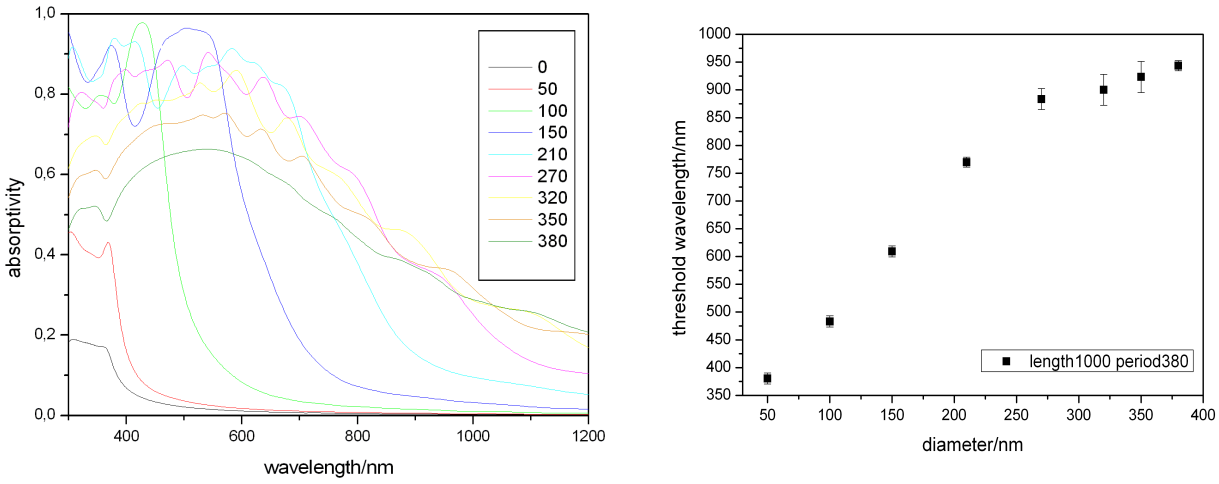

(a) (b)

Figure 18 (a) Absorptivity spectra of NPs for diameters ranging from 50 nm to 380 nm, with a same length of 1000 nm and period of 380 nm. (b) Evolution of the threshold wavelength as a function of diameter

In order to correlate the intensity of absorption with the distribution map of electromagnetic field intensity in NPs arrays, we calculate the electromagnetic field intensity for NPs with diameter of 150 nm, the period of 380 nm and the length of 1000 nm at the illumination wavelength of 509 nm and 1200 nm, respectively. As shown in fig.19(a), when we take the incident light with the wavelength of 509 nm, which corresponds to the maximum absorptivity, the electromagnetic field is focus on the top of the NPs. When the wavelength is 1200 nm, which corresponds to the minimal absorption, there is no electromagnetic field localized inside the pillars, in agreement with its minimal absorption.

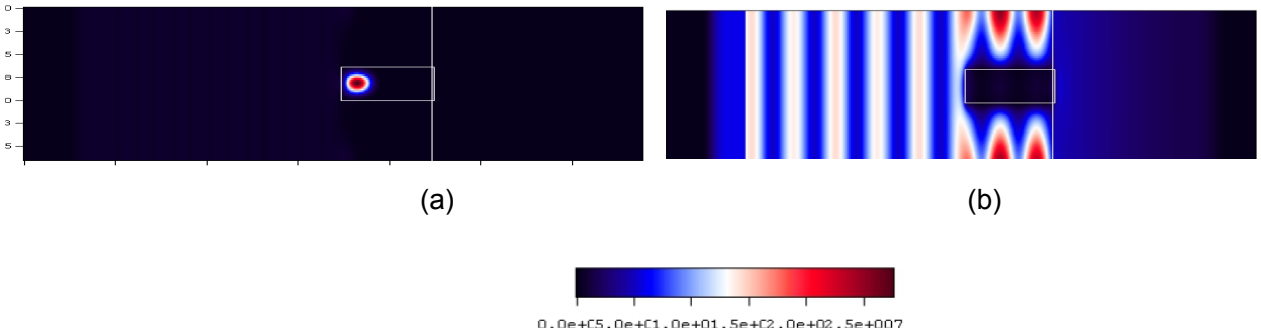

(a) (b)

Figure 19 Distribution map of electromagentic filed intensity for NPs with diameter of 150 nm, period of 380 nm and length of 1000 nm, (a) the illumination wavelength is 509 nm, which corresponds to the maximum absorption of this NPs (b) the illumination wavelength is 1200 nm,which corresponds to the minimum absorption of this NPs

In order to evaluate the absorption performance, we calculated the ultimate efficiency from $\eta = \frac{\int_0^{\lambda_g} I(\lambda) A(\lambda) \frac{\lambda}{\lambda_g} d\lambda}{\int_0^{\infty} I(\lambda) d\lambda}$ where, λ_g is the wavelength corresponding to the bandgap energy, I(λ) is the solar irradiance spectrum, taken to be the AM1.5G spectrum (see chapter 2) and A(λ) is the absorption. The ultimate efficiency describes the photocurrent when each absorbed photon produces one pair of electron-hole.These carriers are collected without taking into account the recombination.

Fig.20 shows the ultimate efficiency of NPs as a funtion of diameters.The red line corresponds to the efficiency of the Si wafer with same thickness. The results show that an optimum diameter exists for the NPs, with a maximum efficiency of 30 %, for a given period and length. This optimized diameter is 270 nm (D/P=0.7), which is in agreement with the experimental results. It appears from fig.20 that NPs with diameter smaller than 210 nm can not achieve higher absorption than the wafer with same thickness, so the critical diameter is 210 nm (D/P=0.55). In order to increase the solar cell harvesting, the NPs should have a diameter bigger than that critical diameter.

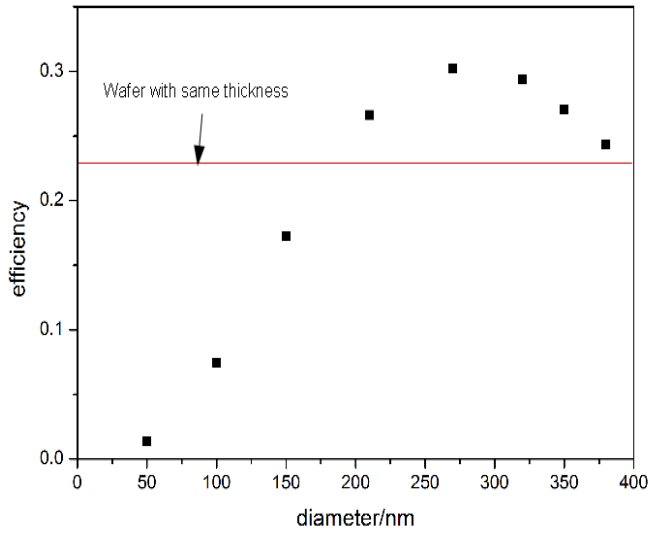

Figure 20 Theoretical ultimate efficiency of NPs with diameters ranging from 50 nm to 380 nm, the same length of 1000 nm and periods of 380 nm, red line shows the ultimate efficiency of Si wafer with same thickness

Period

As shown in many references[4.10-11], the absorption is also senstive to the period. When diameter versus period is larger than 0.5 (D/P>0.5), the light absorption is enhanced compared to the wafer with same thickness. To confirm this results, we studied the absorption of NPs with critical diameter of 210 nm, length of 1000 nm and different periods of 210 nm, 260 nm, 310 nm, 380 nm, 430 nm, 480 nm, 580 nm and 880 nm, respectively. Fig.21(a) shows the absorptivity spectra of these NPs. Fig.21(b) shows the threshold wavelength as a function of the period. The decrease of periods would shift the threshold wavelength towards higher wavelength, facilitating the absorption in a large spectrum. As shown in fig.21(c), the efficiency is significantly enhanced compared to the wafer with same thickness of 1000 nm, when the period is smaller than 430 nm (D/P=0.5). So the critical period is 430 nm. To increase the efficiency, the NPs should have a period smaller than that critical period. It is observed that the optimized period is 260 nm (D/P=0.8), because the NPs with this period has the maximum efficiency of 33 %, for a given diameter of 210 nm and length of 1000 nm.

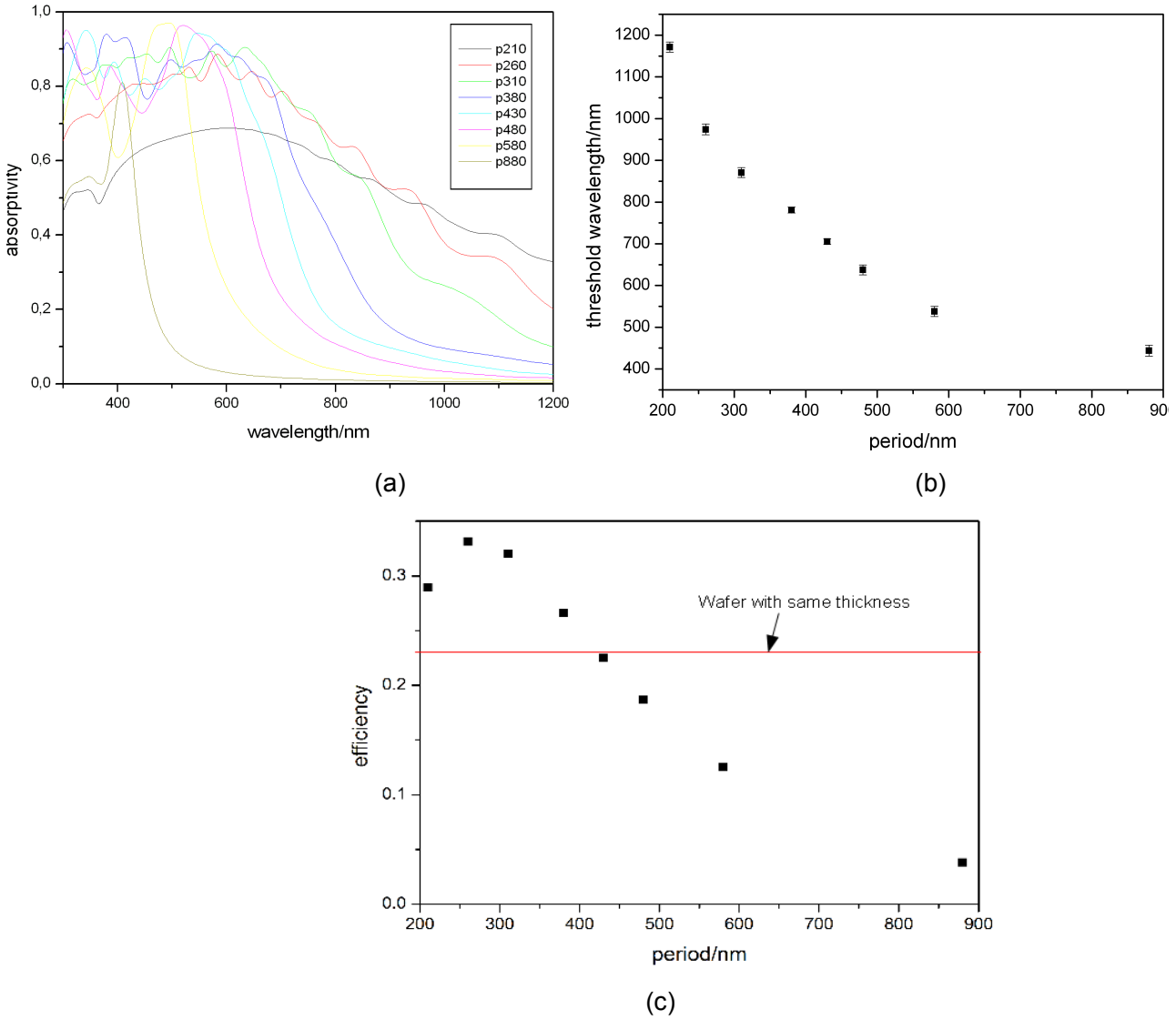

Figure 21 (a) Absorptivity spectra of NPs with various periods from 210 nm to 880 nm, the same length of 1000 nm and diameters of 210 nm. (b) Threshold wavelength as a function of period . (c)Ultimate efficiency as a function of periods

Length

As discussed in the experimental results, the longer the NPs is, the lower the reflectance is. So the best fabricated NPs have a length of 1900 nm. In order to understand the properties of NPs, we calculated the absorption of NPs with optimized diameter of 270 nm, period of 380 nm (D/P=0.7) and various lengths from 20 nm to 3000 nm. Fig.22 (a) shows the absorptivity spectra of NPs with different length. Fig.22 (b)shows the ultimate effficiency of these NPs. It can be seen that the increase of length will lead to

the increase of efficiency, so the longer the NPs, the better the efficiency, which is also in agreement with experimental results. This tendency is due to both the increasing volume of Si and the structural effect.

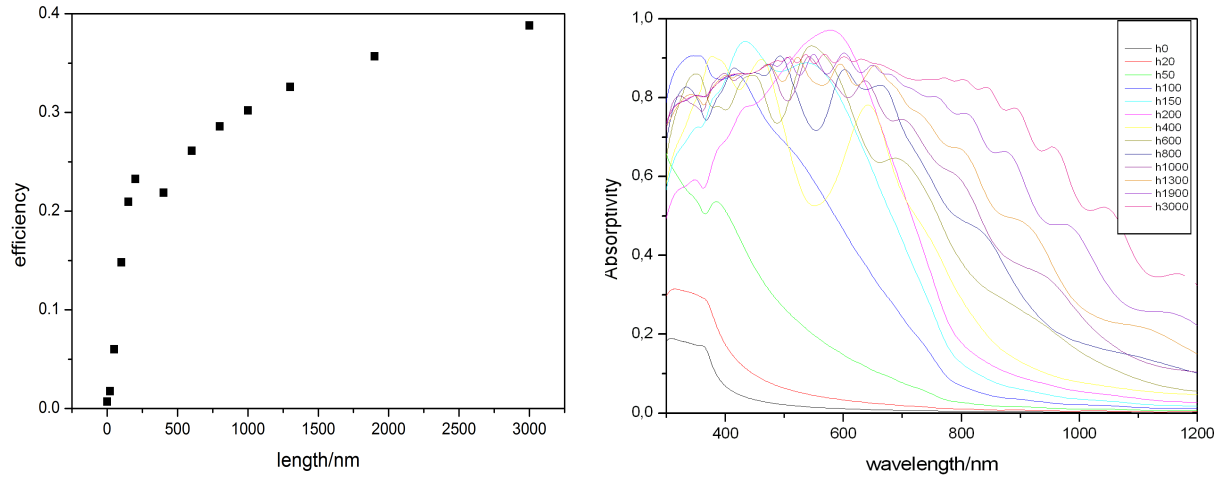

(a) (b)

Figure 22 (a) Absorptivity spectra of NPs with different length from 20 nm to 3000 nm, the same diameter of 270 nm and periods of 380 nm. (b)Ultimate efficiency as a function of length

In order to distinguish the origin of this enhancement, we compared the efficiency of NPs to that of wafer with equivalent volume, as represented in fig.23(a). Compared to wafer with same volume, the efficiency of NPs is always higher. We calculated the ratio of $\eta_{NPs}/\ \eta_{wafer}$, as shown in fig.23(b), which represents the gain of NP structural effect. Increasing the length will lead to an increase of the structural effect, when the length of NPs is up to 200 nm, the structural effect is maximum. After, the structural effect decreases with the increase of length and tend to be a constant. So when the length is longer than 400 nm, the efficiency enhancement with the variation of length is mainly due to the increase of Si volume.

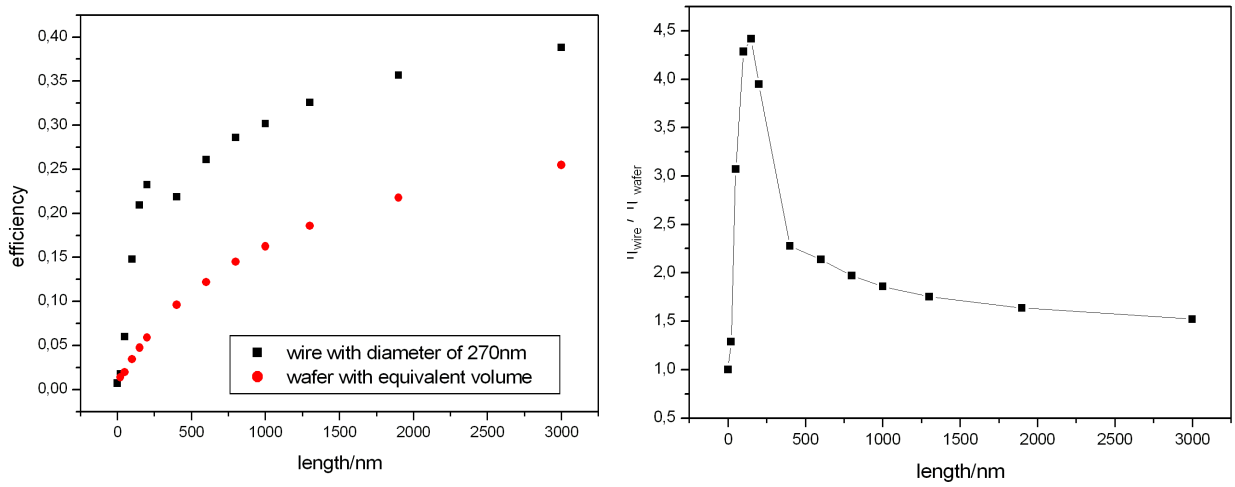

(a) (b)

Figure 23 (a) Efficiency of NPs with different length from 20 nm to 3000 nm, the same diameter of 270 nm and periods of 380 nm and efficiency of Si wafer with equivalent volume. (b) Ratio of NPs efficiency and efficiency of wafer with equivalent volume as a funtion of NP length

Efficiency as a function of diameter, period and length

The influence of diameter, period and length on the optical properties have been studied individually. But the efficiency is a function of these multiple factors. So in order to deeply understand the influence of these multiple factors, we have performed multiple parameters simulations, as shown in fig.24. Part A in the figure shows that for a given period of 380 nm, the optimized diameter is 270 nm (D/P=0.7), which is independent of the length of NPs. Of course, the efficiency of NPs with optimized diameters increases when the length of NPs increases.

We did the same calculation for a period of 600 nm (part B) and 900 nm (part C). For a given period of 600 nm (resp. 900 nm), the optimized diameter is 480 nm (resp.720 nm). In all investigated curves, the ratio D/P= 0.8.

To summarize, the optimized diameters depend on the period of NPs with the ratio D/P=0.7-0.8. This ratio is independent of the length of the SiNPs.

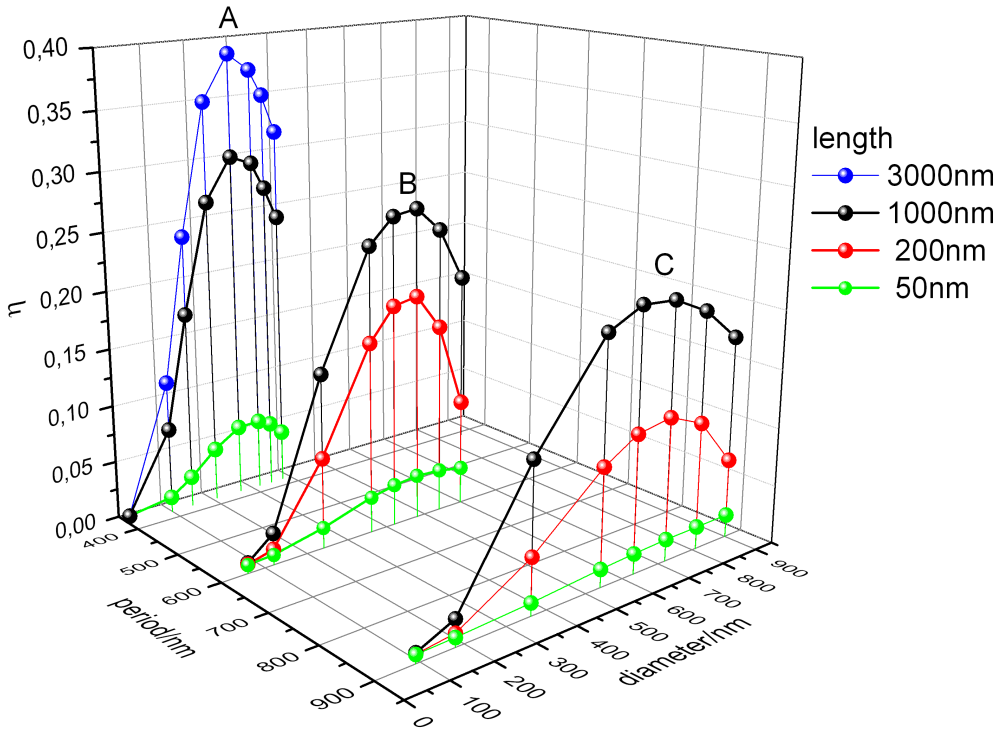

Figure 24 Efficiency of the NPs as a function of length, diameters and period

Same D/P

As discussed before, when D/P =0.7-0.8, the efficiency is maximum for a given length. Another question is to know whether it is more efficient to cover the Si surface with bigger (see fig.25 (a))or smaller SiNPs (see fig.25 (b)) with the ratio D/P=0.7. To answer this question, we compared the absorptivity spectra and efficiency of NPs with same D/P=0.7. Table 7 gives the parameters of these NPs. They have the diameters of 68 nm (with period of 95 nm), 135 nm (with period of 190 nm), 270 nm (with period of 380 nm), 540 nm (with period of 760 nm) and 1080 nm (with period of 1520 nm), respectively. As shown in fig.26, with the increase of diameters, the absorption edge shift toward the lower wavelength, and the efficiency decreases. When the diameter and period are bigger (D=1080 nm and P=1520 nm), the efficiency of NPs is close to that of Si bulk with same thickness.

So the efficiency of NPs with the same ratio D/P is not constant. The efficiency depends on the diameter and period of NPs. If the diameter and period of NPs are smaller (fig.25 (b)), the efficiency is higher.

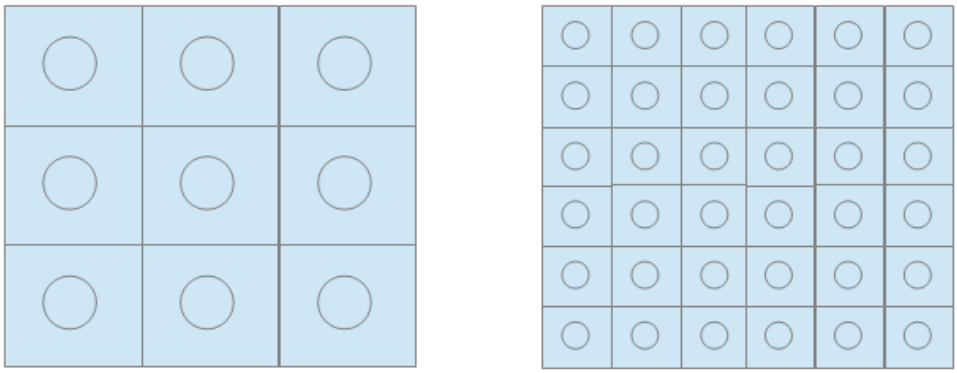

(a) (b)

Figure 25 Schema of (a) bigger SiNPs and (b) smaller SiNPs with same D/P

samples	Diameter/nm	Period/nm	D/P	Length/nm
a	68	95	0.7	1000
b	135	190	0.7	1000
c	270	380	0.7	1000
d	540	760	0.7	1000
e	1080	1520	0.7	1000

Table 7 Parameters of SiNPs with same D/P=0.7

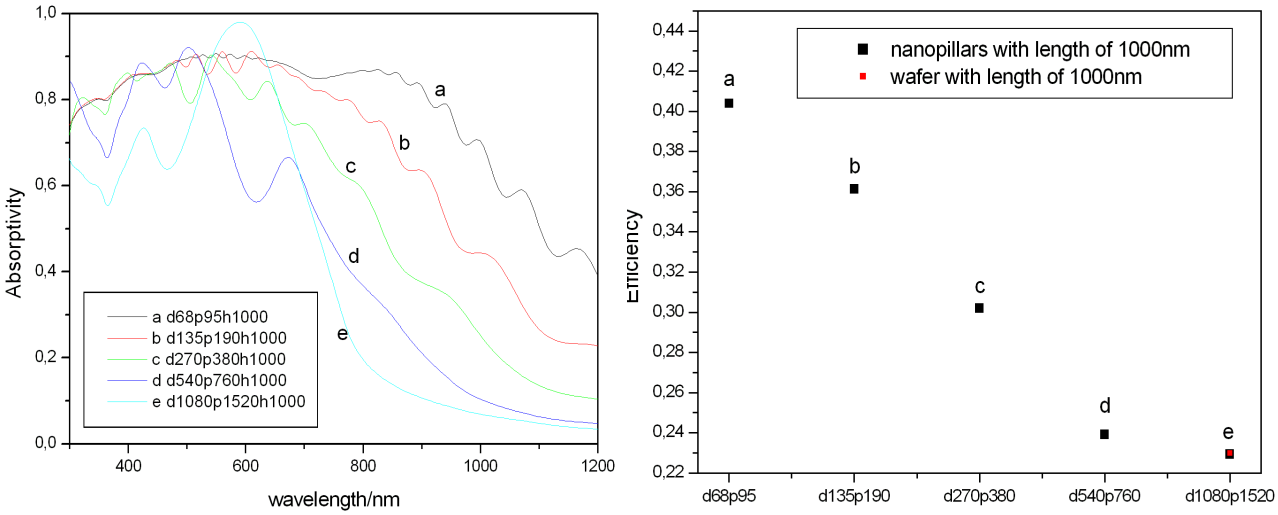

(a) (b)

Figure 26 (a) Absorptivity spectra of NPs with same D/P=0.7, different diameters of 68 nm, 135 nm, 270 nm, 540 nm and 1080 nm. (b) Ultimate efficiency of these NPs

Nanocones

Nanopillars are special instances of nanocones, where the top diameter is equal to the bottom diameter. The influence of bottom diameter, period and length on the optical properties of nanopillars can be extrapolated to nanocones. When fixing the bottom diameter and height, rotating the lateral sides by the angle θ, we obtain nanocones with different shapes, as shown in fig.27. In this part, we studied the influence of angle θ on the absorption of NCs.

Figure 27 Schematic view of NCs with same diameter of 704 nm for a given period of 880 nm and length of 350 nm. θ is the angle between lateral sides and bottom.

Fig.28 (a) shows the absorptivity spectra and efficiency of NCs with different angles θ. When θ increased from 50° to 90°, the absorption edge moved to the longer wavelength. The evolution of the efficiency as a function of θ (figure 28(b)) shows that NCs with angle of 80° and 85° exhibited a maximum of efficiency.

Because the effective refractive index changes gradually from the root to the top of NCs, the Ncs demonstrated excellent antireflection properties over a broad range of wavelengths. It has been demonstrated that compared the absorption of NCs and NPs with same thickness, both the experimental and caclulated results show the NCs exhibited enhanced absorption[2,5].

So from an experimental point of view, in order to reach higher absorption, it's better to make NCs with bigger angle θ (from 80° to 90°), for given period, bottom diameters and height.

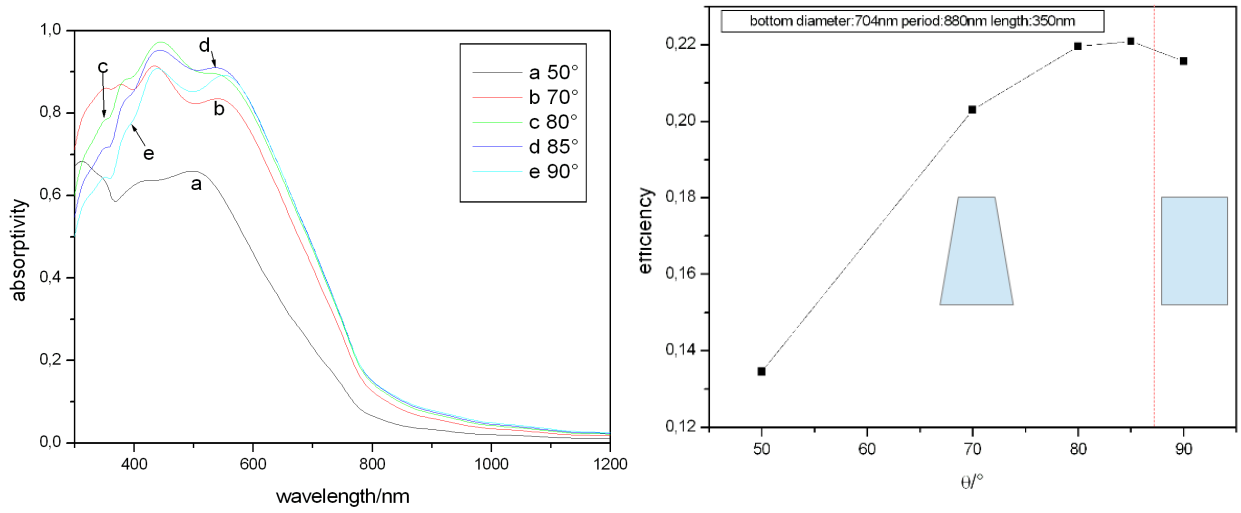

(a) (b)

Figure 28 (a) Absorptivity spectra of NCs with the same height,same period,same bottom diameter but different angle θ. (b)Ultimate efficiency of these NCs

3.3 Comparison between experimental and simulated results

In this section, we simulate the reflectance of samples we made, and compare them to the experimental results.

Nanopillars

First, we simulated the reflectance of SiNPs, samples of same length and period with different diameters as reported in table 1 with same length of 750 nm, same period of 380 nm and different diameters of 320 nm and 270 nm, the SEM images of NPs are shown in fig.1. Fig.29 gives the simulated reflectance spectra of these SiNPs. It can be observed that the simulated reflectance spectra exhibit a great oscillation while the experimental reflectance spectra are smooth (see fig.2). This discrepancy can be due to the size dispersity of the NPs. While experimentally, the size of the NPs is not uniform, the simulations have been done with uniform NPs with an average value of the experimental sizes. The experimental reflectance spectra is the results of interfence between the reflectance spectra of NPs with different diameters. The experimental reflectance spectra appear smoothly compared to theoretical spectra.

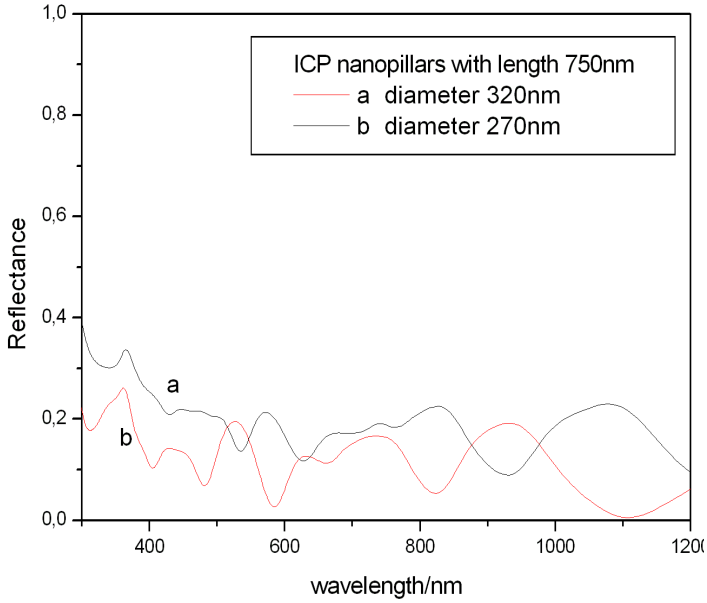

Figure 29 Simulated reflectance spectra of NPs with same length of 750 nm, same period of 380 nm and different diameters of 320 nm and 270 nm

To overcome this difficulty, we have calculated the average reflectances for experimental results and have compared them to the simulated ones, as shown in fig.30. The experimental and theoretical average reflectance values are not the same, while the behavior is almost the same. This difference originates from the error of UV-VIS spectroscopy. The measured reflectance for standard Si reference is larger than the simulated results (see fig.17). In spite of this difference, the simulated average reflectance as a function of diameters is the same as experimental one. With the increase of diameters, the average reflectance first decrease and then increase. The simulated results shows that the best NPs have a diameter of 270 nm with D/P=0.7, in agreement with experimental results.

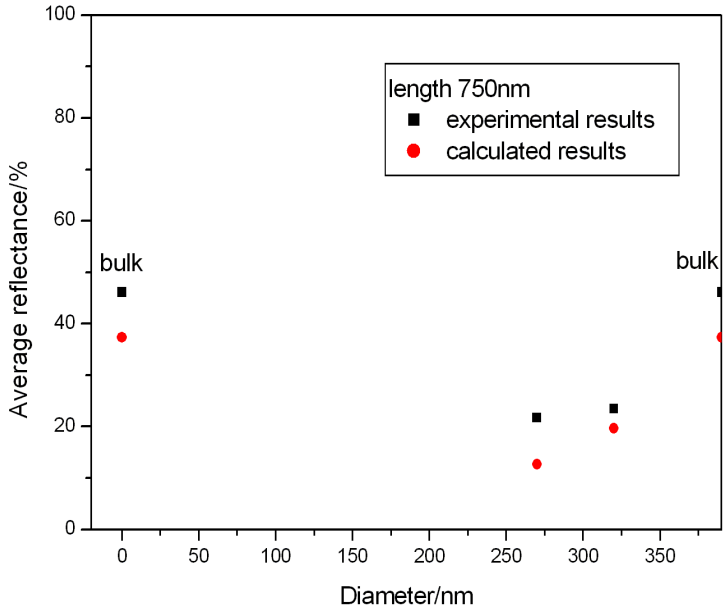

Figure 30 Experimental (black squares) and theoretical (red squares) average reflectance as a function of diameters. NPs have the same length of 750 nm, same period of 380 nm and different diameters of 320 nm and 270 nm

Secondly, we simulate the reflectance spectra of NPs with same length of 1300 nm and different D/P of 0.6, 0.7 and 0.8 (see fig. 3 and table 2). Fig.31 gives a comparison of the average reflectance between experimental results and simulated results. The calculated results are always smaller than the experimental results a few percent, but the average reflectance behavior as a function of D/P is quite similar. It can be seen that the NPs with D/P =0.6 show the lower reflectance, and when we compare the reflectance of NPs with D/P=0.6, the NPs with smaller period of 380 nm and smaller diameters of 240 nm have the lowest reflectance. So the best NPs have the D/P=0.6, diameters of 240 nm and period of 380 nm, which agrees with the experimental results.

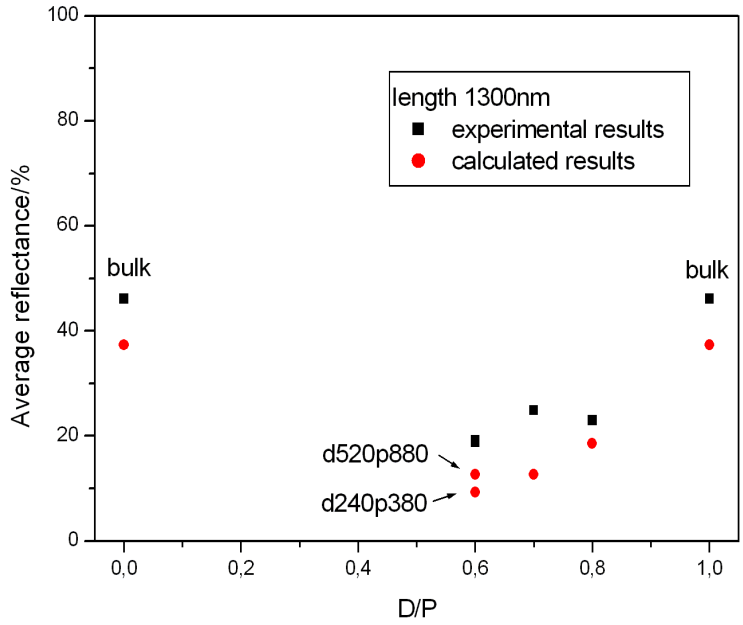

Figure 31 Experimental (black squares) and theoretical (red squares) average reflectance as a function of D/P. NPs have the same length of 1300 nm, and different D/P.

Thirdly, we simulated the reflectance of SiNPs with different lengths of 800 nm, 1000 nm and 1300 nm (see fig.6 and table 3). Fig.32 gives the average reflectance of simulated results, compared with experimental results. It can be seen that the reflectance is not sensitive to the length, when the length is longer than 800 nm. The average reflectance as a function of length is a constant. This is not in agreement with experimental results. As shown in fig.6, we can notice that the fabricated NPs with length of 1900 nm have tapered tips. It has been investigated that NCs with the tapered tip have an enhanced antireflection properties.[7] The effect of conical shape on the reflectance spectra has to be taken into consideration in the theoretical calculation. We expect that a conical shape, associated with the largest length, will decrease the reflectance. (optical adaptation effect)

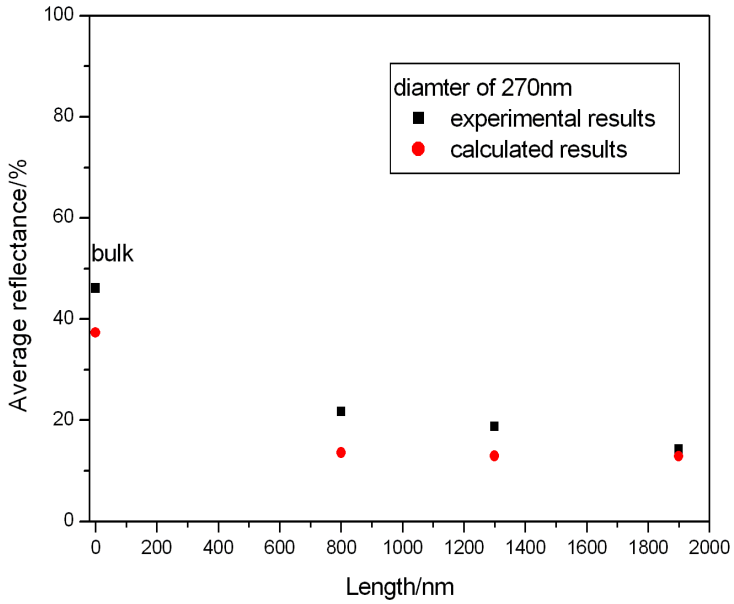

Figure 32 Experimental (black squares) and theoretical (red squares) average reflectance as a function of length. NPs have the same diameters of 270 nm, and same period of 380 nm

Conclusion

In summary, we have studied the influence of diameter, period and length of NPs and NCs on the experimental and calculated optical properties for photovoltaic application. In order to achieve superior ultimate efficiency than Si wafer with same thickness, the ratio of D/P should be between 0.5 and 1, the period as small as possible and the conical angle θ between 80° and 90°.

(a) The optimized diameter changes with the variation of period. When D/P=0.7-0.8, the NPs shows the highest efficiency, and this ratio is independent of the length.

(b) For a given ratio D/P, NPs with smaller diameters and periods exhibited higher efficiency.

(c) The longer the length, the higher the efficiency. This enhancement is due to both the increasing Si volume and the surface structural effect. When the length is up to 400 nm, the gain of structural effect is constant, so the enhancement is consequently due to the increase of Si volume

(d) When the size of the sidewalls is smaller than the measured wavelength, the sidewalls have no effect on the reflectance spectra of NPs.

(e) If the bottom diameter, period and height are constant, NCs with bigger angle θ exhibit higher efficiency.

[1] E. T. Yu and J. V. Lagemaat. Photon management for photovoltaics. MRS Bulletin. 36, 424 (2011).

[2] J. Zhu, Z. f. Yu *et al*. Optical Absorption Enhancement in amorphous silicon nanowire and nanocone arrays. Nano Letters. 9, 279 (2009).

[3] H. Alaeian, A. C. Atre *et al*. Optimized light absorption in Si wire array solar cells. Journal of Optics. 14, 024006 (2012).

[4] J. S. Li, H. Y.Yu *et al*. Design guidelines of periodic Si nanowire arrays for solar cell. Applied Physics Letters. 95, 243113 (2009).

[5] T. Xu, Y. Lambert *et al*. Optical absorption of silicon nanowires. Journal of Applied Physics. 112, 033506 (2012).

[6] B. M. Wang and P. W. Leu. Enhanced absorption in silicon nanocones arrays for photovoltaics. Nanotechnology. 23,194003 (2012).

[7] W. Q. Xie, J. I. Oh and W. Z. Shen. Realization of effective light trapping and omnidirectional antireflection in smooth surface silicon nanowire arrays. Nanotechnology. 22, 065704 (2011).

[8] C. M. Hsu, S. T. Connor *et al*. Wafer-scale silicon nanopillars and nanocones by Langmuir–Blodgett assembly and etching. Applied Physics Letters. 93, 133109 (2008).

[9] L. Ding, T. P. Chen *et al*. Optical properties of silicon nanocrystals embedded in a SiO2 matrix. Physical Review B. 72, 125419 (2005).

[10] C. X. Lin and M. L. Povinelli. Optical absorption enhancement in silicon nanowire arrays with a large lattice constant for photovoltaic applications. Optics Express. 17, 19371 (2009).

[11] J. S. Li, H. Y. Yu *et al*. Si nanopillar array optimization on Si thin films for solar energy harvesting. Applied Physics Letters. 95, 033102 (2009).

Chapter 4 Al-doped ZnO transparent conductive oxide

4.1 Introduction

Transparent and conductive oxides (TCOs) are required to improve solar cell efficiency. To be a good TCOs, these materials must exhibit simultaneously high electrical conductivity and high visible wavelength transparency. They are usually prepared with thin film technologies and used in opto-electrical devices such as flat panel displays, thin film transistors, light emitting diodes and light absorbing devices (solar cells).[1-3]

The most common TCO used in such applications is doped Indium Tin Oxide (ITO). Indeed, it has been widely used as transparent electrodes in solar cells, because it is transparent to visible light, and by virtue of its refractive index, it forms an antireflecting coating on silicon which can overcome these losses.

However, due to the cost and the scarcity of indium, some alternatives are being searched.[4] Because ITO exhibits a resistivity of the order of 10^{-3} Ωcm and an average transmittance above 80% in the visible range, the alternatives should have a carrier concentration of the order of 10^{20} cm^{-3} and a band gap energy above approximately 3 eV.

Table 1 shows the TCO (transparent conducting oxide) semiconductors for thin-film transparent electrodes which have been developed up to now. Among these semiconductors, Al-doped Zinc oxide (AZO) is a common choice because Al and Zn are common and inexpensive materials and they have lowest resistivities comparable to other ZnO films doped with other impurities, as shown in table 2.[1]

Table 1. TCO semiconductors for thin-film transparent electrodes.

Material	Dopant or compound
SnO_2	Sb, F, As, Nb, Ta
In_2O_3	Sn, Ge, Mo, F, Ti, Zr, Hf, Nb, Ta, W, Te
ZnO	Al, Ga, B, In, Y, Sc, F, V, Si, Ge, Ti, Zr, Hf
CdO	In, Sn
$ZnO–SnO_2$	Zn_2SnO_4, $ZnSnO_3$
$ZnO–In_2O_3$	$Zn_2In_2O_5$, $Zn_3In_2O_6$
$In_2O_3–SnO_2$	$In_4Sn_3O_{12}$
$CdO–SnO_2$	Cd_2SnO_4, $CdSnO_3$
$CdO–In_2O_3$	$CdIn_2O_4$
$MgIn_2O_4$	
$GaInO_3$, $(Ga, In)_2O_3$	Sn, Ge
$CdSb_2O_6$	Y
$ZnO–In_2O_3–SnO_2$	$Zn_2In_2O_5–In_4Sn_3O_{12}$
$CdO–In_2O_3–SnO_2$	$CdIn_2O_4–Cd_2SnO_4$
$ZnO–CdO–In_2O_3–SnO_2$	

Table 1 TCO semiconductors for thin-film transparent electrodes and prepared by pulsed laser deposition [1]

Dopant	Dopant content (wt%)	Resistivity × 10^{-4} (Ω cm)	Carrier concentration × 10^{20} (cm^{-3})
Al_2O_3	1–2	0.85	15.0
Ga_2O_3	2–7	1.2	14.5
B_2O_3	2	2.0	5.4
Sc_2O_3	2	3.1	6.7
SiO_2	6	4.8	8.8
V_2O_5	0.5–3	5.0	4.9
F	0.5 (at%)	4.0	5.0
None	0	4.5	2.0

Table 2 Resistivity, dopant content and carrier concentration for typical ZnO films doped with various impuritiesand prepared by pulsed laser deposition. [1]

More than 1500 publications have been edited on AZO materials. In this chapter, we will just give a very brief review about the most important parameters used to elaborate AZO thin films and we will begin with the synthesis method.

A lot of methods have been used for AZO film synthesis, including molecular beam epitaxy (MBE), pulsed laser deposition (PLD), atomic layer deposition (ALD), chemical vapor deposition (CVD), sputtering, cathodic magnetron sputtering, spray pyrolysis and sol-gel methods[5]. Table 3 lists the drawbacks and advantages of these methods. MBE, PLD, ALD and CVD methods are quite expensive. Spray pyrolysis method is a low-cost method but it will lead to environment pollution. Sputtering technology is one of the most widely used technologies to prepare AZO films with lower resistivity of the order of 10^{-4} Ωcm. However, during this process, the non-uniformity of the magnetic field results in a non-uniformity of resistivity. Additionally, AZO films deposited by this method cannot cover nanostructures with high aspect ratios (length-to-width ratio) and it's not easy to do low temperature sputtering. Sol-gel methods allow to prepare uniform coatings in ambient conditions at low equipment cost, their properties of films are tunable and films can fully cover nanostructures with high aspect ratios by spin coating, so we use this method in this work.

Different methods	advantage	disadvantage
magnetron sputtering	Used on different shapes of substract or large area substract high speed to form films and film with good adhesion	Not easy to do low temperature sputtering, non-uniformity of resistivity can not fully cover nanostructures with high aspect ratios
PLD	Easy to control the stoichiometry, low roughness of film and sample is hard to be polluted	High cost of equipment
MBE	Easy to control the stoichiometry and make high concentration doping	High cost of equipment and low growing rate
ALD	Extremely precise processing and uniform deposition of thin film	low growth rate at the vertical direction
CVD	High productivity, obtain uniform film, good adhesive film	The lackage and high-cost of the precusor
spray pyrolysis	Low cost	Environment pollution
sol-gel process	Easy to control the stoichiometry, low-cost and uniform films	Chemical and physical parameters

Table 3 Comparison of different technologies [6-8]

During sol-gel process, several parameters can affect the properties of AZO films, which have been studied by many researchers (more than 200 publications). Table 4 gives some examples of the parameters of sol-gel derived Al-doped ZnO films previously reported in some publications. Starting materials, solvent, coating method, doping concentration and heat treatment will significantly vary the resistivity. But the variation of resistivity as a function of one operating parameter is still a very complicated problem. If the starting materials are zinc acetate dihydrate ($Zn(CH_3COO)_2 \cdot 2H_2O$) and aluminium nitrate nonahydrate ($Al(NO_3)_3 9H_2O$), the solvent and additive are 2-Methoxyethanol and monoethanolamine (MEA), the lowest resistivities of AZO thin films deposited by spin-coating are different. For example, Ref [10] gives the lowest resistivity of 2.57 Ωcm, corresponding to the AZO films with Al doping concentration of 2 wt.%, baking temperature of 150 °C and post-annealing temperature of 500 °C, while Ref [15] shows the lowest resistivity of 6.2×10^{-4} Ωcm and the corresponding AZO films have the Al doping concentration of 1.5 wt.%, baking temperature of 400 °C and post-annealing temperature of 530 °C. When choosing $AlCl_3 6H_2O$ instead of $Al(NO_3)_3 9H_2O$ and depositing thin films by dip-coating, the obtained lowest resistivities are also different. In order to obtain AZO film with high transparency and conductivity used in our solar cells, it's necessary to optimize

these parameters.

Starting materials	solvent	coating	transparency	Lowest resistivity	Corresponding parameters
$Zn(CH_3COO)_2 2H_2O$ $AlCl_3 6H_2O$ [9]	2-Methoxyethanol MEA	dip-coating	transparent	$1,3X10^{-3}$ Ωcm	2 wt.% Al preheated at 400 °C + post-heated at 600°C + annealing under a reduced atmosphere
$Zn(CH_3COO)_2 2H_2O$ $Al(NO_3)_3 9H_2O$[10]	2-methoxyethanol MEA	spin-coating	transparent	2.57Ωcm	2 wt.% Al, preheated at 150 °C + post-heated at 500°C
$Zn(CH_3COO)_2 2H_2O$ $AlCl_3 6H_2O$[11]	2-methoxyethanol MEA	dip-coating	transparent	$2.9x10^{-3}$ Ωcm	2 wt.% Al, preheated at 400 °C + post-heated at 600°C
$Zn(CH_3COO)_2 2H_2O$ $AlCl_3 6H_2O$[12]	2-methoxyethanol MEA	dip-coating	transparent	$6.5x10^{-3}$ Ωcm	0,5 wt.% Al, preheated at 400 °C + post-heated at 600°C+ post-heated at 600°C in nitrogen
$Zn(CH_3COO)_2 2H_2O$ [13]	2-methoxyethanol MEA	spin-coating	transparent	0.099 Ωcm	preheated at 350 °C + post-heated at 600°C in air + post annealing at 500°C in forming gas
$Zn(CH_3COO)_2 2H_2O$ [14]	dehydrated isopropyl alcohol DEA	Drain coating	transparent	0,225 Ωcm	preheated at 120 °C + post-heated at 550°C in vacuum
$Zn(CH_3COO)_2 2H_2O$ $Al(NO_3)_3 9H_2O$[15]	2-methoxyethanol MEA	spin-coating	transparent	$6.2x10^{-4}$ Ωcm	1,5 wt.% Al, preheated at 400 °C + post-heated at 530°C
$Zn(CH_3COO)_2 2H_2O$ $AlCl_3 6H_2O$[16]	Isopropanol MEA	spin-coating	transparent	22Ωcm	1 at.% Al preheated at 275°C + post-heated at 650°C
$Zn(CH_3COO)_2 2H_2O$ $Al(NO_3)_3 9H_2O$[17]	isopropyl alcohol and ethanol	dip-coating	transparent	182Ω/ □	1.0at.% Al . Preheated at 600°C+ post-heated at 600°C
$Zn(CH_3COO)_2 2H_2O$ $Al(NO_3)_3 9H_2O$[18]	Absolute ethanol diethanolamine (DEA)	dip-coating	transparent	$4.2x10^{-3}$ Ωcm	1 at.% Al, preheated at 400 °C + post-heated at 650°C
$Zn(CH_3COO)_2 2H_2O$ $Al(NO_3)_3 9H_2O$[19]		spin-coating	transparent	$1.54x10^{4}$ Ω/□	1.6mol% Al, preheated at 350 °C+ post-heated at 750°C.
$Zn(CH_3COO)_2 2H_2O$ $AlCl_3$[20]	methanol	spin-coating	transparent	$8.68x10^{-4}$ Ω cm	0.8 at.% Al, preheated at 300 °C+ post-heated at 575°C in air + second post-heated at 350°C in H_2
$Zn(CH_3COO)_2 2H_2O$ $Al(NO_3)_3$[21]	Propylene glycol methyl ether (PGME) MEA	spin-coating	transparent	$1.94x10^{-2}$ Ωcm	1 at% Al annealed at 600°C in N_2 + annealed at 500°C in N_2/H_2

Table 4 Summary of sol gel-derived AZO films previously reported

As mentioned before, sol-gel method is a particularly interesting method, because of the low-cost and tunable properties of AZO films. Additionally, it is allowed to prepare large-area coatings. So in this chapter, we synthesis sol-gel derived AZO films and investigate the influence of doping concentration, baking temperature, post-treatment and hydrogen treatment on the optical, electrical properties of AZO films.

4.2 Preparation and structural characterization of AZO films

The properties of AZO films depend on the operating parameters, so it is important to choose the operating parameters before synthesis process. The synthesis process contains three main parts: precursor preparation, deposition of the prepared sol on the substrate and heat treatment of the xerogel film. In each part, there are several operating parameters. Table 5 gives the parameters we used in this work.

	Operating parameters	Our choice
constant parameters	Starting materials	$Zn(CH_3COO)_22H_2O$ and $Al(NO_3)_3$
	solvent	2-methoxyethanol and MEA
	Concentration of zinc	0.8 mol/L
	Synthesis temperature and time	60°C for 1h
	Aging time	48h
	Deposition methods and parameters	Spin-coating with speed of 3000r/min for 30s
	AZO film thickness	250 nm
Variable parameters	Concentration of Al	0 – 5 wt.%
	Baking temperature and time	200°C to 400°C for 10 mins
	Post-annealing temperature and time	500 °C to 700 °C for 1h
	Hydrogen treatment	400 °C to 700°C for 1h

Table 5 Operating parameters used in our work

To prepare oligomer zinc precusor, we have chosen $Zn(CH_3COO)_2.2H_2O$ and $Al(NO_3)_3$ as starting materials, and 2-methoxyethanol and MEA as solvent and additive, respectively. The use of several zinc precursors has been previously reported: nitrate, chloride, perchlorate, acetylacetonate and alkoxides but the most often used is the acetate dehydrate. Metal alkoxides, although they offer several chemical advantages, are not suitable because they are very sensitive to moisture, highly reactive and remain still rather expensive. Because of their low cost, facility of use, and commercial availability, metal salts are interesting as precursors and could be more appropriate for large-scale

applications. Znaidi has written a review in 2010 on sol–gel-deposited ZnO thin films.[22] In this review, he summarized the main chemical routes used in the sol–gel synthesis of undoped ZnO thin films and highlights the chemical and physical parameters influencing their structural properties. He concluded that “the use of organic salts as precursors in alcoholic media remains advantageous, on the one hand because of the low cost and the facility of the metal salt use in general and on the other hand by the fact of avoiding the problems presented by certain inorganic anions and the washing steps. Moreover, using zinc acetate as a precursor, the acetate groups, as contaminants of the gel, decompose under annealing producing combustion volatile by-products. The choice of the solvent has been explained in the chapter 2 as well as the choice of Zn^{2+} concentration which was 0.8 $mol.L^{-1}$.

We stir the mixture of starting materials and solvent at 60 °C for 1h and then leave it to age for 48h at room temperature. Fig.1 shows the complexation in the initial solutions. The oligomer precusor solution were prepared by dissolving the $Zn(CH_3COO)_2 .2H_2O$ in 2-methoxyethanol. The hydrolysis and condensation of Zn^{2+} are relatively slow, the addition of MEA will facilitate the dissolution of zinc salt. MEA acts as complexing agent, which play a role in chelating and stabilizing ligands against precipitation of zinc hydroxide. In the system, there are three nucleophilic species (MEA, CH_3COO^- and HO^-) which can react with the Zn^{2+} lewis acid center. During aging, the small zinc-oxo-acetate oligomers are formed from Zn-MEA or Zn-$OCOCH_3$ soluble complexes. The condensation of the hydrolyzed moieties give rise to colloids or precipitates which are filtered before coating.[23]

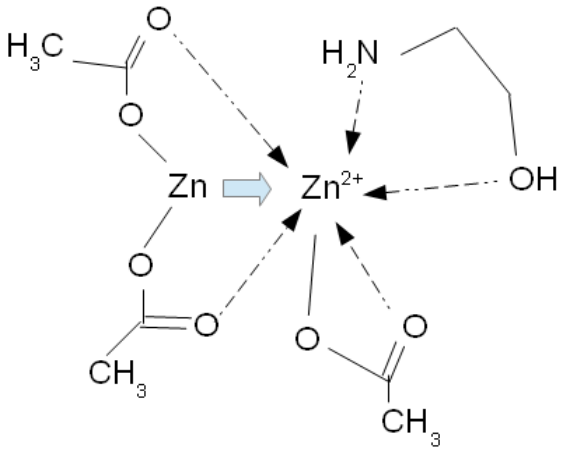

Figure 1 Sketch of chemical equilibria taking place in the initial solutions.

After preparing the initial solution, films are deposited by spin-coating with speed of 3000 r/min for 30s. In order to evaporate the solvent and organic compounds, a pre-heat treatment is performed after each deposition. The process is repeated for several times until the required thickness (250 nm) is reached. Finally, we perform heat treatment to make more crystalline and dense AZO films. Heat treatments, including pre-heat treatment, post-annealing and H_2 treatment, are very important steps governing the film orientation, so it has to be carefully chosen. The baking temperature range we discussed here is from 200 °C to 400 °C, the post-annealing temperature is from 500 °C to 700 °C and the H_2 treatment temperature range is 400 °C to 700 °C. Additionally, Al dopant increases the creat extra carriers, which leads to a big variation of resistivity. But different aluminum doping concentrations are cited in publications to be the optimized concentration for the best conductivity. So we have decided to vary Al doping concentration from 0 wt.% to 5 wt. % and compare the transmittance and electrical properties of AZO films.

Before discussing the influence of these parameters, we study the structural properties of AZO films. Here, AZO films with 2 wt.% Al doping concentration, 200 °C baking temperature and 600 °C post-annealing temperature are used.

4.2.1 Crystal structures

The crystal structures of ZnO are wurtzite, zinc blende, and rocksalt, as shown in fig.2. The zinc-blende ZnO structure can be stabilized only by growth on cubic substrates, and the rocksalt NaCl structure may be obtained at relatively high pressures. The thermodynamically stable phase is wurtzite.

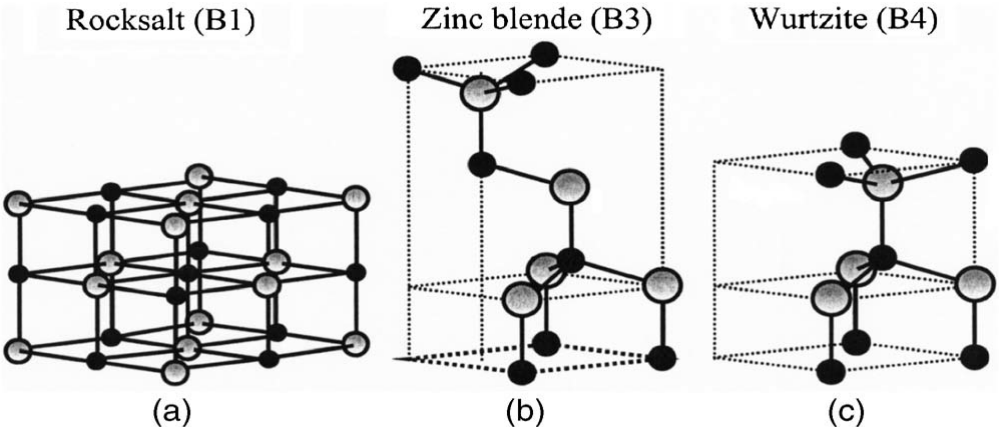

Figure 2 Representation of ZnO crystal structures: (a) rocksalt (*B*1), (b) zinc blende(*B*3), and (c) hexagonal wurtzite (*B*4).The shaded gray and black spheres denote Zn and O atoms, respectively.

The wurtzite structure has a hexagonal unit cell with two lattice parameters a and c (a = 3.249 A, c = 5.205 A) and belongs to the space group C^4_{6v} with two formula units per primitive cell. The Raman active zone-center optical phonons predicted by the group theory are $A_1+E_1+2E_2$. The polar phonons with symmetry A_1 and E_1 exhibit different frequencies for transverse-optic (TO) and longitudinal-optic (LO) phonons. Nonpolar phonon modes with symmetry E_2 have two frequencies, E_2(high) and E_2 (low).[24]

We deposited sol-gel derived AZO films on the SiO_2/Si substrate by spin-coating, and measured their Raman spectrum at room temperature using a LabRAM HR Horiba spectrometer between 200-1300 cm^{-1}. Excitation wavelength we have chosen is 325 nm, because our AZO films are too thin to be detected by visible excitation wavelengths. The excitation power was kept lower than 10 mW in order to avoid thermal decomposition of the samples at the beam focus.

The raman spectrum of AZO films is shown in fig.3. It can be observed that E_2^{high}=438 cm^{-1}, A_1(LO)=570 cm^{-1} and $2A_1$(LO)=1140 cm^{-1} modes are shown in the Raman spectrum of AZO films, which indicates the formation of the wurztite structure. No difference was observed with the increase of aluminum doping concentration.

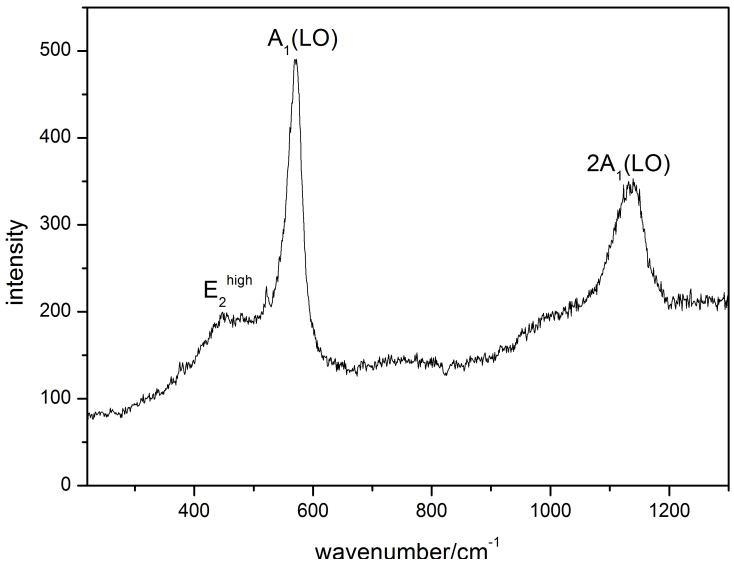

Figure 3 Raman spectrum of Al-doped ZnO thin films

The crystallinity of AZO films were measured by a Rigaku SMARTLAB diffractometer in high resolution mode (Parallel beam or with a Bragg–Brentano geometry) with CuK_α radiation. The scan angle 2θ is between 30 to 40°. Fig.4 shows the XRD patterns of this AZO thin films on SiO_2/Si substrate. It can be seen that a highly c-axis oriented (002) peak

and two weak (100) and (101) peaks are observed at 34°, 31° and 36°, respectively. The films exhibite a strong orientation of the c-axis, which usually has good electrical properties[22].

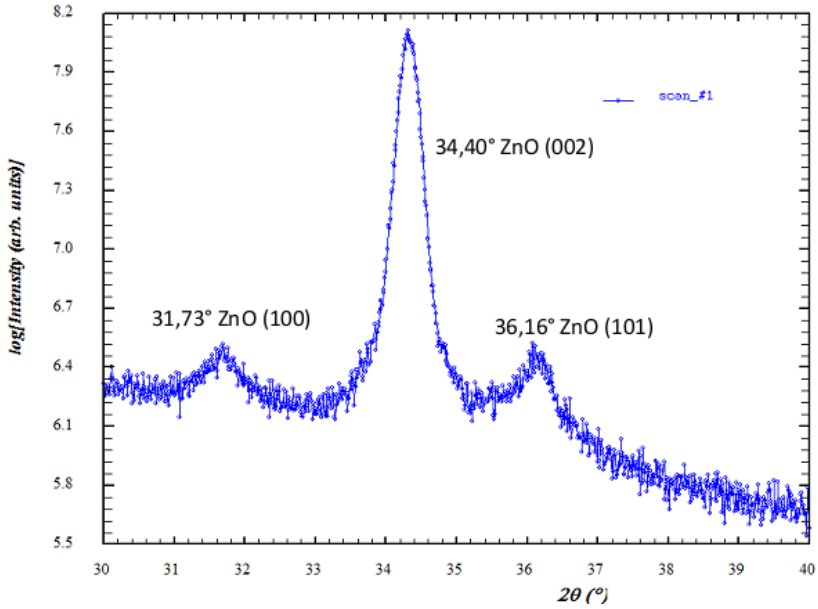

Figure 4 XRD pattern of Al-doped ZnO thin films

Ours XRD results are similar with the results reported in the literature. Indeed, in the review of Znaidi[22], he has tried to find a relation between sol-gel operating parameters and undoped ZnO film orientation. Unfortunately, no clear correlation does exist between each of these parameters and such crystallographic orientation. But he has reported that the use of solvents and additives with higher boiling points, like 2-methoxyethanol and MEA, resulted in strongly preferential orientation of ZnO crystals and thin films. A solvent with a high boiling point would evaporate more slowly on heating, allowing the structural relaxation of the gel film before crystallization.

4.2.2 Surface morphology

Fig.5 shows the SEM images for AZO thin films deposited on SiO_2/Si substrate, (a) is the cross-section SEM image of AZO film, (b) shows the surface of AZO films. The fig.5 (a) reveals that the films are homogeneous on the substrates, and have a thickness of 250 nm. Each film is composed of many fine and compact AZO particles. As shown in fig.5 (b), all AZO particles are uniformly distributed. Inset of fig.5(b) shows two-dimensional AFM surface height morphology of AZO films, proving that the sphere-shaped particles of AZO films are within 50 nm.

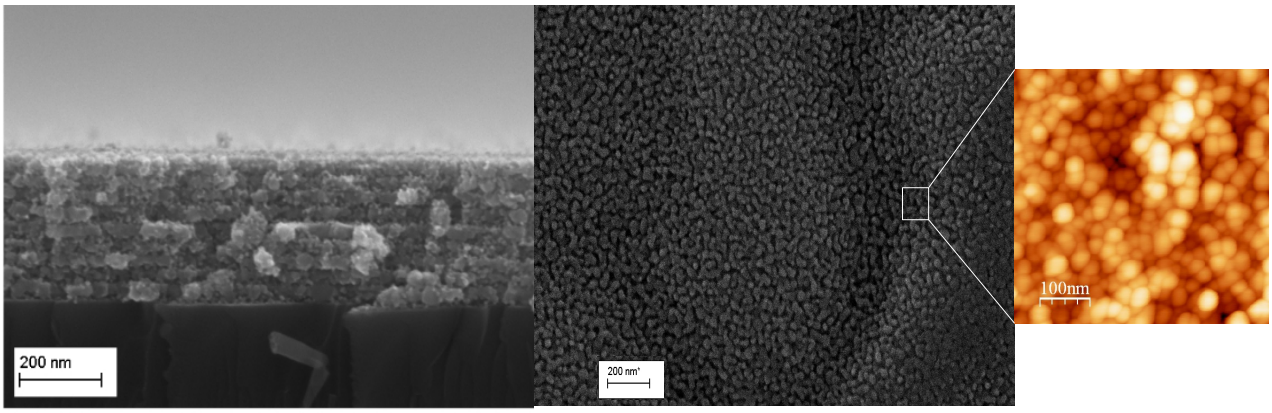

(a) (b)

Figure 5 SEM images of Al-doped ZnO thin films (a) cross-section (b) top-view. The inset of (b) shows the AFM image of AZO films

4.2.3 Defects

Defects are the origin of the conductivity of materials. In ZnO films, Zn_i,V_O^+, H_i^+, Al_i^+ and O_i^- are the main defects[24]. In order to understand the origin of the conductivity of AZO films, it's necessary to study their defects. Typically, photoluminescence (PL) and electron paramagnetic resonance (EPR) are used to study the defects.

Room-temperature Photoluminescence spectra from AZO can exhibit a number of different peaks in the visible spectral region, corresponding to the defect emission. Green emission (~510 nm) is the most commonly observed defect emission in ZnO nanostructures, which is often attributed to singly ionized oxygen vacancies.[21] Yellow defect emission (~564 nm) is typically attributed to an oxygen interstitial. In addition to green and yellow emissions, orange-red emissions are often also observed at 626 nm in ZnO nanorods, and this emission was attributed to oxygen interstitials.[21] As shown in fig.6, the PL spectrum of AZO films in our work shows one broad red-NIR emission centered at about 700 nm, which is due to oxygen interstitials (in the range from 620 nm to 690 nm) and oxygen vacancies (in the range from 690 nm to 750 nm).[24]

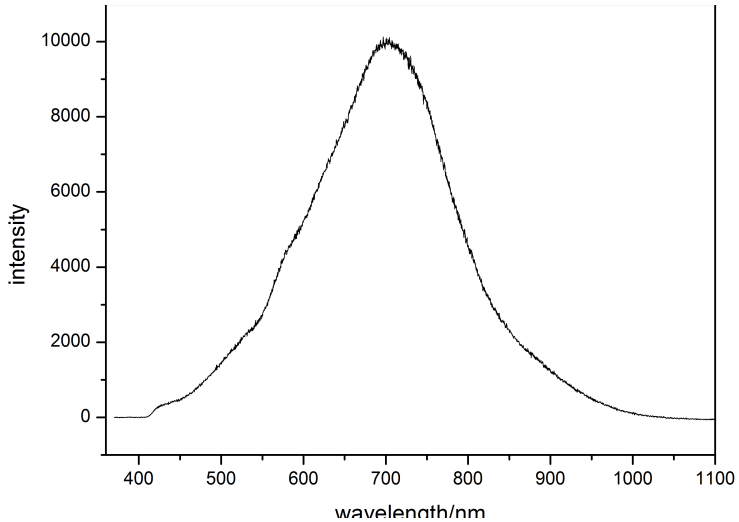

Figure 6 Photoluminescence spectrum of Al-doped ZnO thin films (λ_{exc}=331 nm)

In order to confirm the type of defects in our AZO films, we performed X-band CW-EPR (electron paramagnetic resonance) experiments at room temperature. It is known that every electron has a magnetic moment $s=\frac{1}{2}$ and spin quantum number $m_s=\pm\frac{1}{2}$. In the presence of an external magnetic field, the gap between the $m_s=\frac{1}{2}$ and $m_s=-\frac{1}{2}$ energy states is $\Delta E=g_e\mu_B B_0$, where g_e is the electron's g-factor, μ_B is the Bohr magneton and B_0 is the strength of external magnetic field. When an unpaired electron move from the lower energy level to the higher energy level by absorbing a photon with the energy of $h\nu$, where $h\nu=\Delta E$, a spin resonance occurs. This absorption is monitored and converted into a spectrum. Here, EPR spectrum is recorded as the first derivative of this absorption spectrum.

EPR is a useful tool to investigate defects in the material. Different g-factors are associated with different defects. When g-factor is 1.96, the absorption peaks in AZO film are attributed to shallow donors, such as Zn_i^+ [25-26], substitutional Al atoms[27] or interstitial H_i^+[28]. When g-factor is 1.996, the associated defects could be V_O^+ or O_i^-[29].

Fig.7 shows the EPR spectrum of AZO thin films. This AZO films have only one signal at B_0=3517 Gauss. The operating frequency is at 9.6 GHz, so the g factor can be calculated by equation: $g_e=\frac{h\nu}{B_0\mu_B}$ g =1,99, which is associated with oxygen interstitial and oxygen vacancy[29] .

So the native point defects: oxygen interstitial and oxygen vacancy contribute greatly to the conductivity in AZO films.

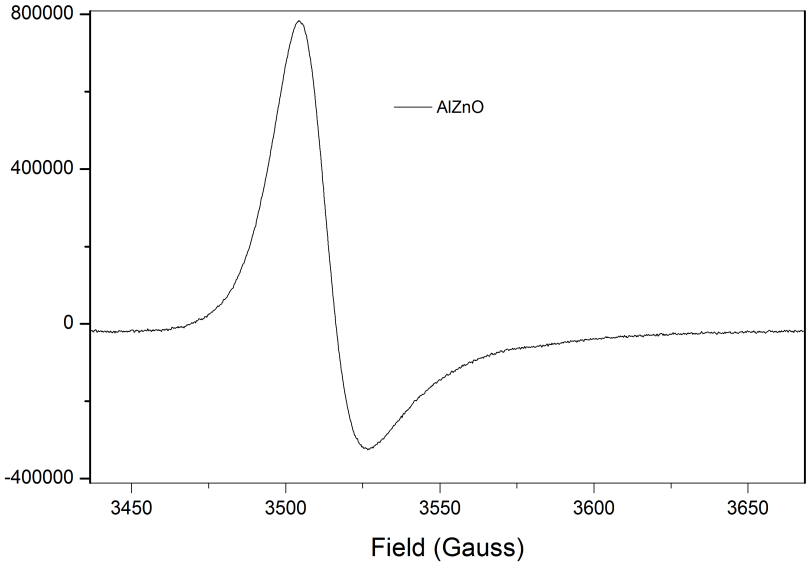

Figure 7 EPR spectra of Al-doped ZnO thin film

4.3 Influence of operating parameters on the properties of AZO films

4.3.1 Influence of doping concentration on the properties of AZO films

As mentioned before, Al doping concentration have an effect on the properties of AZO films. It is well known that the change of the doping concentration will lead to the variation of carrier concentration. According to the burstein-Moss effect, when the carrier concentration increases, the donor electron will occupy the lowest state of the conduction band, which will increase the position of fermi level in the conduction band, so the bandgap will be broadened.[30-32] This broadening will lead to the change of AZO thin film properties. However, high Al concentration does not always increase the carrier concentration, owing to the limited solubility of Al inside ZnO, the extra Al will deform the crystal structure. So the doping concentration range in this work is set from 0 wt.% to 5 wt. %.

Optical properties

The transmittance spectra of AZO thin film as a function of the wavelength at different doping concentration (0 wt.% to 5 wt.%) are shown in fig.8. These thin films were

deposited on quartz under the same heating condition (baking temperature of 200 °C and post annealing temperature of 500 °C in air). We have tried to study the effect of the operating parameters, for example, here, Al^{3+} concentration on the value of the optical band gap but our results are not consistent with the literature. No increase of the value of the optical band gap was observed with the increase of Al^{3+} concentration. Even in the literature, we can find some contradictory results. This problem can be explained by the fact that the optical gap shift is contributed by two competing effects, Burstein-Moss (B-M) band-filling effect and band-gap narrowing (BGN) effect.[1] The well-known optical band-gap (E_g) blue shift in heavily doped semiconductors occurs because the lower states in the conduction band are blocked. Conversely, band-gap narrowing is caused by exchange interactions in the free-electron gas and electrostatic interactions between free electrons and ionized impurities. The fact that BGN effect is largely compensated by B-M effect and temperature or doping are two influence factors in the E_g behavior makes it difficult to separate these two effects by means of current experiments.

Compared to other samples, samples with 0 wt.% and 5 wt.% Al doping concentration have lower transmittance in the visible and near infra-red range but higher transmittance in the ultraviolet range. Increasing the doping concentration from 1 % to 4 %, the transmittance are almost constant. It can be seen that all films have high transparency (transmittance > 80 %) in the visible and near infared region, which is good for photovoltaic application, so in order to optimize the parameters, we compared their electrical properties.

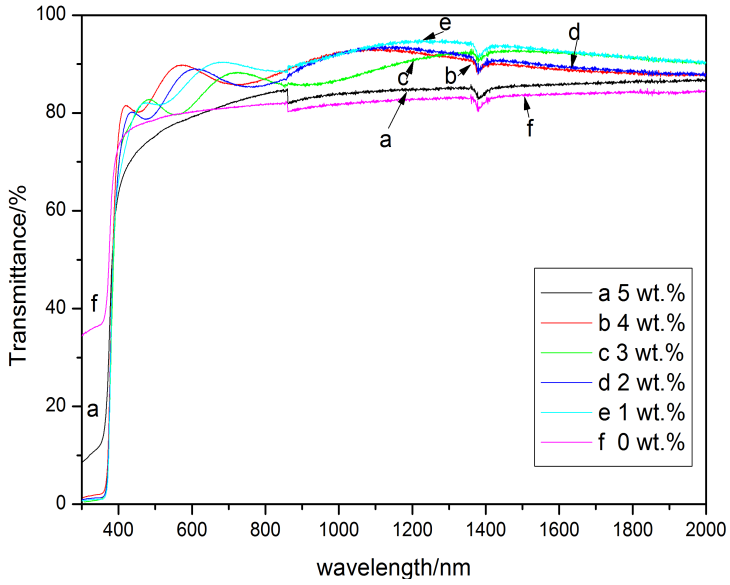

Figure 8 Transmittance spectra of undoped and Al doped ZnO thin films as a function of the wavelength at different doping concentration.

Electrical properties

To measure the electrical properties of AZO films, thin films with different doping concentration were deposited on SiO_2/Si substrate, and the resistivity was obtained by hall effect system measurement. Variation of resistivity of the AZO films with doping concentration are shown in figure 9.

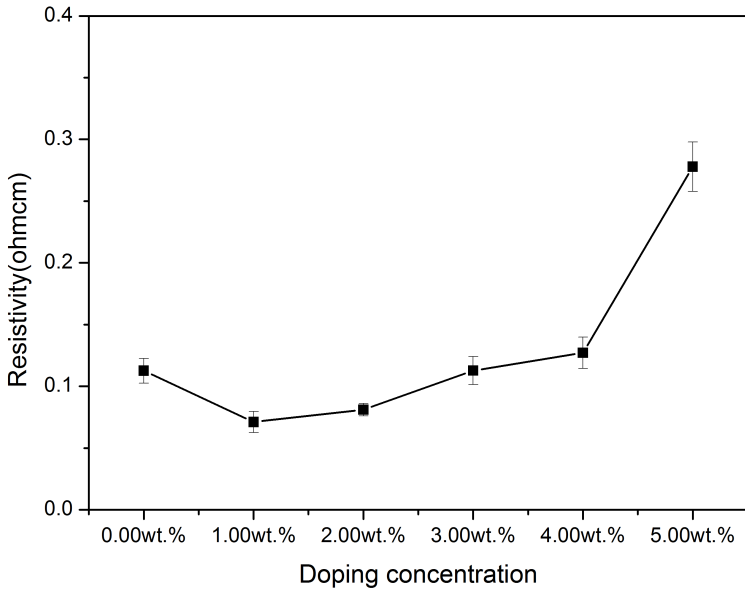

Figure 9 Effect of doping concentration on the resistivity of AZO films

With increasing Al doping concentration, the resistivity of AZO films first decrease. When the doping concentration is up to 1 wt.% and 2 wt.%, the resisitivity is minimal, and then the resisitivity increases with the increase of doping concentration. This is because Al^{3+} can easily substitute Zn^{2+} and creat extra carriers.[31] Resistivity is inversely proportional to the carrier concentration, so the resistivity of AZO are smaller than undoped ZnO. However, when the doping concentration reaches saturation point, Al^{3+} will segregated in the form of Al_2O_3 at the gain boundaries which acts as a trap for free electrons and increase the potential barrier of grain boundary, so the mobility will decrease and resistivity increases.

As shown in table 4, the lowest resistivity is always observed in a limited Al concentration range of 0.5-2 wt.%. In our work, when the same heat treatments are performed, AZO films with 1-2 wt.% shows the lowest resistivity of $7x10^{-2}\Omega cm$ and high transparency, so the optimized Al concentration is between 1 to 2 wt.%.

4.3.2 Influence of baking temperature on the properties of AZO films

After choosing the best doping concentration, we optimize the pre-heat treatment (baking). Baking temperature is one of the most important factors during the synthesis, which governs the film orientation.[22] In table 4, the minimum resistivity is observed when the baking temperature is in the range of 150 °C to 600 °C. The aim of baking is to evaporate the solvent and remove organic compounds, so this temperature should be higher than the boiling point of solvent and close to the crystallization temperature of AZO. The boiling point of 2-methoxyethanol and MEA are 124.6 °C and 171.1 °C, respectively.[22] Fig.10 shows the weight loss as a function of baking temperature. After 400 °C, the weight loss keep constant, which means that zinc acetate decomposition is done and ZnO films are obtained at 400 °C. So the temperature range discussed in this part is from 200 °C to 400 °C.

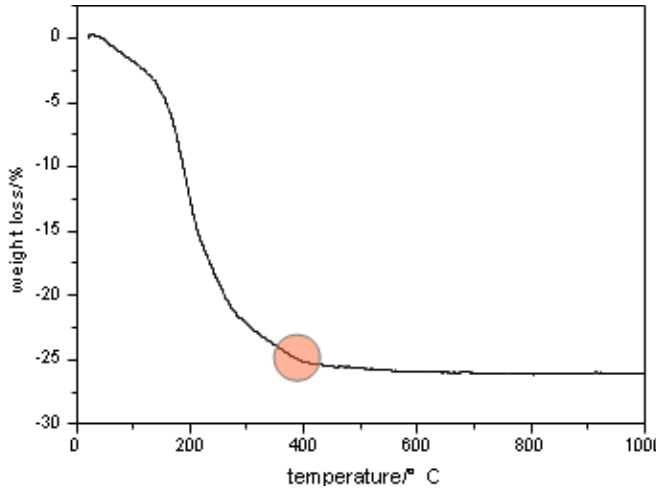

Figure 10 Thermogravimetric analysis curve as a function of temperature

Optical properties

Fig.11 shows the transmittance spectrum of AZO thin film as a function of the wavelength at different baking temperatures. These samples have the same doping concentration of 2 wt%, same post-annealing temperature of 600 °C in air and second post-annealing temperature of 450 °C in H_2. With the increase of the baking temperature from 200 °C to 400 °C, the transmittance first decreases and then increases in the visible and near-infared range. AZO films with 200 °C and 400 °C baking temperature have higher transmittance (>80 %), so in order to use them as transparent electrodes in solar cells, we have to investigate their electrical properties.

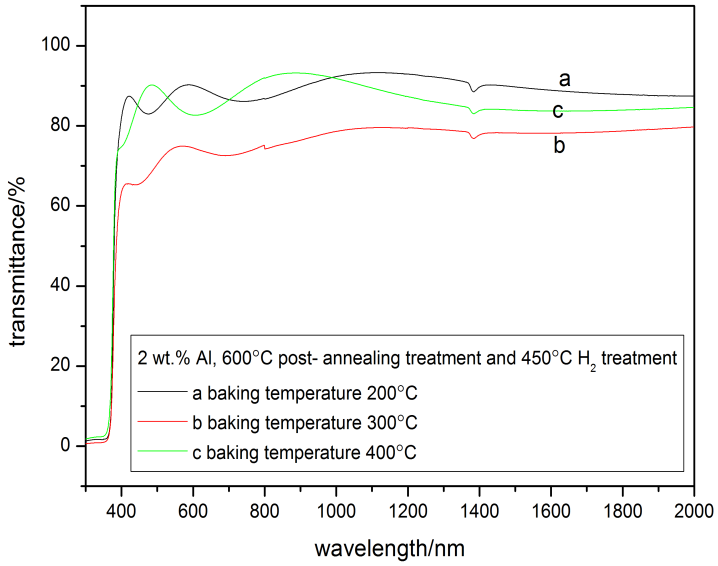

Figure 11 Transmittance spectrum of AZO thin films at different baking temperature

Electrical properties

The variation of resistivity of the AZO films with baking temperature is shown in Fig 12. The results indicate that as the baking temperature goes from 200 °C to 400 °C, the resisitivity reduce significantly, and shows a minimum value of $1.5x10^{-2}$ Ωcm when baking temperature is 400 °C. Increasing temperature will remove more organic compounds which lead to less porosity and make the films denser, so the higher temperature of 400 °C gives the lowest resistivity of $1.5x10^{-2}$ Ωcm and high transparency, so the optimized baking temperature is 400 °C.

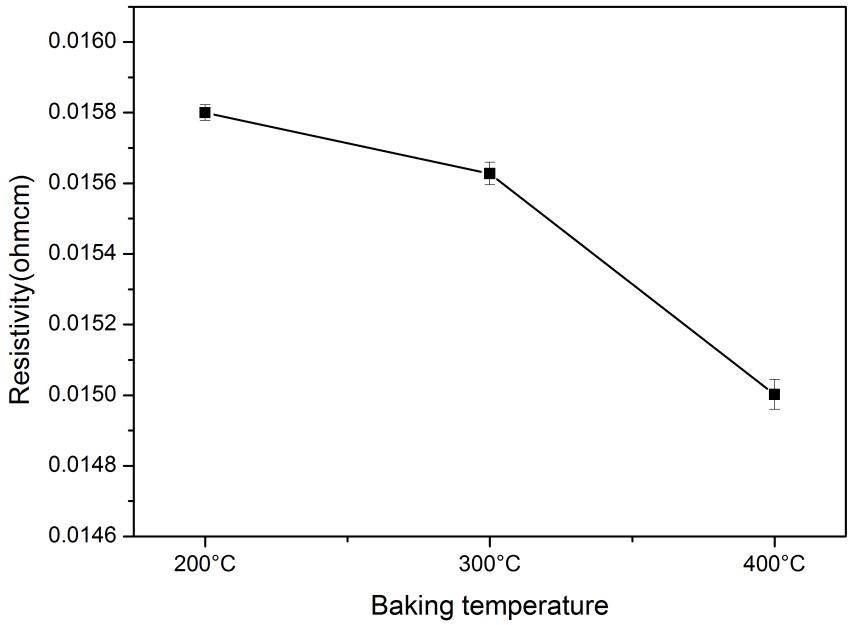

Figure 12 Resistivity of AZO thin films as a function of different baking temperature

4.3.3 Influence of post annealing temperature on the properties of AZO films

Beside the baking temperature, the post annealing temperature is also important for optimization of optical and electrical properties of AZO films. Because as-deposited films are usually amorphous and have a high density of structural defects which affect the properties. The main contributions of this post treatment is to improve the crystallinity as well as chemisorbing or desorbing of oxygen from the grain boundaries.[33-34] This temperature should be higher than the formation temperature of AZO films. As shown before, the formation temperature of AZO is 400 °C, so the post annealing temperature is set from 500 °C.

Optical properties

Fig.13 shows the transmittance spectrum of AZO thin film as a function of the wavelength at different post annealing temperature from 500 °C to 700 °C. These films have the optimized doping concentration of 2 wt% and baking temperature of 200 °C. The results indicate that with the increase of the temperature, the transmittance is almost constant in the visible and near-infared range. So all the tranparency of these samples with different post annealing temperatures are good for solar cells applications.

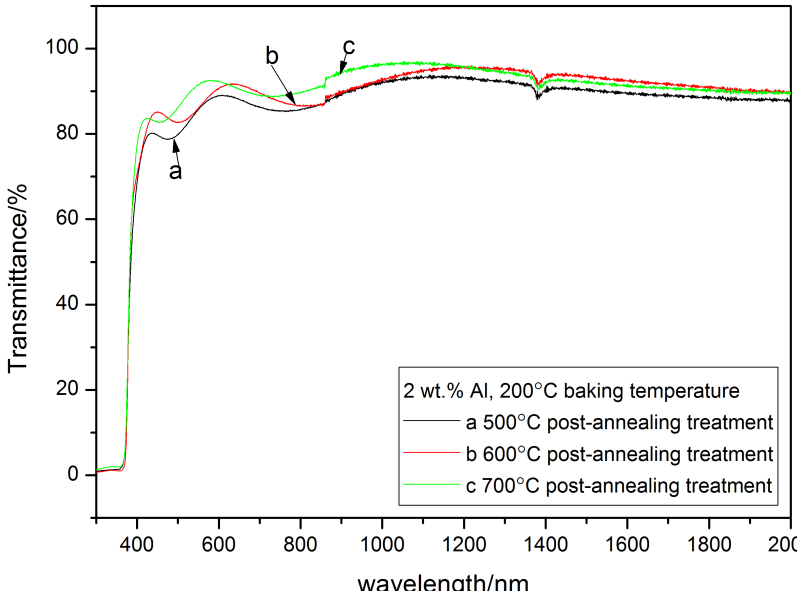

Figure13 Transmittance spectrum of Al doped ZnO thin films as a function of the wavelength at different post annealing temperature

Electrical properties

After investigating the optical properties of samples with different post-annealing temperature, we discuss the influence of these temperatures on the electrical properties of AZO films. The plot of variation of resistivity with temperature for the film are shown in Fig.14. During post annealing treatment, the reactions for dissolution of Al_2O_3 in ZnO might be formulated as below:

$$Al_2O_3 \rightarrow 2\mathrm{Al}^{\cdot}_{Zn} + 2\mathrm{O}^{x}_{O} + \frac{1}{2}O_{2(g)} + 2e \quad [35]$$

If the heat treatment atmosphere is air, the oxygen will diffuse into the film, removing oxygen vacancies and then reducing the carrier concentration. However, when the temperature is smaller than 600 °C, the crystallinity and grain size increase with the increase of temperature, the decrease in resistivity is mainly attributed to these competitive effects. The minimum resistivity of $3.3x10^{-2}$ Ωcm corresponds to the sample with post annealing temperature of 600 °C.

But when it is further annealed after the formation of crystalline phase, the resistivity increases, due to the diffusion of oxygen and decrease of carrier concentration.

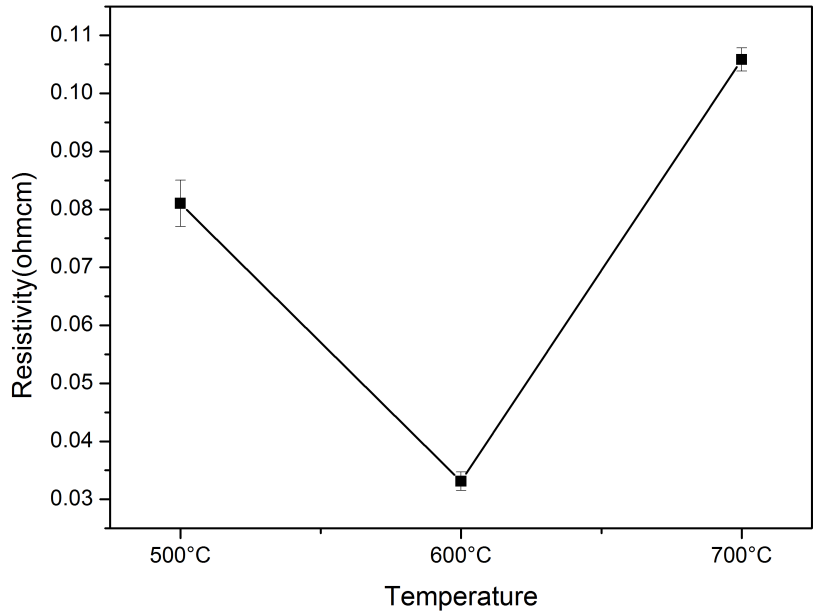

Figure14 Resistivity of Al doped ZnO thin films as a function of different post annealing temperature

4.3.4 Influence of hydrogen treatment on the properties of AZO films

In table 4, some researchers performed second annealing in reduced atmosphere after post-annealing treatment, and the samples they obtained show lower resistivity compared to other samples without this step. In order to further decrease the resistivity of AZO films, we performed this heat treatment in hydrogen gas. As discussed before, the oxidizing atmosphere will absorb oxygen and decrease the carrier concentration. If the hydrogen treatment is performed, it will remove the absorbed oxygen and increase the oxygen vacancies, so the resistivity will decrease. On the other hand, because the reaction $ZnO+H_2=Zn+H_2O$ happens when the temperature is above 400 °C, which produces the interstitial zinc atoms, according to the reaction:

$ZnO - O_O \rightarrow Zn_i^{\cdot} + e^{'} + \frac{1}{2} O_2(g)$, this increase of Zn_i will bring more native point defects and decrease the resistivity[36]. However, the influence of hydrogen treatment temperature on the properties of AZO films is still under consideration[37-38], and will be discussed in this part.

Optical properties

Fig.15 shows the transmittance spectrum of AZO thin film without and with hydrogen treatment as a function of the wavelength. These samples have the same doping concentration of 2 wt.%, baking temperature of 200 °C and post-annealing temperature of 600 °C. The results indicate that this hydrogen treatment will shift the wavelength of the absorption edge to the higher energy side, which is due to the increase of carrier concentration caused by this treatment, and resulting in the broadening of the bandgap, so called Burstein-Moss effect.

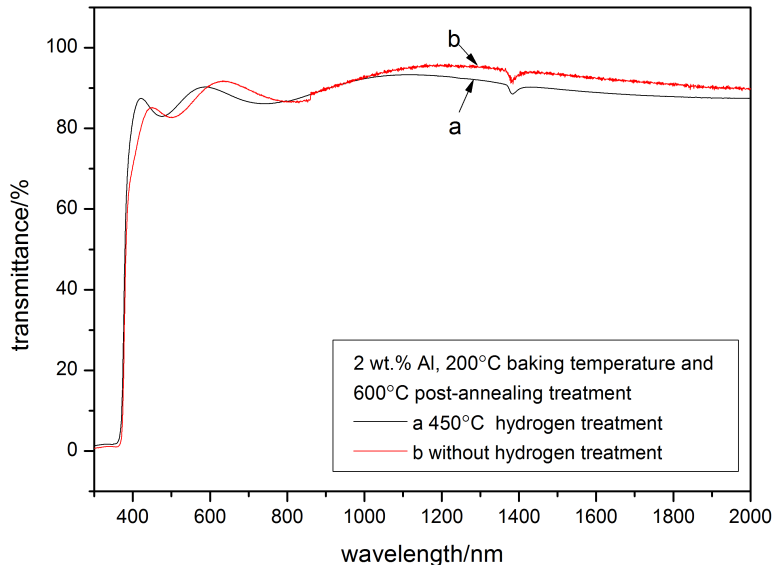

Figure 15 Transmittance spectrum of Al doped ZnO thin films without and with hydrogen treatment as a function of the wavelength

Electrical properties

The plot of variation of resistivity with different hydrogen treatment temperatures for the film are shown in Fig .16. It can be seen that hydrogen treatment decreases the resistivity of AZO films compared to the sample without hydrogen treatment and the lowest resistivity

of $1.6x10^{-2}$ Ωcm is observed at the temperature from 400 °C to 500 °C, but at the temperature > 500 °C, the resistivity significantly increases.

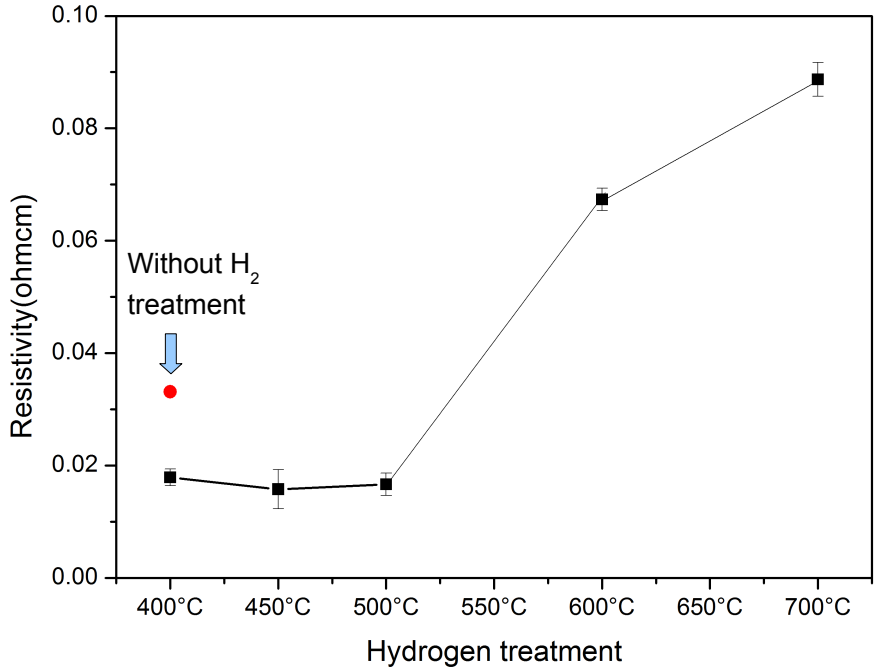

Figure15 Resistivity of Al doped ZnO thin films as a function of different hydrogen treatment temperature

Conclusion

Al doped ZnO films have been synthesized by sol-gel method, which exhibit wurtizite structure with (002) preferred orientation of grain growth. AFM and SEM images show an uniform particles distribution in the films. The resistivity of these AZO films is dominated by electrons generated by oxygen vacancies and oxygen interstitials. Sol-gel technology is a low-cost and simple method compared to other technology, however, the operating parameters can affect the properties of AZO films, such as Al concentration, pre- and post-heat treatment and hydrogen treatment.

Al^{3+} concentration strongly influences the optical and electrical properties of thin films. When the baking temperature and post annealing temperature are 200 °C and 500 °C, respectively, AZO films with doping concentration from 1 wt.% to 2 wt.% show the lowest resistivity of $7x10^{-2}$ Ωcm.

When the doping concentration is 2 wt.%, the best post-annealing temperature is 600 °C and hydrogen treatment temperature is 450 °C, AZO films with baking temperature of 400 °C show the lowest resistivity of $1.5x10^{-2}$ Ωcm.

When the doping concentration is 2 wt.%, baking temperature is 200 °C, AZO films with post annealing temperature of 600 °C show the lowest resistivity of $3.3x10^{-2}$ Ωcm.

When the doping concentration is 2 wt.%, baking temperature is 200 °C and post-annealing temperature is 600 °C, AZO films with hydrogen treatment temperature from 400 °C to 500 °C show the lowest resistivity of $1.6x10^{-2}$ Ωcm.

Transmittance spectra indicate that all these films have high transmittance (above 80 %) in the visible and NIR region.

So the optimized sample is the one with doping concentration is 2 wt.%, baking temperature is 400 °C, post-annealing temperature is 600 °C and hydrogen treatment temperature of 450 °C, which has the minimum resistivity of $1.5x10^{-2}$ Ωcm and a transmittance >80 %.

However, compared to AZO films made by other methods, the resistivity is still under improvement.

[1]T. Minami, Transparent conducting oxide semiconductors for transparent electrodes. Semiconductor science and technology. 20, 35 (2005).

[2] H. Liu, V. Avrutin e*t al*. Transparent conducting oxides for electrode applications in light emitting and absorbing devices. Superlattices and Microstructures. 48, 458 (2010).

[3] S. Calnan, A. N. Tiwari. High mobility transparent conducting oxides for thin film solar cells. Thin Solid Films. 518, 1839 (2010).

[4] T. Minami, T. Miyata. Present status and future prospects for development of non- or reduced-indium transparent conducting oxide thin films. Thin Solid Films. 517, 1474 (2008).

[5]A Stadler. Transparent Conducting Oxides—An Up-To-Date Overview, Materials 2012, 5, 661 (2012).

[6] R. Romero, D. Leinen *et al*. The effects of zinc acetate and zinc chloride precursors on the preferred crystalline orientation of ZnO and Al-doped ZnO thin films obtained by spray pyrolysis. Thin Solid Films. 515, 1942 (2006).

[7] R. O. Ndong, F. P. Delannoy *et al*. Structural properties of zinc oxide thin films prepared by r.f.magnetron sputtering. Materials Science and Engineering B. 97, 68 (2003).

[8] E. Guziewicz, M. Godlewski. ALD grown zinc oxide with controllable electrical properties. Semiconductor Science and Technology. 27, 074011 (2012).

[9] V. Musat, B. Teixeir *et al*. Al-doped ZnO thin films by sol–gel method. Surface and Coatings Technology. 180, 659 (2004).

[10] N. D. M. Sin, M. H. Mamat *et al*. Electrically conductive zinc oxide (ZnO) nanostructures prepared by sol-gel spin-coating. AIP Conference Proceedings. 1341, 48 (2011).

[11] V. Musat, B. Teixeir *et al*. Effect of post-heat treatment on the electrical and optical properties of ZnO:Al thin films. Thin Solid Films. 502, 219 (2006) .

[12] J. H. Lee, K. H. Ko *et al*. Electrical and optical properties of ZnO transparent conducting films by the sol–gel method. Journal of Crystal Growth. 247, 119 (2003).

[13] R. Ghosh, G. K. Paul *et al*. Effect of thermal annealing treatment on structural,electrical and optical properties of transparent sol–gel ZnO thin films. Materials Research Bulletin. 40, 1905 (2005).

[14] X. Z. Qiang, D. Hong *et al*. Al-doping effects on structure, electrical and optical properties of c-axis-orientated ZnO:Al thin films. Materials Science in Semiconductor

Processing. 9, 132 (2006).
[15] Y. S. Kim, W. P. Tai *et al*. Electrical and optical properties of Al-doped ZnO thin films by sol–gel process. Applied Surface Science. 253, 4911 (2007).
[16] K. M. Lin, P. J. Tsai *et al*. Parametric study on preparation and characterization of ZnO:Al films by sol–gel method for solar cells. Materials Science and Engineering B. 139, 81 (2007).
[17] K. E. Lee, M. S. Wang *et al*. Structural, electrical and optical properties of sol–gel AZO thin films. Current Applied Physics. 9, 683 (2009) .
[18] S. Y. Kuo, W. C. Chen *et al*. Effects of doping concentration and annealing temperature on properties of highly-oriented Al-doped ZnO films. Journal of Crystal Growth. 287, 78 (2006).
[19] P. Sagar, M. Kumar *et al*. Influence of hydrogen incorporation in sol-gel derived aluminum doped ZnO thin films. Thin Solid Films. 489, 94 (2005).
[20] W. J. Chen, W. L. Liu *et al*. Synthesis of ZnO:Al Transparent Conductive Thin Films Using Sol-gel Method. Procedia Engineering. 36, 54 (2012).
[21] A. B .Djurisic, Y .H. Leung *et al*.. Green, yellow, and orange defect emmision from ZnO nanostructures: Influence of excitation wavelength. Applied Physics Letters. 88,103107 (2006).
[22] L. Znaidi. Sol–gel-deposited ZnO thin films: A review. Materials Science and Engineering B. 174, 18 (2010).
[23] L. Znaidi, G. J. A. A. S. Illia *et al*. Oriented ZnO thin films synthesis by sol-gel process for laser application. Thin solid films. 428, 257 (2003).
[24] Ü. Özgür, Y. I. Alivov *et al*. A comprehensive review of ZnO materials and devices. Journal of Applied Physics. 98, 041301 (2005).
[25] M. D. McCluskey and S. J. Jokela. Defects in ZnO. Journal of Applied Physics. 106, 071101 (2009).
[26] L. S. Vlasenko and G. D. Watkins. Optical detection of electron paramagnetic resonance for intrinsic defects produced in ZnO by 2.5-MeV electron irradiation in situ at 4.2 K. Physics Review B. 72, 035203 (2005).
[27] S. B. Orlinskii and J. Schmidt. Identification of shallow Al donors in Al-doped ZnO nanocrystals: EPR and ENDOR spectroscopy. Physics Review B. 77, 115334 (2008).

[28] J. K. Park, K. W. Lee *et al*. Magnetic resonance spectroscopy of hydrogen shallow donors in aluminum-doped zinc oxide prepared by sol–gel processing. Solid State Communications. 152,116 (2012).

[29] L. S. Vlasenko. Magnetic Resonance Studies of Intrinsic Defects in ZnO: Oxygen Vacancy. Applied Magnetic Resonance. 39,103 (2010).

[30] M. H. Mamat, M. Z. Sahdan *et al*. Optical and electrical properties of aluminum doped zinc oxide thin films at various doping concentrations. Journal of the Ceramic Society of Japan.117, 1263 (2009).

[31] H. Wang, M. H. Xu *et al*. Low temperature synthesis of sol-gel derived Al-doped ZnO thin films with rapid thermal annealing process. Journal of Materials Science: Materials in Electronics. 21, 589 (2010).

[32] R. Vinodkumar, I. Navas *et al*. Highly conductive and transparent laser ablated nanostructured Al:ZnO thin films. Applied Surface Science. 257, 708 (2010).

[33] M. Ohyama. Sol-gel preparation of transparent and conductive Aluminum-doped Zinc oxide films with highly preferential crystal orientation. Journal of the American Ceramic Society. 81, 1662 (1998).

[34] P. Nunes, E. Fortunato *et al*. Influence of the post-treatment on the properties of ZnO thin films. Thin Solid Films. 383, 277 (2001).

[35] J. P. Lin and J. M. Wu. The effect of annealing processes on electronic properties of sol-gel derived Al-doped ZnO films. Applied Physics Letters. 92,134103 (2008).

[36] J. F. Chang, W. C. Lin *et al*. Effects of post-annealing on the structure and properties of Al-doped zinc oxide films. Applied Surface Science.183, 18 (2001).

[37] P. D. C. King and T. D. Veal. Conductivity in transparent oxide semiconductors. Journal of Physics: Condensed Matter. 23, 334214 (2011).

[38] M. D. McCluskey, M. C. Tarun *et al.* Hydrogen in oxide semiconductors. Journal of Materials Research. 27, 2190 (2012).

Chapter 5 Realization and characterization of solar cell

After discussing the influence of geometry on the optical properties of Si nanopillars (or nanocones) and optimizing the optical and electrical properties of AZO transparent films by varying the operating parameters, we fabricate complete solar cells based on Si nanopillars (or nanocones). Intrinsic and n^+-doped polysilicon are deposited on the top of Si nanopillars (or nanocones) in turn to form n^+-i-p junctions which are used to separate photogenerated electron-hole pairs. After, we deposite AZO antireflection coatings on the top of n^+-i-p junction to reduce the optical loss. In addition, AZO films form conformal coatings to enhance the electrical properties of solar cells. To complete the solar cell, front contact and back contact are deposited on the top of AZO films and p-type Si wafer, respectively. The structure of solar cells is shown in fig.1.

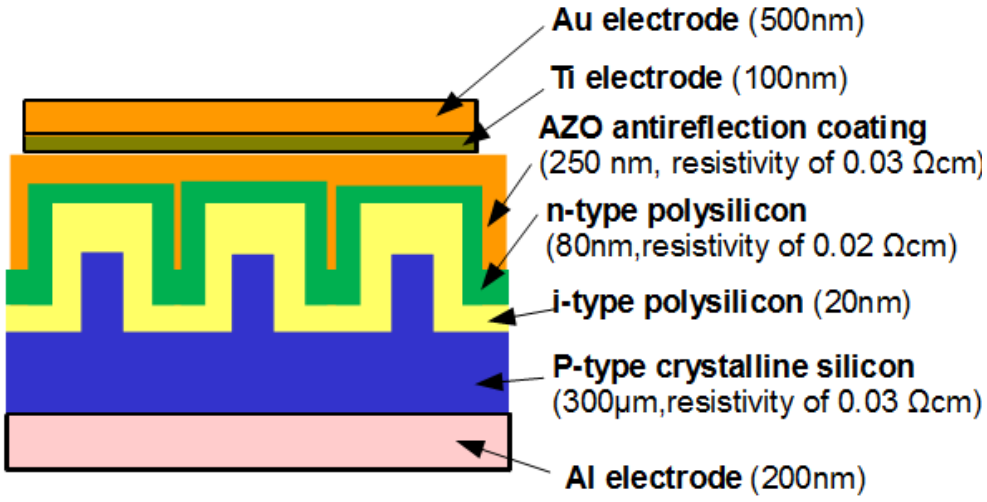

Figure 1 Illustration of solar cells structure based on nanopillars

However, the efficiency of this solar cell is not ideal. First of all, the defects on the rough surfaces of Si nanopillars (or nanocones) made by plasma etching are not negligible[1], and a source of performance degradation of electronic devices, including transport properties and resistivity[2]. Second, defects located at grain boundary in polysilicon will also deteriorate the efficiency of solar cells. So it is necessary to perform passivation of nanopillars and polysilicon in order to decrease defect concentration.

In this chapter, we integrate the complete solar cells and then perform different passivation and investigate the influence of passivation of nanopillars and polysilicon on the electrical properties of solar cells. Finally, we discuss the influence of AZO films on the

optical and electrical properties of solar cells.

5.1 The influence of passivation on the properties of solar cell

Defects on the surface of Si wafer or nanopillars (nanocones) made by plasma etching can change the interface properties of pn junction, so they have to be removed before forming pn junction. Typically, these surfaces are treated by wet oxidation and then the generated SiO_2 layer are removed by HF etching[1-3].

The high resolution TEM images (see fig.2) show the comparison between the surface of nanowires obtained by plasma etching with the step of wet oxidation and without wet oxidation step. It can be seen that after oxidation, the disordered surface is reduced and the atomically abrupt surface is obtained.[3]

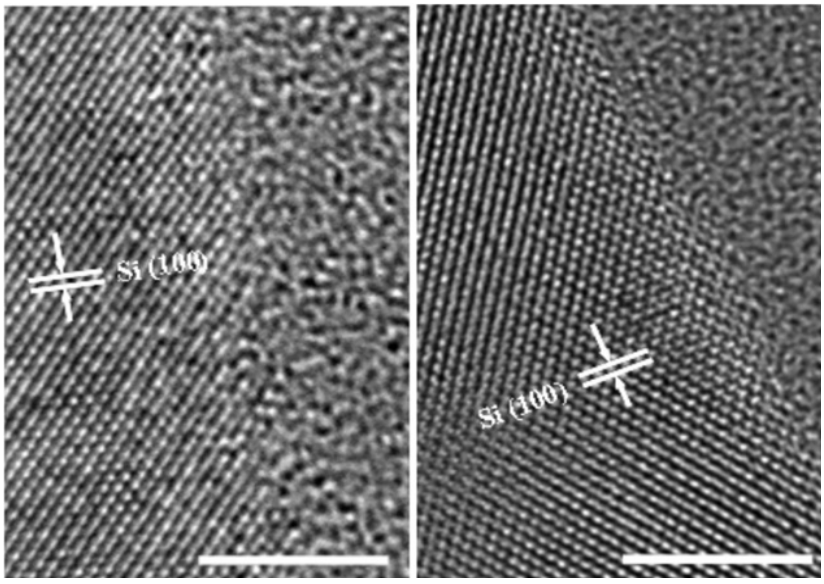

Figure 2. HRTEM images showing the Si NW surface after RIE etching (left) and after the oxidation step (right). An atomically abrupt Si NW surface has been obtained. Scale bar is 5 nm.[3]

This reduction of defects can also be detected by other methods. It has been reported that surface passivations have an effect on the transport properties of SiNWs.[3] A five order difference in effective carrier concentration was observed, when comparing SiNWs fabricated with and without a thermal oxide. And the removal of the surface oxide by HF treatment results in a SiNW conductance drop up to six orders of magnitude[2].

Regarding the defects associated with grain boundary in polysilicon, one way to decrease the defects is to increase the grain size by RTA (rapid thermal anneal). During RTA process, the grains grow to minimize grain boundary area and reduce the overall

surface energy.[4] However, this way is not sufficient because the defects in the form of Si dangling bonds in polysilicon still exist after RTA process. Hydrogen has the ability to bond to the dangling bonds and passivate these defects. So hydrogen passivation is useful. There are several ways to introduce hydrogen into Si, such as annealing in hydrogen gas at high temperatures(more than 900 °C), SiNx:H and H_2 plasma.

Simulations[5] show that hydrogenation from a gas source at a few hundred degrees Celsius is very inefficient, except in the presence of surface damage. Experimental results found that shallow impurities in Si can be passivated by annealing in H_2 at high temperature and quenching to room temperature, and the total number of shallow centers passivated by this method is comparable to that of the hydrogen plasma passivation at moderated temperature (in the range of 200- 600 °C).

Hydrogen plasma passivation is an effective method to dissociate H_2 gas and provide sufficient atomic H with a large kinetic energy, so they easily adsorb on the surface and passivate the defects. However, the quality of passivation depends on the passivation parameters, especailly temperature and time, because the in-diffusion and out-diffusion of H vary with the change of these two parameters. Higher temperature leads to a fast H diffusion, but prolonged passivation time creates new defects and disorder.[6]

The most widely used passivation way in virtually all solar cells (laboratory and industrial) is depositing silicon nitrate (SiNx:H) onto the surface of polysilicon and performing a thermal annealing to make H diffusing into the materials.[7] Without annealing, H atom are still linked to Si or to nitrogen, so they cannot participate to the passivation. Compared to hydrogen plasma passivation, SiNx:H passivation leads to an increase of solar cell properties without damage to the surface.[8]

In this work, we investigate the effect of three different passivation treatments (wet oxidation passivation and two different hydrogen passivation treatments) of planar solar cells. First of all, we perform two different hydrogen passivation of polysilicon on planar solar cells, the first method employs annealing in hydrogen gas and the second method is to deposit SiNx:H films and then perform annealing treatment. The quality of passivation is characterized by I-V curves in dark and under illumination. Second, we perform wet oxidation passivation on the planar solar cells. The main objective is to choose an efficient passivation, which leads to a higher efficiency of solar cells. Finally, we passivate nanocones solar cells in the most efficient way and compare their quality of passivation

with that of planar solar cells.

5.1.1 The influence of passivation on the properties of planar solar cell

Hydrogen passivation

After depositing intrinsic and n-type polysilicon on the same Si wafer to form planar n^+-i-p junction, we cut this wafer into three pieces (see fig.3). Sample A without treatment is kept as a reference, sample B is annealed in H_2 gas at 900 °C for 2 hours and sample C is covered with 100 nm SiNx:H films, which are prepared by plasma-enhanced CVD with a mixture of SiH_4 (5 % N_2) and NH_3, the deposition temperature is 340 °C, pressure is 1 Torr and the power is 10 W. After that, sample C is annealed at 500 °C in Ar for 30 mins to make H diffuse into polysilicon and then the SiNx:H films are removed by HF.

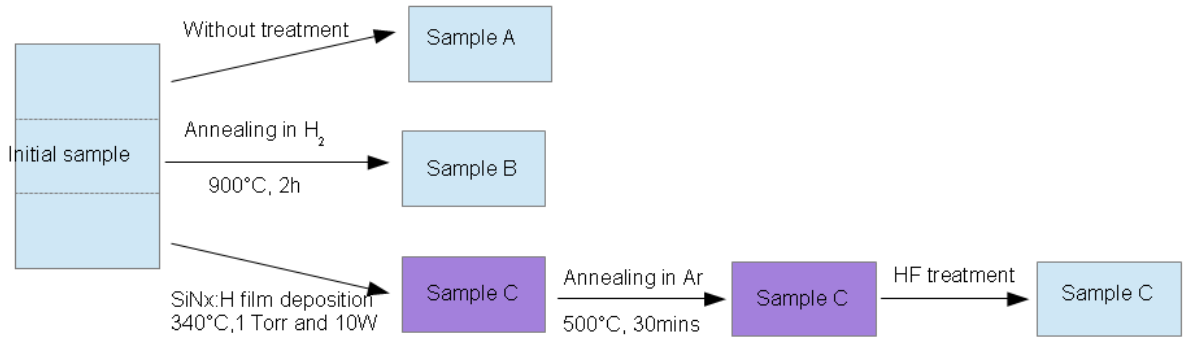

Figure 3 Schematic illustration of hydrogen passivation experiment

To measure the I-V curves of these samples, we deposite 100 nm Ti and 500 nm Au on the top of these three samples as front contact and deposite 200 nm Al as the back contact.

Fig.4 shows the I-V curve of planar n^+-i-p junctions with different hydrogen passivation compared to the one without passivation. Sample A (without passivation) has an nearly linear I-V curve with leakage current of 3.5 mA (for a reverse voltage of 0.2 V) and no threshold voltage, i.e. it is almost ohmic contact, which cannot separate electron-hole pairs. So in order to use it as a solar cell, we have to passivate it.

Compared to sample A, sample B (with hydrogen annealing passivation) has the leakage current of 17 mA when reverse voltage is 0.2 V, i.e. a 5 fold increase. So this passivation brings more recombination. This is because thermal annealing at 900 °C (higher than polysilicon deposition temperature of 700 °C) will activate doping atoms.

When the doping concentration increases, the resistance and the diffusion length decrease, so the recombination increases. So this hydrogen annealing passivation is not efficient.

It's can be seen that SiNx:H films passivation treatment improves the quality of n^+-i-p junction. As shown in fig.4, the leakage current of sample C is 0.3 mA at reverse voltage of 0.2 V. SiNx:H films passivation treatment decreases the leakage current by a factor of 10. Additionally, sample C has a threshold voltage closed to that of standard p-n junction. So Sample C is suitable for solar cell applications.

To passivate polysilicon, annealing has to be performed after SiNx:H films depostion. However, this annealing temperature (500 °C) is not high enough to activate doping atoms, so it doesn't bring more recombination as hydrogen annealing passivation. At the same time, during annealing, SiNx:H films will release H atoms, which diffuse into polysilicon and reduce dangling bonds. So this passivation method is more efficient to improve the quality of n+-i-p junction.

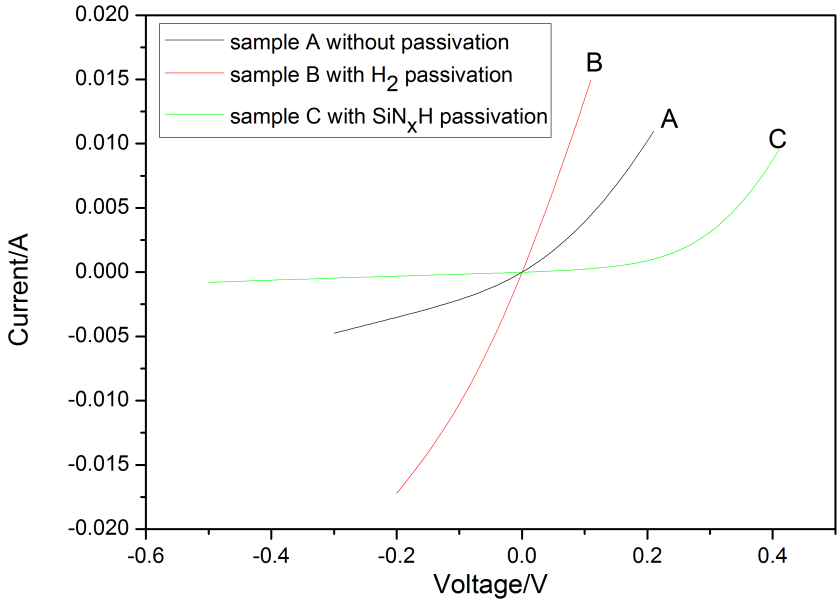

Figure 4 I-V curve of planar n+-i-p junction, sample A is the solar cell without passivation, sample B is the solar cell with hydrogen annealing passivation and sample C is the solar cell with SiNx:H passivation

Fig.5 compares the electrical characteristics under illumination of planar n+-i-p junction solar cells with and without SiNx:H passivation.

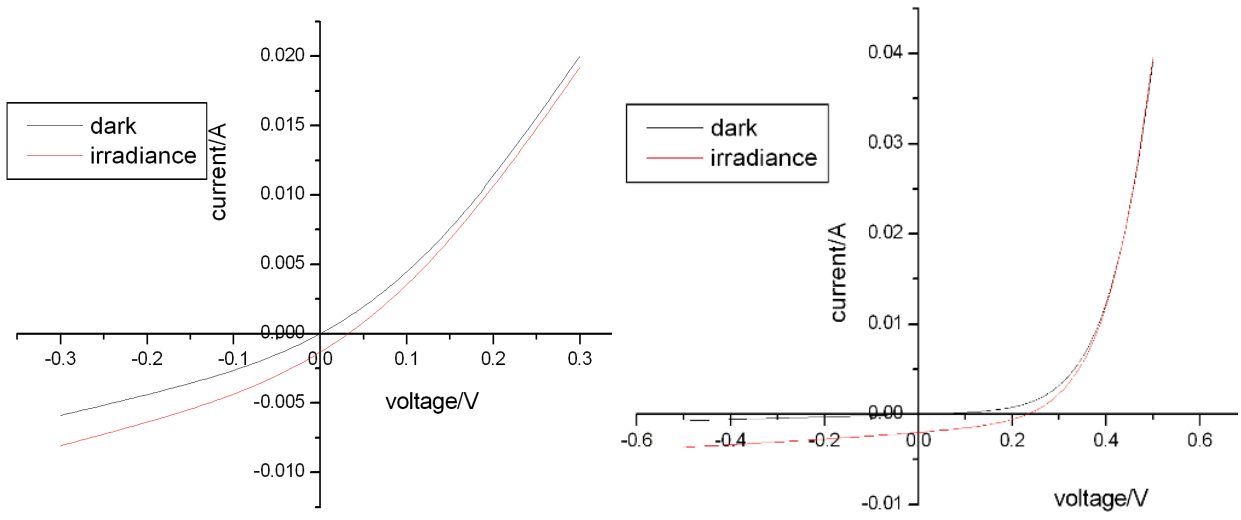

(a) (b)

Figure 5 I-V curve in dark and under illumination of (a) sample A planar n+-i-p junction solar cells without passivation and (b) sample C planar n+-i-p junction solar cells with SiNx:H passivation

The quality of the solar cell yield is associated to the efficiency factor, η, given by the Oriel® IV test station software: $\eta = \frac{P_{max}}{(P_0 * S_{sample})}$, where S_{sample} is the sample area, P_0 is the power of the illuminator and P_{max} is the maximum power of the solar cell. However, the sample area exposed to the illuminator is smaller than the sample area owing to the metal mask and because of the limited diffusion length, the effective collection area is much smaller than the overall illuminated surface. So we have to take these two factors into consideration and normalize the efficiency by the equation: $normalized\ \eta = \frac{\eta * S_{sample}}{S_{eff}}$, where S_{eff} is the effective collection area exposed to the illuminator. If the area exposed to the illuminator light is far away from the rim of the electrode (> 1.5 mm), the collected photogenerated carrier is negligible (see part 5.2.2). So the S_{eff} is the yellow area around the electrode, and the distance between the rim of this area and electrode is 1.5 mm, as shown in fig.6. S_{eff} for sample with U-shape electrode and the sample with two small circular electrodes are 44 mm² and 6.28 mm², respectively. Both sample A and Sample C with U-shape electrode have the effective area of 44 mm² (sample area is 1 cm²).

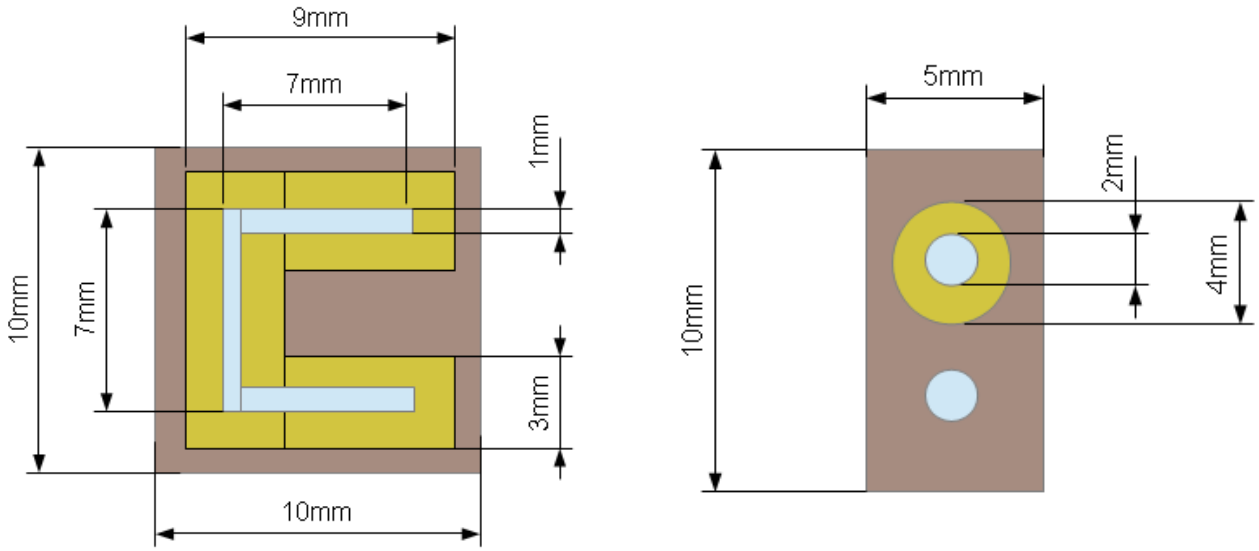

(a) (b)

Figure 6 Schema of effective area expose to the source, (a) samples with U-shape electrode and (b) samples with two small circular electrodes. The yellow part is the effective carrier collection area, the blue part is the electrodes and the light brown square is the sample.

Table 1 lists the solar cell parameters of sample A and sample B. It is observed from table 1 that after SiNx:H passivation, the normalized efficiency of n+-i-p junction increases from 0.02 % to 0.36 %, i.e. a 18-fold increase. The measured open circuit voltage V_{oc} of the reference sample is 32 mV under AM1.5 conditions. After SiNx:H passivation, V_{oc} is 231 mV. This passivation increase V_{oc} by a factor of 6. It has been reported that the improvement of V_{oc} by SiNx:H passivation (PECVD deposition at 400 °C and annealing in nitrogen at 500 °C) is of the order of 70 %. So this passivation significantly improves the efficiency of solar cells.

sample	V_{oc} (mV)	Jsc (mA/cm²)	Efficiency (%)	Normalized efficiency (%)
A	32	1.3	0.01	0.02
C	231	2.0	0.16	0.36

Table 1 Solar cell parameters of sample A and sample C

Wet oxidation passivation

Polysilicon surface passivation has been discussed before and SiNx:H passivation is an efficient way. In addition, the surface of Si nanopillars (nanocones) or Si wafer should be

passivated to have better n+-i-p junction. So before forming n+-i-p junction, we perform wet oxidation in tubular furnace at 950 °C under a flow of 1.5 slm (standard litre per minute) of O_2, 2.5 slm of H_2 for 32 mins and remove SiO_2 by HF solution. After this passivation, we deposit polysilicon and perform SiNx:H passivation (making SiNx:H films, annealing them in Ar and then removing SiNx:H films). In the end, we deposite electrodes (see part 2.3.1 in chapter 2) to complete the solar cells.

Fig.7 shows the I-V curve of planar n+-i-p junction solar cells with wet oxidation and SiNx:H passivation (sample D) and planar n+-i-p junction solar cells with SiNx:H passivation (sample C). It can be seen that wet oxidation passivation decreases the leakage current, compared to the sample with only SiNx:H passivation. Table 2 shows the leakage current of sample A, B, C and D. The addition of wet oxidation decreases the leakage current by a factor of 30, compared to the sample C which has the leakage current of 0.3 mA at voltage of -0.2V. So the sample with wet oxidation and SiNx:H passivation is more close to the ideal n+-i-p junction, which is beneficial to solar cell application.

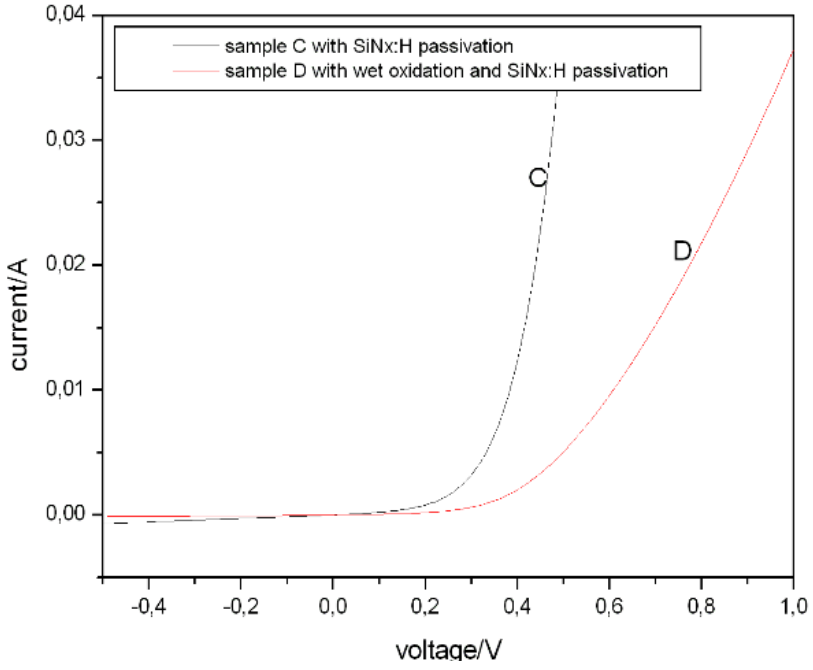

Figure 7 I-V curve of sample C and sample D

Sample	Leakage current / mA (at reverse voltage of 0.2V)
A	3.5
B	17
C	0.3
D	0.01

Table 2 Electrical parameters of sample A, B, C and D

Table 3 represents the efficiencies and normalized efficiencies of these two solar cells. Sample D with two small circular electrodes has the effective collection area of 6.28 mm². The improvement of efficiency associated with the wet oxidation passivation is of the order of 11 %. So both of the passivations are important to solar cell applications. SiNx:H passivation improves the efficiency by a factor of 18 and the combination of SiNx:H passivation and wet oxidation improve the efficiency of our samples by a factor of 20.

sample	Efficiency(%)	Normalized efficiency(%)
C	0.16	0.36
D	0.05	0.40

Table 3 Efficiency of sample C (n+-i-p junction solar cells with SiNx:H passivation) and sample D (with wet oxidation and SiNx:H passivation)

5.1.2 The influence of passivations on the properties of nanocones solar cells

The combination of SiNx:H passivation and wet oxidation significantly improve the efficiency of planar solar cells. Because there are more defects on the surface of nanocones, the efficiency of solar cell without passivation is negligible. We carry out the combination of two passivation on nanocones n+-i-p junction solar cells. It is expected that the efficiencies of nanocones solar cells will be also improved.

Sample E is the passivated solar cells based on nanocones with top diameter of 375 nm, bottom diameter of 804 nm and length of 340 nm, and sample F is the one based on nanocones with top diameter of 414 nm, bottom diameter of 880 nm and length of 480 nm (see fig.10 in chapter 3). Fig.8 plots the I-V curves of these two different nanocones n+-i-p junction solar cells with wet oxidation and SiNx:H passivation compared to planar solar cells with same passivation treatment. The leakage current and threshold voltage of nanocones solar cells are comparable to planar solar cells, as shown in table 4, while the

series resistance of nanocones solar cells are bigger than that of planar solar cells.

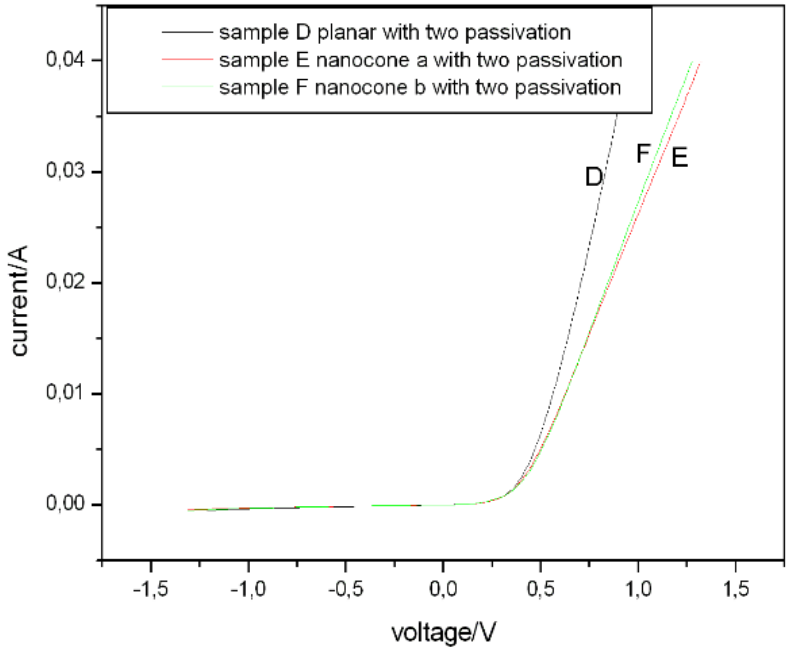

Figure 8 I-V curve of nanocones n+-i-p junction solar cells with SiNx:H passivation and wet oxidation Sample D is planar solar cells, sample E is the solar cell based on nanocones with top diameter of 375 nm, bottom diameter of 804 nm and length of 340 nm and sample F is the solar cell based on nanocones with top diameter of 414 nm, bottom diameter of 880 nm and length of 480 nm.

Sample	Leakage current / mA (at reverse voltage of 0.2V)	Series resistance (Ω)
D	0.01	13
E	0.01	23
F	0.01	24

Table 4 Electrical parameters of sample D, E and F

Fig.9 shows the efficiency improvement of planar solar cells and nanocones solar cells after passivation. It can be observed that after passivation, the normalized efficiency of nanocones solar cell (sample F) increases up to 0.4 %, which is comparable to that of the planar solar cells. The efficiency improvement of this nanocones solar cells is larger than that of planar solar cells after passivation, due to the passivation of a higher defect concentration.

The efficiency of sample E (0.32 %) is smaller than that of sample F (0.4 %). This is because nanocones of sample E has higher reflectance (average reflectance is 30 %) than sample F (average reflectance is 25 %), as shown in fig.11 in chapter 3. Samples with

lower reflectance have higher absorption which leads to a higher efficiency.

As the reflectance of these two nanocones are not optimized (see chapter 3), the efficiencies of solar cells based on them are not ideal. Due to the technical problem, it's impossible to fabricate nanocones with all the different shapes, instead, we optimize the absorption of nanocones by a complementary simulation. But the simulation takes a lot of time. In order to continue the experiment, we integrate solar cells on as-prepared nanocones no matter how big the reflectance is, because the main object is to choose the efficient passivation method. It is expected that after two passivations, solar cells based on optimized nanocones will have higher efficiency than planar solar cells.

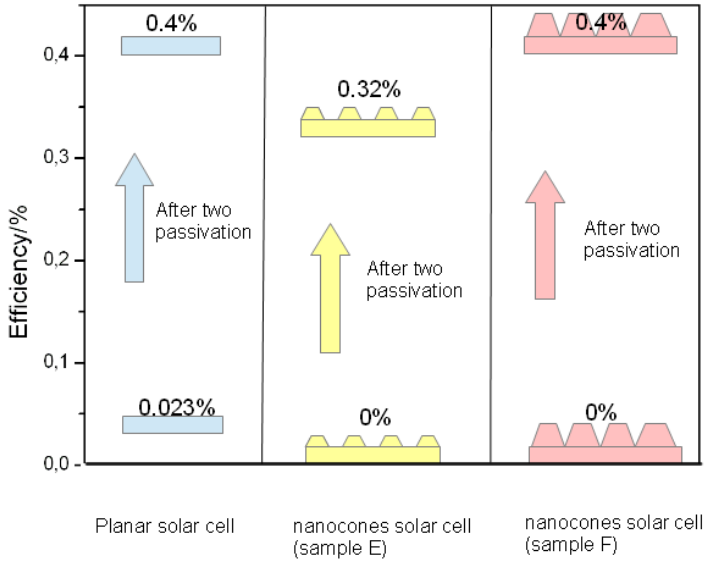

Figure 9 Efficiency improvement of planar solar cells and two different nanocones solar cell (sample E and sample F). Yellow part represents sample E and red part represents sample F

5.2 The influence of AZO films on the properties of solar cells

Because of the high refractive index of Si (n=3.5 at λ=600 nm), the reflection of bare silicon is over 30 %, which is calculated by:

$R=\left(\frac{n_0-n_{Si}}{n_0+n_{Si}}\right)^2$ n_0 is the refractive index of the surroundings (air) which is equal to 1 and n_{Si} is the refractive index of Si. This optical loss is one of the reasons why the efficiency of solar cells is lower. This can be reduced by introducing nanostructure (nanopillars or nanocones) or applying anti-reflection coatings (ARC). In the second approach, to achieve low reflectance, the refractive index of the anti-reflection coating is the geometric mean of

that of the materials on either side. This is expressed by:

$n_1 = \sqrt{n_0 n_{Si}}$, n_1 is the refractive index of anti-reflection coating. When n_0=1 and n_{Si}=3.5, n_1 should be equal to 1.87. Typically, ARC layers are TiO_2 and SiN_x:H, and these ARC layers are not electrically conductive material, so the forming of front-metal contact is a problem. [9]

Here, we use sol-gel derived AZO films. Ellipsometry measurements result shows that AZO films we made has the refractive index of 1.86 which is suitable to be a ARC layer. Unlike SiNx:H films, AZO films and gold forms an ohmic contact[10]. Additionally, it has been found the AZO films form conformal coatings to enhance the electrical properties of solar cells.

In this part, we deposited AZO films on the planar, nanopillars and nanocones n+-i-p junction to investigate the effect of AZO films on the optical properties of solar cells. And then we study the effect of AZO conformal coatings on the electrical properties of solar cells.

5.2.1 The influence of AZO films on the optical properties of solar cells

To begin with, we deposit AZO films with 2 wt.% doping concentration on planar, nanopillars and nanocones n+-i-p junctions by spin coating, and then we perform heat treatment in air at 600 °C for 1h. The resisitivity of this transparent AZO films is 0.03 Ωcm. SEM images of nanocones n+-i-p junction with and without AZO films are shown in fig.10. The bright films in fig.10 (b) is AZO films. It is observed that AZO made by sol-gel methods forms homogenous films on the top of nanocones.

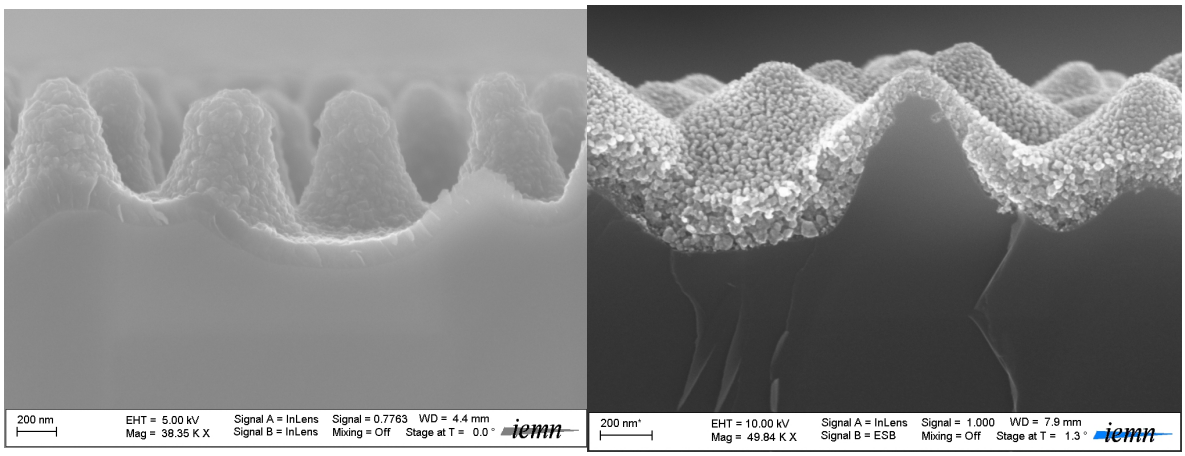

(a) (b)

Fig.10 SEM images of (a) nanocones n+-i-p junction without AZO films and (b) with AZO films

We measure the reflectance spectra of these samples and compare them with the reflectance of planar n+-i-p junction withou AZO films. Fig.11 shows the reflectance spectra of planar n+-i-p junction without AZO films and planar, nanopillars and nanocones n+-i-p junction with AZO films. It can be seen that the reflectance spectra of planar solar cell with AZO films shows great oscillations. Neverthless, the addition of AZO film significantly decreases the average reflectance of planar solar cell, as illustrated in table 5. The decrease is of the order of 46 %.

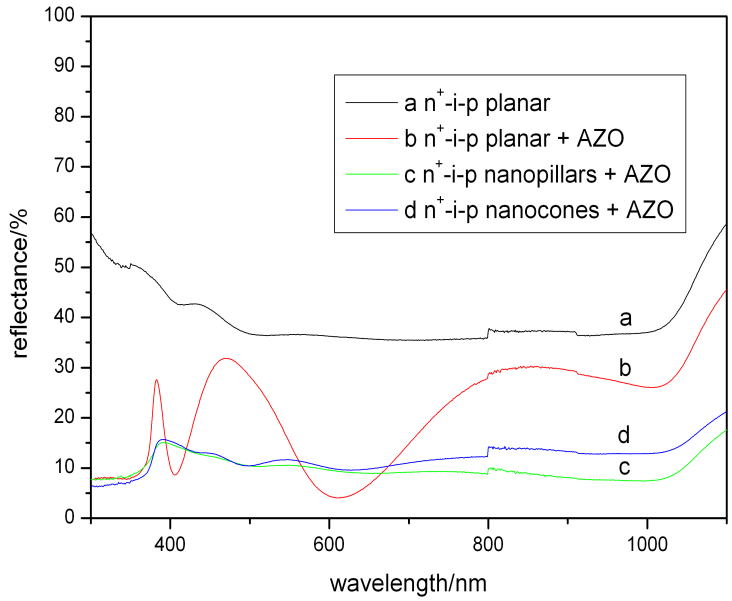

Figure 11 Reflectance spectra of planar n+-i-p junction without AZO films, planar, nanopillars and nanocones n+-i-p junction with AZO films.

samples	Average reflectance (%)
Planar junction	39.8
Planar junction+AZO	21.48
Nanopillars junction + AZO	9.86
Nanocones junction+AZO	12.17

Table 5 Average reflectance of different solar cells

These oscillations correspond to the optical interference effect between the AZO films and substrate[11-12]. As shown in fig.12, the optical path difference δ between R_1 and R_2 is equal to $2 d n_1 * \cos\theta$, where d is the thickness of AZO films (250 nm) and n_1 is its refractive index. If the light strikes the film at normal incidence angle (θ=0°), constructive interference occurs when $2 d n_1 = m \lambda$ (1), where m is integer and λ is the wavelength of

incident light. And destructive interference when $2n_1 d = (m - \frac{1}{2})\lambda$ (2). Fig.13 shows the refractive index of our AZO films. It can be caclulated that when λ=384 nm, 477 nm and 880 nm with m=3, 2 and 1, respectively, constructive interference occurs following equation (1), which agrees with experiment results. When λ=409 nm and 610 nm with m=2.5 and 1.5, respectively, so the destructive interference occurs following equation (2), in agreement with experimental results (see fig.11 (b)).

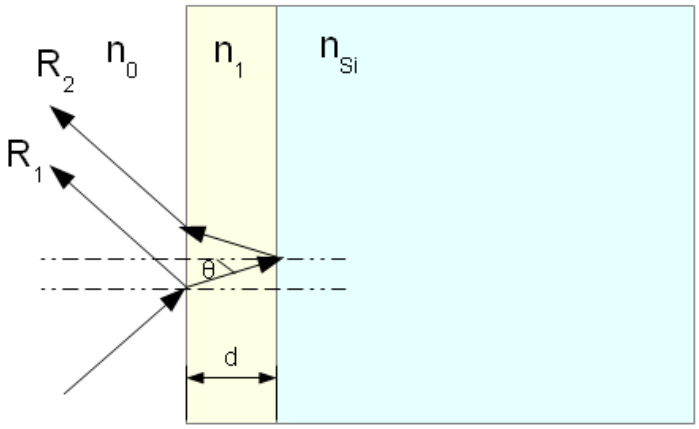

Figure 12 Schematic diagram showing the interference effect

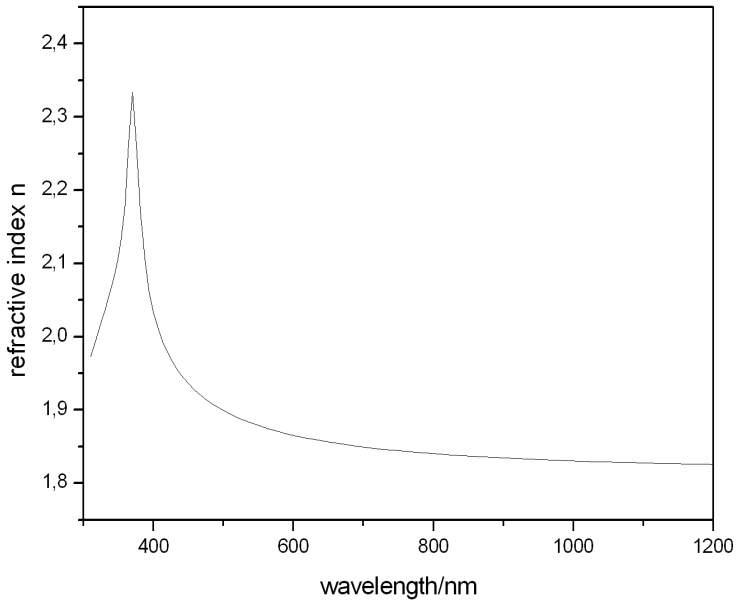

Figure 13 Measured refractive index of AZO as a function of wavelength

The addition of nanostructures will further decrease the reflectance of solar cells. Nanocones and nanopillars solar cells with AZO films have the average reflectance of 12.17 % and 9.86 %, respectively. This decrease is associated with the decrease of

effective refractive index, according to ref.11 and 13. The effective refractive index of nanostructure is $n_{eff}=[n_1^2 f+n_0^2(1-f)]^{\frac{1}{2}}$,where f is the filling factor. Concerning about nanostructure covered with AZO films, $n_{eff}=[n_{eff0}^2 f+n_0^2(1-f)]^{\frac{1}{2}}$ $n_{eff0}=n_1 f'+n_{Si}(1-f')$, where f' is the fraction of AZO.

The calculated effective refractive index profiles of nanocones and nanopillars solar cells with AZO films are shown in fig.14. AZO films deposited on nanopillars will have constant effective index of 3,2, which provides an intermediate refractive index step. And AZO films have a graded transition of the effective refractive index from 1 to 1.87, leading to the decrease of the reflectance.

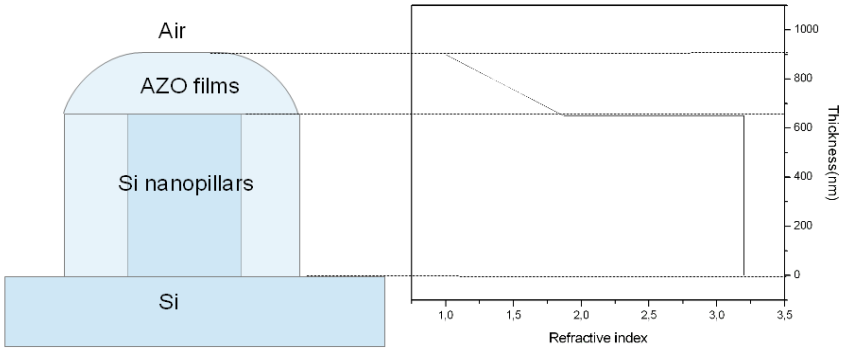

(a)

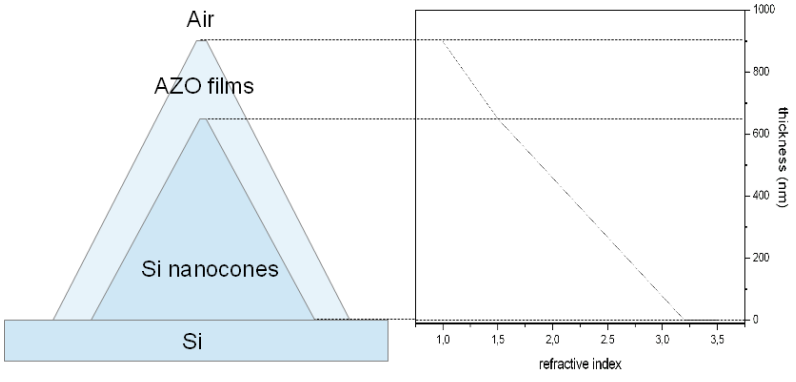

(b)

Figure 14 Calculated effective refractive index profiles of AZO/Si structure. (a) nanopillars solar cell (b) nanocones solar cell

AZO films deposited on nanocones will have a gradient effective refractive index from 1.55 to 3.2, which will have better antireflective properties in broad range of

wavelength[12,14].

So AZO films with adaptive refractive index decrease the reflectance of silicon planar solar cell, and the addition of nanostructure will further decrease the reflectance owing to the effective refractive index profile. Since this refractive index profile depends on the ratio of AZO films and Si nanostructures and also depends on the filling factor of nanostructures, the next work should be the optimization of the AZO/Si nanostructure.

5.2.2 The influence of AZO films on the electrical properties of solar cells

AZO films can be used as ARC layers, and because of their electrically conductive properties, it would be interesting to study their effect on the electrical properties of solar cells. Electrodes contacts are deposited on AZO films by evaporation. To form ohmic contact, we perform a thermal annealing (600 °C) after gold deposition. It is known that Au will be incorporated into silicon during high thermal process, which will deteriorate the performance of solar cells. Here, AZO films will prevent the gold diffusion inside silicon.

In this part, we measure the photocurrent of nanocones solar cells with AZO film when the light spot is focused on different position along z axis, as shown in fig.15, and compare them with the result of solar cells without AZO film to investigate the effect of AZO films on electrical properties of solar cells.

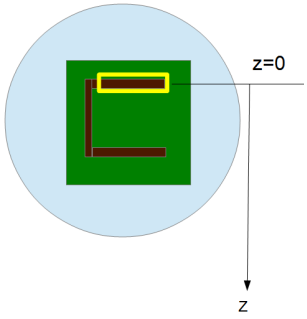

Figure 15 Illustation of photocurrent measurement of solar cells with U-shape electrode, black square is the solar cell and blue hollow square is the incident light spot which will move along z axis during mearement

Fig.16 plots the photocurrent density of solar cells with and without AZO films as a function of light spot positon. When we move the light spot along z axis, the photocurrent changes associated with effective carrier collection area. Solar cell without AZO films shows a decay ratio (which is the ratio of maximum photocurrent density and minimum photocurrent density) is 12. The addition of AZO films decreases it by a factor of 5, i.e. the

effective carrier collection area of solar cell with AZO films is better.

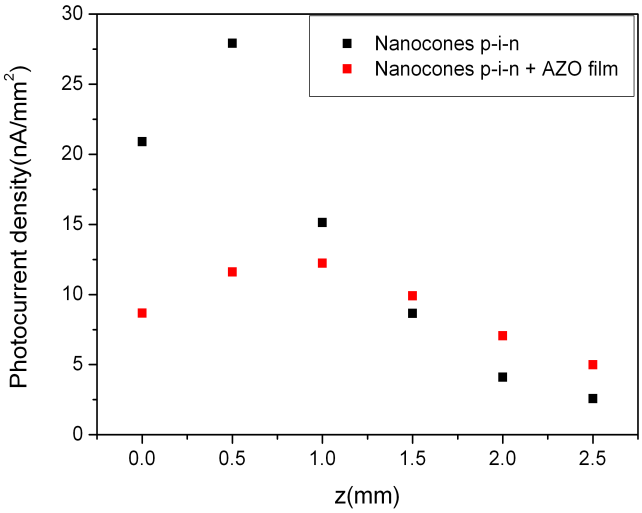

Figure 16 Photocurent density of solar cells as a function of light spot position, black square represent the results of nanocones solar cells without AZO films and red square represent the results of solar cells with AZO films

However, the photocurrent density of solar cell with AZO films is smaller than that of solar cell without AZO films. As discussed before, the addition of AZO films significantly decreases the reflectance, so the photocurrent should be improved. However, the resistivity of AZO films (0.03 Ωcm) used here is comparable to that of Si (0.02 Ωcm), and this leads to the increase of serial resistance and the decrease of photocurrent.

Conclusion

In this part, in order to make complete solar cell with higher efficiency, first, we have investigated the effect of hydrogen passivation and wet oxidation passivation on the electrical properties of solar cells. Then, we have studied the influence of AZO films on the optical and electrical properties of solar cells.

It is observed that SiNx:H passivation improve the efficiency of our planar solar cells by a factor of 18 and the combination of SiNx:H passivation and wet oxidation improve the efficiency by a factor of 20. So these two passivation methods are efficienct and necessary for improving the solar cell efficiency.

Because there are more defects in nanocones, the efficiency of nanocones solar cells without passivation is negligible. After the two passivations, the efficiency of nanocones

solar cells is comparable to that of planar solar cells. A significant improvement is achieved. It is expected that after two passivations, solar cells based on nanocones with optimized absorption will have higher efficiency than planar solar cells.

Equally important, the addition of AZO films decreases the reflectance of solar cells and AZO films combined with nanostructure will further decrease the reflectance, but AZO/ Si nanostructures have to be optimized.

The electrical properties of solar cells are also enhanced by adding AZO conformal coatings. The effective carrier collection area increase by a factor of 5 when adding AZO films. However, because the resistivity of AZO films is comparable to that of Si, an associated series resitance is added to the solar cells and the photocurrent decreases.

So in order to increase the photocurrent intensity of solar cells, the next step would be the optimization of AZO films.

[1] G. S. Oehrlein, R. M. Tromp *et al*. Study of silicon contamination and near surface damage caused by CF4/H2 reactive ion etching. Applied Physics Letter. 45, 420 (1984).
[2] U. K. Bhaskar, T. Pardoen *et al.* Surface states and conductivity of silicon nano-wires. Journal of Applied Physics. 113, 134502 (2013).
[3] X. L. Han, G. Larrieu *et al.* Realization of ultra dense arrays of vertical silicon nanowires with defect free surface and perfect anisotropy using a top-down approach. Microelectronic Engineering. 88, 2622 (2011).
[4] M. L. Terry, D. Inns *et al*. Rapid Thermal annealing and hydrogen passivation of polycrystalline silicon thin-film solar cells on low-temperature glass. Advances in OptoElectronics. 2007, 1 (2007).
[5] I. A. Veloarisoa, M. Stavola *et al*. Passivation of shallow impurities in Si by annealing in H_2 at high temperature. Applied Physics Letters. 59, 2121 (1991).
[6] S. Honda, T. Matesa *et al*. Defects generation by hydrogen passivation of polycrystalline silicon thin films. Solar Energy. 80, 653 (2006).
[7] B. Gorka. Hydrogen passivation of polycrystalline Si thin film solar cells. (2010). (thesis)
[8] A. Slaoui, E. Pihan *et al*. Passivation and etching of fine-grained polycrystalline silicon films by hydrogen treatment. Solar Energy Materials and Solar Cells. 90, 2087(2006).
[9] B. Sopori, V. Mehta *et al*. Fundamental mechanisms in the fire-through contact metallization of si solar cells: a review. 17th Workshop on Crystalline Silicon Solar Cells and Modules: Materials and Processes. Workshop Proceedings. (2007).
[10] L. J. Brillson and Y. Lu. ZnO Schottky barriers and Ohmic contacts. Journal of Applied Physics. 109, 121301 (2011).
[11] T. Wu, R. Chuang *et al*. ZnO nanoneedles/ZnO:Al film stack as an anti-reflection layer for high efficiency triple junction solar cell. Electrchemical and Solid- State Letters.15, 208 (2012).
[12] J. W. Leem, Y. M. Song *et al*. Effect of Al-doped ZnO film thickness on periodic GaAs subwavelength grating structures for photovoltaic device applications. Materials Research Bulletin. 47, 2884 (2012).
[13] V. Janicki, R. Leitel *et al.* Design of hybrid coatings composed of homogeneous layers and refractive index gradients. 5963, 1 (2005).
[14] J. Zhu, Z. F. Yu *et al*. Optical absorption enhancement in amorphous silicon nanowire and nanocone arrays. Nano Letters. 9, 279 (2009).

Conclusion and prospects

Conclusion

The objective of this thesis was to realize low-cost Si nanostructures (nanopillars and nanocones) based radial p-i-n junction solar cells. These solar cells have a great potential to achieve high efficiency, because nanopillars and nanocones have excellent antireflection properties and this radial geometry can minimize the carrier recombination. After giving an overview of solar cells and nanostructures used in solar cells, specifically nanowires and quantum dots, we have introduced all the techniques used to elaborate our solar cells in chapter 2. The fabrication process involves three parts: (I) low-cost fabrication based on silica balls which is used as etching mask and deposited through Langmuir-Blodgett technology, and optimization of optical properties of Si nanopillars (or nanocones); (ii) low-cost fabrication and optimization of AZO thin films transparent electrodes using sol-gel technique; (iii) integration and passivation of final device.

Si nanopillars and nanocones have excellent optical properties which vary with the geometry parameters, so in order to achieve high absorption of our solar cells, we have to optimize the absorption of nanopillars (or nanocones). Chapter 3 investigates the influence of geometry parameters, such as periods, diameters, lengths and sidewalls on the reflectance of nanopillars (or nanocones). As a complementary methods, we use FDTD method to calculate the absorption of nanopillars and nanocones. By comparing their absorption spectra, Si nanostructures are optimized. We have found that: (1) the optimized ratio of diameter and period D/P=0.7-0.8; (2) for a given ratio D/P, NPs with smaller diameters and periods have higher efficiencies; (3) nanopillars with long length have high efficiencies; (4) the influence of bottom diameter, period and length on the optical properties of nanopillars can be extrapolated to nanocones; (5) when the period, bottom diameters and height are fixed, the optimized NCs have the angle θ between 80° and 90.

Sol-gel derived Al-doped ZnO films used as transparent electrodes in solar cells should be transparent and conductive, but the operating parameters of sol-gel process affect the properties of AZO films. In chapter 4, we study the influence of doping concentration, baking temperature, annealing temperature and hydrogen treatment on the optical and electrical properties of AZO thin films. It has been found that the best AZO films with the

doping concentration of 2 wt.%, baking temperature of 200°C, post-annealing temperature of 600°C and hydrogen treatment temperature between 400°C and 500°C have the lowest resistivity of $1.6x10^{-2}$ Ωcm and have high transmittance (above 80%) in the visible and NIR region.

Finally, chapter 5 presents complete integrated planar or Si nanocones solar cells. For nanocones, the efficiency is not ideal, due to the defects on their surface and defects located at grain boundary in polysilicon. The effect of different passivation methods on the electrical properties of the solar cells has been studied. The results show that the combination of SiNx:H passivation and wet oxidation are efficient; they have improved the efficiency of our solar cells by a factor of 20.

In addition, we investigate the effect of AZO films on the optical and electrical properties of solar cells. Owing to the adaptive refractive index, AZO films are good antireflection layers. And this conformal coatings increase the effective carrier collection area of solar cells.

Prospects

The efficiencies of our solar cells are low, mainly due to very thin intrinsic layer in p-i-n diode. Nanocones solar cells should have higher efficiencies because of their high absorption, but the results show that nanocones solar cells after passivation have efficiencies comparable to planar solar cells after passivation. In order to improve the efficiency, firstly, we could optimize the thickness of intrinsic layer to increase the thickness of depletion region. Secondly, we could fabricate solar cells based on the optimized nanocones with great absorption. In chapter 3, the calculated results show that the optimized nanocones should have D/P= 0.7-0.8, conical angle between 80° and 90°. We will realize solar cells based on these nanocones with a period of 880 nm and a length of 450 nm. Thirdly, the two passivation methods should be optimized. (1) for wet oxidation method, the oxidation temperature and oxidation time have effect on the properties of Si. So it is necessary to change them. (2) for SiNx:H passivation, the power, the pressure, the deposition temperature and the time of PE-CVD (plasma-enhanced chemical vapor deposition) which are used to deposit SiNx:H layer will change the open circuit voltage V_{oc} of polysilicon based solar cells. The annealing temperature and time can also affect the electrical properties of polysilicon. So it will be interesting to investigate the influence of

these parameters on the solar cell efficiencies and optimize them.

Finally, the resistivity of AZO films we obtained should be decreased. So, the next work would be further optimization of AZO films by varying other parameters, such as PH value of precusor, aging time, heat treatment in vacuum, heat treatment time.

Annexe

Progressive multi-layer drop-casting of CdSe nanoparticles for photocurrent down shifing monitoring

Y. Lambert,[1] Di Zhou,[1] Tao Xu,[2] O. Cristini,[3] D. Deresmes,[1] B. Grandidier,[1] and D. Stiévenard[1,a)]
[1]*IEMN, UMR8520, Département ISEN, 41 Bd Vauban, 59046 Lille Cédex, France*
[2]*Key Laboratory of Advanced Display and System Application, Shanghai University, 149 Yanchang Road, Shanghai 200072, People's Republic of China*
[3]*PHLAM, UMR8523, Université de Lille 1, 59652 Villeneuve d'Asq Cédex, France*

(Received 18 April 2013; accepted 9 July 2013; published online 29 July 2013)

We investigated the spectroscopic photocurrent response of photovoltaic devices versus an increasing number of drop-casted CdSe nanoparticles onto planar and nanocones silicon p-i-n junctions. For all samples, a strong enhancement of the photocurrent in the UV range was detected as well as a constant increase of the photocurrent up to 20% (16%) for a planar (nanocones) junction in the range 600–800 nm. The analysis of the photocurrent versus the number of drop casted nanoparticles layers allows us to evidence a down-shifting mechanism in the U-V range and an adaptative index effect below the threshold of absorption. © *2013 AIP Publishing LLC*.
[http://dx.doi.org/10.1063/1.4816956]

In order to increase the energy conversion efficiency of semiconductor solar cells, many improvements have been studied (see Ref. 1 for a recent review) such as (i) hot carrier collection which reduces thermalization losses, (ii) multi-junction cell which allows absorption of a wider range of wavelengths in the solar spectrum, (iii) multi-exciton generation which promises the generation of a few excitons for one absorbed photon, (iv) intermediate band collection in which low-energy photons can be absorbed in a two-photon process, (v) up-conversion layers which convert two IR photons into one UV photon, and finally (vi) absorbing layers which convert one high UV energy photon into one low energy IR photon (down shifting) or one UV photon into more than one IR photons (down-conversion). This paper is focussed on down-shifting CdSe nanoparticle (NP) layers drop-casted on silicon junction.

Down-conversion was first proposed by Dexter[2] in 1957. Detailed analyses of the possible performance enhancement have been published[3,4] and experimental evidences were obtained in 1974 using rare earths[5] and are still of interest today.[1,6] Another promising way for down-conversion layers is the use of NPs which exhibit a series of advantages: their gap can be tuned by their size, they have high brightness, stability, and quantum efficiency.[7] Efficient light harvesting was demonstrated in planar or nanostructured junctions by adding various NPs layers such as ZnS,[8–10] PbS,[11] ZnSe,[12] CdS,[13] or Si[14] ones. Since their down-shifting effect evidenced by Lysen *et al.*,[15] the most used nanoparticles are CdSe ones,[16] with observations of non-radiative energy transfer (Förster effect),[17] simulated by Govorov *et al.*[18]

Generally, the NPs are deposited using one shot, i.e., with one thick layer of nanoparticles, excepted in the case of ZnS NPs[8] deposited using four different liquid concentrations. In this work, we have measured the photocurrent of n+-i-p planar junctions and nanostructured ones with nanocones versus the number of CdSe drop-casted nanoparticle layers. This analysis allows us to distinguish a down shifting effect observed with an excitation in the UV band and a dielectric effect observed even for a few layers of deposited NPs.

The planar junctions were obtained by LPCVD deposition of 20 nm intrinsic silicon layer followed by 70 nm n+ doped silicon layer (typically 2×10^{19} As cm^{-3}) on a planar p doped silicon substrate (typically 5×10^{18} B cm^{-3}). Aluminium (200 nm) was deposited as back contact. Ti (100 nm)–Au (200 nm) electrodes with a U shape were evaporated on the top of the structures. The technological process for nanostructured junctions was the same except that starting from bulk silicon; nanocones were obtained by Reactive Ion Etching with SiO_2 used as mask. The typical dimensions of the nanocones are: 700 nm at the bottom, 165 nm at the top, 440 nm for the height, and with an average density of 1.5×10^8 nanocones cm^{-2}. The CdSe NPs were obtained by a classical method developed by Kim *et al.* with minor modifications[19] and a target 3 nm mean size. At the end of the growth, precipitated NPs were redispersed into hexane. Additional washing (by adding methanol and using centrifugation) was needed for four more times to remove extra unreacted organics. At least, three cycles of dispersion in chloroform and drying under azote gas flow and then redispersion in chloroform were done. The photoconductivity measurements were performed using a monochromator source (ORIEL), with a 100 W Xenon light, allowing a spectroscopic analysis from 300 nm to 1100 nm. The photon flux was calibrated using a thermopile detector with a broad flat spectral response from 200 nm to 50 μm. All the photocurrent curves were therefore normalized. In order to increase the signal/noise ratio, the light flux was chopped at a frequency of 30 Hz and a lock-in detection[20] was used. In order to correlate the morphology of the drop-casted NPs layers with their absorption spectra, AFM (Atomic Force Microscopy) measurements were performed, as illustrated in Figure 1. The large scale view shows different layers of NPs

a)Email: didier.stievenard@isen.fr

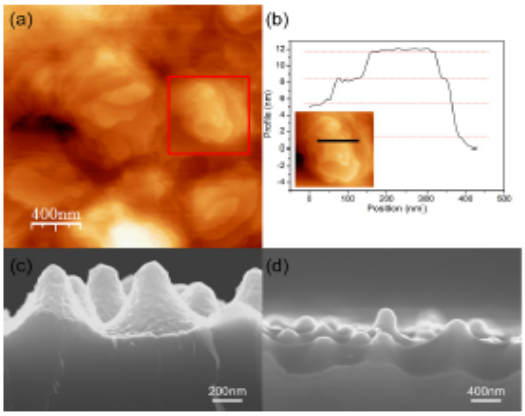

FIG. 1. (a) AFM image (5 μm × 5 μm) of drop-casted CdSe NPs on the silicon substrate; (b) enlarged image (0.5 μm × 0.5 μm) with height cross section showing steps associated with CdSe compact layers; cross sectional SEM images of a sample with nanocones and (c) without and (d) with drop casted CdSe nanoparticles.

with partially filled top layers (Fig. 1(a)). On the enlarged view (Fig. 1(b)), compact plateaux are clearly observed along a height cross section with step height of typically 3.4 ± 0.1 nm. Figure 1(c) is a SEM image of a cleaved sample with nanocones, without NPs and Figure 1(d) is the same sample after drop casting of CdSe nanoparticles (black contrast between the nanocones). We observed that the NPs are mainly deposited between the nanocones and not on their top. Moreover, the CdSe layer does not exhibit visible stacking defects, i.e., the drop casted layer has a good homogeneous stacking.

The absorption spectra of the CdSe NPs is maximum at 550 nm. According to the equation proposed by Yu *et al.*,[21] the preferential diameter size of the NPs should be 3 nm. For the same absorption peak, de Freitas *et al.*,[22] measured a diameter ranging from 2.6 to 4.8 nm with high-resolution transmission electron microscopy technique. So, the values we measured are well associated with typically one layer of CdSe NPS with an average diameter of 3–3.5 nm. This is in agreement with their absorption spectrum. It was also observed (Figure 2) in the photoconductivity spectrum of a thick layer of CdSe NPs dropcasted on silicon, where the variation of the photocurrent is perfectly superimposed to the optical absorption spectrum of the CdSe NPs. (The insert in Fig. 2 shows the photoluminescence of CdSe NPs in solution.)

In the following, we present photoconductivity measurements recorded versus the number of drop-casted NPs layers.

The photocurrent measured on planar junctions versus the number of drops (Figure 3) shows a dramatic increase up to 550% for an excitation around 350 nm. This spectrum is obtained as follows: at each wavelength, we calculate the ratio (I1-I0)/I0 where I1 is the photocurrent measured after the deposition of NPs and I0 is the photocurrent measured without any NPs.

In order to account for this effect, the following mechanisms are discussed. First, down conversion is ruled out

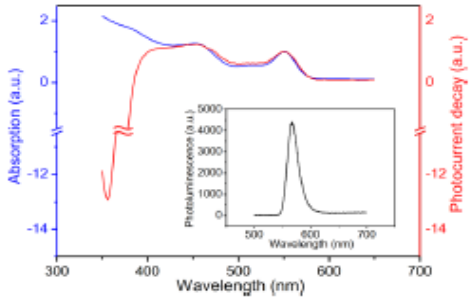

FIG. 2. Comparison of the photocurrent variation according to the CdSe NPs absorption spectrum for 6 drops (insert: PL of a solution of CdSe nanoparticles).

because it is associated with the absorption of one UV photon transformed to two IR photons. In our case, the absorption is maximum at 354 nm (3.50 eV) and the photoluminescence emission of the CdSe NPs is at 560 nm (2.21 eV). So, a photon at 3.50 eV cannot be transformed into two photons at 2.21 eV. Second, a Förster effect needs Coulombic transfer between nanoparticles with a nanoparticle size larger and larger as the transfert of the exciton is made at energy lower and lower. As the lifetime of an exciton in CdSe is of the order of a few ns and as the transfer time for the Förster effect is of the order of 100 ps,[23] a typical series of ten transfers is possible through the CdSe nanoparticles layer. But, the observed effect increases with the thickness of dropcasted nanoparticles and the Förster effect should decrease accordingly because it is more and more difficult to achieve an increasing number of bonds, with an efficacity of the transfert which varies as 1/d,[6] where d is the distance between two neighboring particles. Förster effect is unprobable.

So, we propose that a down shifting effect is observed. Indeed, this effect should be proportional to the volume of the NPs, as observed in the insert of Figure 3. Moreover, the saturation of the photocurrent is explained as the absorption

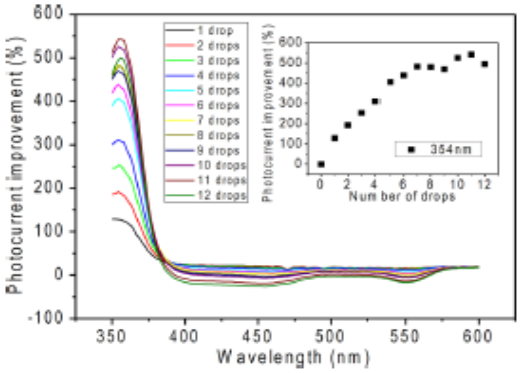

FIG. 3. Relative increase of the photocurrent versus the number of drops of CdSe NPs layers for an optical excitation ranging from 350 to 600nm; Insert: Relative increase of the photocurrent versus the number of drops of CdSe NPs layers measured for an optical excitation of 354 nm.

of a high energy photon by the down-shifting layer can only result in the generation of one electron-hole pair in the junction, i.e., this mechanism cannot overcome the Shockley-Queisser efficiency limit.

As shown in Figure 4, the same effects have been observed in nanocones n+-i-p junction.

However, a decrease of the photocurrent is observed at 366 nm. A simulation using the Finite Difference Time Domain (FDTD) method shows a different behavior of the reflectance between a planar and a NCs structure. At 366 nm (maximum of the n index of silicon), a peak is observed for reflectance. Relatively, this peak (amplitude of 10%) has more importance for NCs (average reflectance of 20%) than for planar structure (average reflectance of 45%) and, therefore, it is easily detected. As the NPs can be considered as resonators coupled to the structure, they "feel" the global behavior of the structure. Moreover, simulations show a decrease of the electric field near the surface for excitation at 366 nm, compared to the one obtained at 354 nm. So, the absorption of the NPs is less enhanced at 366 nm, leading to a lowering of the down shift effect, i.e., a decrease of the photocurrent.

Another increase of the photocurrent correlated with the number of dropcasted NPs is also observed in the range 600 to 800 nm, below the threshold of the absorption in the NPs.

Figure 5 shows the relative increase of the photocurrent measured at 650 nm and versus the number of drops (layers) on planar junctions (filled squares). As soon as one or two drops are deposited, i.e., for a few ten monolayers of NPs, a relative increase of the photocurrent ranging from 18% to 20% is observed.

We attribute this increase to a dielectric adaptation effect. The photocurrent is directly bound to the transmission coefficient $t_{air\text{-}silicon}$ between air ($n_{air}=1$) and silicon ($n_{Si}=3.43$) or $t_{air\text{-}CdSe\text{-}silicon}$ when CdSe nanoparticles are dropcasted. This coefficient, between two materials 1 and 2, is equal to $4n_1n_2/(n_1+n_2)^2$ where n is the optical index equal to the square root of the dielectric constant of the material. For three materials (i.e., air, CdSe, and silicon), the transmission coefficient is equal to the product between the one

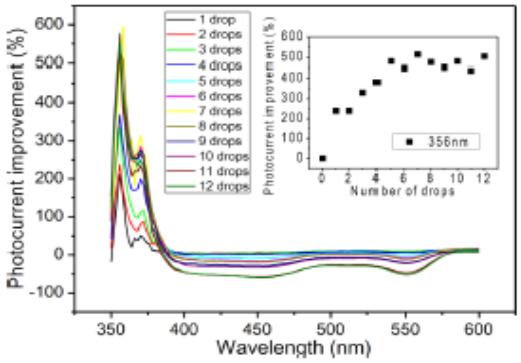

FIG. 4. Relative increase of the photocurrent versus the number of drops of CdSe NPs layers for an optical excitation ranging from 350 to 600 nm in a nanocone junction; Insert: Relative increase of the photocurrent versus the number of drops of CdSe NPs layers measured for an optical excitation of 354 nm.

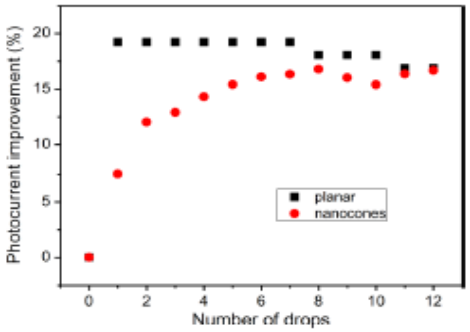

FIG. 5. Relative increase of the photocurrent versus the number drop-casted CdSe NPs layer measured for an optical excitation at 650 nm for a planar junction (squares) or a nanocones based junction (filled circles).

calculated at the air-CdSe interface by the one calculated at the CdSe silicon interface. We find $t_{air\text{-}silicon}=0.70$ and $t_{air\text{-}CdSe\text{-}silicon}=0.832$, i.e., a relative increase of 19%, in good agreement with the experimental value. For the dielectric constant of CdSe (equal to 7 for bulk material), we have taken into account the filling factor of a compact network of spherical nanoparticles (see Figure 1), equal to 0.48, i.e., the effective dielectric constant of the nanoparticles layer is equal to 7×0.48. Another correction can be taken into account: the top layers are not filled at 100% as shown in Figure 1(a). But, as only a few top layers are concerned, compared to a great number of underlayers, the effect on the total filling factor is less than 5%, i.e., a final impact on the transmission coefficient of 1 or 2% (because the transmission function versus the n index is a smooth function around its maximum, which is our experimental case), always in agreement with the experimental results.

The same effect is observed on nanocones based junctions, as shown in Figure 5 (filled circles). In that case, the relative increase of the photocurrent associated with the graded dielectric effect is a little lower compared to the precedent one, i.e., of the order of 16%. This is logical since there is already a dielectric effect associated with the nanocones (the dielectric constant associated with the silicon nanocones is lower than the bulk silicon one because their silicon filling factor is less than one). So, the CdSe layer dielectric effect is just an additional effect. Moreover, for the first drops, as shown in Figure 1(d), the NPs are preferentially between the nanocones and therefore the associated dielectric effect is lower compared to the effect observed on the planar junction.

In conclusion, we have evidenced an increase of photocurrent of a planar silicon junction or of nanocones based silicon junction associated with a progressive number of CdSe dropcasted nanoparticles layers. This original progressive approach allows to unambiguously separate an efficient down-shifting effect and a graded dielectric effect.

This work was supported the Ministry of Higher Education and Research, Nord-Pas de Calais Regional Council and FEDER through the "Contrat de Projets Etat Region (CPER) 2007-2013". Di Zhou has a Ph.D. grant from

the People's Republic of China. T. Xu acknowledges the support from the National Natural Science Foundation of China (61204014) and the Innovation Project of Education Commission of Shanghai Municipality (12YZ021).

[1]X. Huang, S. Han, W. Huang, and X. Liu, Chem. Soc. Rev. **42**, 173 (2013).
[2]D. Dexter, Phys. Rev. **108**, 630 (1957).
[3]B. S. Richards, Sol. Energy Mater. Sol. Cells **90**, 1189 (2006).
[4]W. G. J. H. M. van Sark, Thin Solid Films **516**, 6808 (2008).
[5]W. Piper, J. deLuca, and F. Ham, J. Lumin. **8**, 344 (1974).
[6]R. Rothemund, S. Kreuzer, T. Umundum, G. Meinhardt, T. Fromherz, and W. Jantsch, Energy Procedia **10**, 83 (2011).
[7]P. V. Kamat, J. Phys. Chem. C **112**, 18737 (2008).
[8]C.-Y. Huang, D.-Y. Wang, C.-H. Wang, Y.-T. Chen, Y.-T. Wang, Y.-T. Jiang, C.-C. Chen, and Y.-F. Chen, ACS Nano **4**(10), 5849 (2010).
[9]M. Ahmad, K. Rasool, M. A. Rafiq, and M. M. Hasan, Appl. Phys. Lett. **101**, 223103 (2012).
[10]A. Le Donne, S. K. Jana, S. Banerjee, S. Basu, and S. Binetti, J. Appl. Phys. **113**, 014903 (2013).
[11]C.-Y. Huang, D.-Y. Wang, C.-H. Wang, Y.-T. Chen, Y.-T. Wang, Y.-T. Jiang, Y.-J. Wang, C.-C. Chen, and Y.-F. Chen, J. Phys. D: Appl. Phys. **44**, 085103 (2011).
[12]J.-Y. Jung, K. Zhou, J.-H. Bang, and J.-H. Lee, J. Phys. Chem. C **116**, 12409 (2012).
[13]H.-C. Chen, C.-C. Lin, H.-V. Han, K.-J. Chen, Y.-L. Tsai, Y.-An. Chang, M.-H. Shih, H.-C. Kuo, and P. Yu, Sol. Energy Mater. Sol. Cells **104**, 92 (2012).
[14]X. Pi, L. Zhang, and D. Yang, J. Phys. Chem. C **116**, 21240 (2012).
[15]W. G. J. H. M. van Sark, A. Meijerink, R. E. I. Schropp, J. A. M. van Roosmalen, and E. H. Lysen, Sol. Energy Mater. Sol. Cells **87**, 395 (2005).
[16]S. Chanyawadee, R. T. Harley, M. Henini, D. V. Talapin, and P. G. Lagoudakis, Phys. Rev. Lett. **102**, 077402 (2009); B. Güzeltürk, E. Mutlugün, X. Wang, K. L. Pey, and H. V. Demir, Appl. Phys. Lett. **97**, 093111 (2010); H. M. Nguyen, O. Seitz, D. Aureau, A. Sra, N. Nijem, Y. N. Gartstein, Y. J. Chabal, and A. V. Malko, *ibid.* **98**, 161904 (2011); J. Choi, B. Parida, H. Y. Li, S. Park, and K. Kim, J. Nanosci. Nanotechnol. **12**(7), 5619 (2012); O. Seitz, L. Caillard, H. M. Nguyen, C. Chiles, Y. J. Chabal, and A. V. Malko, Appl. Phys. Lett. **100**, 021902 (2012).
[17]T. Förster, Ann. Phys. Leipzig **437**, 55 (1948).
[18]P. L. Hernadez-Martinez and A. O. Govorov, Phys. Rev. B **78**, 035314 (2008).
[19]J. I. Kim and J. K. Lee, Adv. Funct. Mater. **16**, 2077 (2006).
[20]T. Xu, Y. Lambert, B. Grandidier, D. Stiévenard, A. Akjouj, Y. Pennec, and B. Djafari-Rouhani, J. Appl. Phys. **112**, 033506 (2012).
[21]W. W. Yu, L. H. Qu, W. Z. Guo, and X. G. Peng, Chem. Mater. **15**, 2854 (2003).
[22]J. N. de Freitas, I. R. Grova, L. C. Akcelrud, E. Arici, N. S. Sariciftci, and A. F. Nogueira, J. Mater. Chem. **20**, 4845 (2010).
[23]S. Lu, Z. Lingley, T. Assano, D. Harris, T. Barwicz, S. Guha, and A. Madhukar, Nano Lett. **9**, 4548 (2009).

Publications

- Y. Lambert, **D. Zhou,** T. Xu, O. Cristini, D. Deresmes, B. Grandidier and D. Stiévenard. Progressive multi-layer drop-casting of CdSe nanoparticles for photocurrent down shifting monitoring. Applied Physics Letter 103, 051102 (2013).
- **D. Zhou**, A. Boé, Y. Lambert, D. Stiévenard, O. Cristini, R. Bernard, K. Raulin and S. Turrell. Low-cost sol-gel synthesis of Al-doped ZnO films:influence of operating parameters. E-MRS, May 27-31,2013, Strasbourg, France (Poster)
- Y. Lambert, **D. Zhou**, T. XU, O. Robbe and D. Stiévenard. Multi-layer drop-casted CdSe nanoparticles for photovoltaic: a strong down-convertion evidence. E-MRS, May 27-31,2013, Strasbourg, France (Poster)
- Y. Lambert, **D. Zhou**, O. Robbe and D. Stiévenard. R. P. Nalini, J. Cardin, C. Dufour and F. Gourbilleau. Correlated structural and photoelectrical characterization of Si-rich silicon oxide (SRSO)/SiO2 multilayer systems. E-MRS, May 27-31,2013, Strasbourg, France (Poster)
- **D. Zhou**, Y. Pennec, B. Djafari-Rouhani, T. XU, Y. Lambert, O. Robbe, Y. Deblock and D. Stiévenard. Optical properties of nanopillars/nanocones based solar cells : FDTD simulation and experimental tests. Physics Review B. (under redaction)
- **D. Zhou**, O.Cristini, R. Bernard, Y. Lambert, K. Raulin, A. Boé, S. Turrell and D. Stiévenard. Low-cost sol-gel synthesis of Al-doped ZnO films: influence of operating parameters. Thin films. (under redaction)
- **D. Zhou**, R. Bernard, O. Cristini, D. Stiévenard. Hydrogen and wet oxidation used to passivate planar and nanocones solar cells. Solar energy materials & solar cells. (under redaction)

Conception et réalisation de cellules solaires à base de nanostructures silicium

Dans les cellules solaires planaires silicium, le matériau doit être assez épais pour que l'absorption des photons soit efficace, et dans le même temps, l'accroissement de l'épaisseur augmente les chances de recombinaison des porteurs. Afin d'avoir à la fois absorption et couche mince, des structures radiales (nanopiliers ou nanocones) peuvent être utilisées, qui ont des diamètres inférieurs à la longueur de diffusion des porteurs minoritaires, ce qui garantit une bonne collecte des porteurs.

Ce travail présente la réalisation et la caractérisation de cellules solaires silicium bas coût, basées sur des nanostructures (piliers ou cônes). Pour la nanostructuration, l'usage d'un masqueur électronique est évité grâce à l'utilisation de microbilles de silice, déposées par technique Langmuir-Blodget et servant de masque à la gravure sèche des nanostructures. L'électrode face avant est en ZnO, obtenue par technique sol-gel. Avant la fabrication, une simulation des propriétés optiques des nanostructures en fonction de leur forme (densité, hauteur, diamètre,) a été réalisée à l'aide de calculs FDTD (Finite Difference Time Domain). La synthèse des films ZnO par sol gel a été optimisée (concentration des dopants, recuit thermique, hydrogénation, …) afin d'avoir la meilleure transparence optique et la plus faible résistivité. Finalement, des cellules solaires n^+- i - p ont été réalisées, assemblant nanostructures et couche ZnO. Des étapes supplémentaires de passivation des défauts de surface et d'interfaces associés aux nanostructures ont été finalement menées.

Conception and realization of solar cells based on silicon nanostructures

For planar p-n junction solar cell, the material must be thick enough to have enough absorption, whereas increasing the thickness leads to the increase of recombination of carriers. In order to decouple the requirement of light absorption and carrier collection, nanopillars (or nanocones) radial p-n junction are introduced. Nanopillars (or nanocones) have greater absorption and radial geometry offers minimal recombination if the diameter of nanopillars (or nanocones) is smaller than the minority carrier diffusion length.

This work presents the realization and characterization of low-cost Si nanostructures (nanopillars and nanocones) solar cell with sol-gel derived ZnO transparent electrodes. In order to decrease the fabrication price, silica balls and Lamuguir-Blodgett techniques are used as the substitutes of photoresist and electrical beam lithography, respectively. Besides, ZnO thin film transparent electrodes are synthesized by low-cost sol-gel methods For pursuiting high efficiency, first of all, we have tested the absorption of nanopillars and nanocones by varying their periods, diameters, lengths and sidewalls. Second, we have optimized the electrical properties of ZnO thin film by changing the synthesis parameters, such as doping concentration, baking temperature, anneal temperature and hydrogen treatment. In the end, solar cells were fabricated based on optimized Si nanostructures and optimized ZnO thin films. Due to their bad electrical properties associated with surface defects, surface passivation methods were performed to reduce the defects concentration in p-i-n junction and improve the efficiency of solar cells.